Entanglement, Bell's inequalities and coherence: new ideas and new scenarios

by

Adam Vallés Marí

submitted for the degree of
Doctor of Philosophy

Thesis Advisor: Prof. Dr. Juan P. Torres

ICFO-INSTITUT DE CIÈNCIES FOTÒNIQUES
UPC-UNIVERSITAT POLITÈCNICA DE CATALUNYA

Barcelona, January 2017

ICFO
Institut
de Ciències
Fotòniques

UPC
UNIVERSITAT POLITÈCNICA
DE CATALUNYA
BARCELONATECH

To my family

ACKNOWLEDGEMENTS

Looking backwards now, I can see all wagons full of people from this train that has brought me here.

From that first train station at UPC, where I asked Prof. Juan P. Torres if I could jump in and try to understand the mysteries of quantum mechanics, many people has accompanied me in this journey. People that I would like to thank, seizing the opportunity that these lines give me, for their support and guidance through all the stations that have already past.

I would like to begin by expressing my gratitude to my supervisor Juan P. Torres, for giving me the opportunity to work in ICFO and having the patience to guide me whenever I lost track. I am also in great debt with my mentor, Martin Hendrych. He transferred me part of his endless knowledge during my first period in ICFO, and taught me how to whisper to all quantum machinery to get the most of it.

Someone once said that there are two families: the one that blood gives you and the one that you choose. Before starting to enumerate all the essential people in this journey, let me dedicate this thesis to the people that have always been present in all trains I have travelled with and surely will do. Thanks for the unconditional support to my *mother* and *sister*, Raül, my father and the most loved little ones, Eladi and Aran, followed by Ruben, Matias, Oriol and Aitor.

ICFO possess an incomparable environment for science, offering in my opinion, a prefect mixture of professional and leisure activities, enhancing scientific networking where people can become more creative. I would like to deeply thank all components of the Quantum Engineering of Light group, for their useful discussions and precious help during these last years. Thank you so much to Luis José Salazar, Carmelo Rosales, Roberto León, Jiří Svozilík, Nathaniel Hermosa, Michal Mičuda, Gerard Jiménez, Jessica Oliveira, Júlia Amorós and Adrià Barja. From ICFO special thanks to Vincenzo D'Ambrosio, Silvana Palacios, Valeria Rodriguez, Rafael Giner, Javier Encomienda, Fabian Steinlechner, Roland Terborg, Giorgio Colangelo, Gianvito Lucivero, Marc Jofre, Miquel Rudé, Carlos Abellán, Ferran Martín and of course to all the ICFO departments for making our life so easy, mechanical and electronic workshops, human resources, purchasing, IT, logistics, maintenance and travel.

I would like to specially thank Luis José Salazar and Vincenzo D'Ambrosio to carefully read and helping me correct this manuscript, and also the PhD thesis reviewers José Capmany, Jordi Mompart and Hugues de Riedmatten.

In some parts of the journey it may seem that there were no life outside the laboratory, for that reason, people pushing you out from the ICFO wagon are even more important. Thanks for being the great part of this story Pau Garcia, Steffen Neuwirth, Ivan Salas, Isaac Llopis, Elena Castaño, Fanny Ulldemolins, Diego Pastor, Aitor Aldama, Ade Blanchart, Lluís Tapia, Anna Velmar, Arturo Manzano, Sara Martín, Sara Urgell, John and Zoe McCrudden, Anxo Armada and thanks for your smiles and patience Cristina Ballbé.

ABSTRACT

The work presented in this thesis, mostly experimental, is based on three main pillars: the concepts of entanglement, Bell's inequalities and coherence. Entanglement is a very special type of correlation that can exist between two systems, even if these systems are physically separated by a large distance. Bell's inequalities are a window to inquiry fundamental questions about how Nature works at its fundamental level, and it turns out that they can also become tools with practical relevance. Coherence is a fundamental trait of electromagnetic theory, in the classical as well as in the quantum regimes, and it is closely linked to the concept of entanglement.

In this thesis we study different platforms aimed at generating entangled states. We control its properties, measure the quality of the entanglement and search for links with concepts such as coherence. In certain cases of practical interest, the generation of entanglement can become a great challenge due to technical difficulties of the experiments. From a fundamental point of view, the concept of entanglement still poses questions about what it really means and where it can manifest.

In the different experiments presented in this thesis, we have generated different kinds of entanglement capable of being used in various environments. For instance, this is the case of the generation of polarization entangled paired photons at the telecom band in a

semiconductor Bragg reflection waveguide. This represents a significant step towards the realization of efficient and versatile sources of entangled photon pairs, that could be integrated in a microchip.

In another experimental scheme we have proved, also by measuring the violation of the Clauser, Horne, Shimony and Holt (CHSH) Bell-like inequality, the generation of non-coherent and coherent correlations between different degrees of freedom of a single photon, finding a close analogy with the entanglement that can exist between two distant photons. These types of experiment can help in discussions aimed at illuminating what is the true meaning of entanglement.

Lastly, in a third experiment we make use of frequency-entangled photons to demonstrate a new type of optical coherence tomography (OCT) scheme, where the reflectivity of the sample translates in a change of coherence. We call this new approach *induced optical coherence* tomography (iOCT). This new scheme allows probing the sample with one wavelength and measuring light with another wavelength. As a result, we can gain penetration depth into the sample by using longer wavelengths, while still using the optimum wavelength for detection.

Finally, from a theoretical perspective, we study how coherence and correlations represent two related properties of a compound system. We derive an expression that determine the relationship between the degree of coherence of each subsystem, and the type and degree of the correlation present between the subsystems. We also demonstrate that the degree of violation of the CHSH inequality is the appropriate measure that quantifies how much correlations can be turned into coherence, and how much coherence can be extracted.

RESUM

El treball presentat en aquesta tesi, majoritàriament experimental, es basa en tres pilars fonamentals: els conceptes d'entrellaçament, desigualtats de Bell i coherència. L'entrellaçament és un tipus molt especial de correlació que pot existir entre dos sistemes, fins i tot si aquests es troben físicament molt allunyats un de l'altre. Les desigualtats de Bell són una finestra que invita a preguntar-se com es comporta la Natura en el seu nivell més fonamental, com també es poden convertir en eines de gran rellevància pràctica. La coherència és una característica fonamental de la teoria electromagnètica, tant en l'àmbit clàssic com en el quàntic, i també compta amb una relació directa amb l'entrellaçament.

En aquesta tesi estudiem diferents plataformes per poder generar estats entrellaçats. Per tant, poder controlar les seves propietats, mesurar la qualitat de l'entrellaçament i buscar connexions amb altres conceptes com ara la coherència. En alguns casos d'interès pràctic, la generació d'entrellaçament pot convertir-se en un gran repte a causa de les dificultats tecnològiques dels experiments. Des d'un punt de vista fonamental, el concepte d'entrellaçament per se encara porta a qüestionar-se quin és el seu significat realment i on es pot manifestar.

En els diferents experiments presentats en aquesta tesi, hem generat diferents tipus d'entrellaçament capaços de ser implementats en varis entorns. Com per exemple, un dels casos seria el de la generació

de parells entrellaçats en polarització per la banda de telecomunicació, mitjançant les guies d'ona per reflexió Bragg formades d'un material semiconductor. Aquest avenç representa un pas important en vers a la realització de fonts de parells de fotons entrellaçats que siguin eficients i versàtils, i que a més puguin ser integrades en un microxip.

Mitjançant un altre esquema experimental, mesurant també la violació d'una desigualtat de Bell, que en el nostre cas es tracta de la desigualtat de Clauser, Horne, Shimony i Holt (CHSH), hem demostrat la generació de correlacions no-coherents i coherents entre dos graus de llibertat d'un mateix fotó, trobant d'aquest forma una clara analogia amb l'entrellaçament que pot haver-hi entre dos fotons físicament allunyats. Aquests tipus d'experiments poden contribuir a esclarir el vertader significat de l'entrellaçament.

Finalment, mitjançant l'ús de l'entrellaçament en freqüència, en el tercer experiment hem demostrat un nou tipus d'esquema de tomografia de coherència òptica (OCT), on la reflectivitat de la mostra representa un canvi de coherència. Nosaltres anomenem aquest nou enfoc com tomografia de *coherència òptica induïda* (iOCT). Aquest nou esquema permet analitzar la mostra amb una longitud d'ona i mesurar-ne l'efecte amb una altra. D'aquesta forma es pot aconseguir més profunditat de penetració al sondejar la mostra amb una longitud d'ona llarga, mentre es fa servir una altra longitud d'ona òptima per ser detectada.

Per acabar, hem estudiat des d'un punt de vista teòric, com la coherència i les correlacions representen dos propietats relacionades dins d'un sistema compost. Derivem una expressió que determina la relació entre el grau de coherència de cada subsistema, i el tipus i grau de correlació present entre els subsistemes. Com també demostrem que el grau de violació de la desigualtat CHSH és la mesura apropiada que quantifica quanta correlació pot transformar-se en coherència, i quanta coherència pot ser extreta.

CONTENTS

LIST OF FIGURES

LIST OF ABBREVIATIONS

EPR	Einstein, Podolsky and Rosen
CHSH	Clauser, Horne, Shimony and Holt
LOCC	local operations classical communications
DoF	degree of freedom
SPDC	spontaneous parametric down-conversion
BBO	beta barium borate
KTP	potassium titanyl phosphate
$LiNbO_3$	lithium niobate
HOM	Hong-Ou-Mandel
BS	beam splitter
PBS	polarization beam splitter
LHVM	local hidden variable model
OAM	orbital angular momentum
BRW	Bragg reflection waveguide
AlGaAs	aluminium gallium arsenide
InGaAs	indium gallium arsenide
TIR	total internal reflection
KDP	potassium dihydrogen phosphate
SHG	second harmonic generation
SLM	spatial light modulator
FWHM	full-width at half maximum

GVM	group velocity mismatch
GVD	group velocity dispersion
DM	dichroic mirror
HWP	half-wave plate
QWP	quarter-wave plate
NDF	neutral density filter
DL	delay line
SNOM	scanning near-field optical microscope
QP	q-plate
MNMS	maximally nonlocal mixed state
MEMS	maximally entangled mixed state
OCT	optical coherence tomography
iOCT	induced optical coherence tomography
Nd:YVO4	neodymium-doped yttrium vanadate
LBO	lithium triborate
PPLN	periodically-polled lithium niobate
OSA	optical spectrum analyzer
BPF	band-pass filter
LPF	long-pass filter
SPF	short-pass filter
FBG	fibre Bragg grating

CHAPTER ONE

INTRODUCTION

The core of this thesis is based on three fundamental concepts of quantum information science: entanglement, Bell's inequalities and coherence. Notwithstanding being different ideas, all three are profoundly linked somehow. For instance, only entangled states can violate a Bell-like inequality, being the degree of that violation also a possible measure of coherence. However, the inequality can hold even for certain states that are entangled.

Our interest in this thesis will be both fundamental and practical. From a fundamental perspective, entanglement and the violation of Bell's inequalities by all pure entangled states are distinctive traits of quantum theory, one that indeed shakes our understanding of how Nature works. However, the underlying mathematical structure of quantum entanglement seems to appear in other scenarios as well, even it can be *recreated* in certain phenomena of classical optics. On the other hand, the degree of violation of a Bell's inequality can be used as a *measure of coherence*. Coherence is a fundamental aspect of electromagnetic theory, both in the classical as in the quantum regimes, and it is closely linked to the concept of entanglement.

This opens unexpected connections between quantum and classical optics in both directions. It can illuminate a direction towards new ways of doing things in classical optics, what can be called as *quantum-inspired* optics (see Chapter 5). It can also contribute to a better understanding of what it means to be entangled, by allowing the simulation of certain features of entangled states in scenarios easier to handle experimentally (see Chapter 4).

From a practical point of view, entanglement is a pillar of many protocols of quantum information science. Therefore, the road map towards the implementation of quantum technologies out-of-the-lab includes the development of efficient, robust, tunable and even easy-to-use entanglement generators, that moreover could be integrated with other elements such as sources of light and quantum information processing elements (see Chapter 3). The use of entanglement can even facilitate the implementation of new types of diagnosis systems, as it is the case of the quantum optical coherence systems (see Chapter 6).

Some historical remarks

The concept of entanglement was originally introduced to explain the unexpected correlations existing between two spatially separated systems that had interacted in the past. It was Schrödinger who coined this phenomenon as "entanglement" [1]. In the same year 1935, Einstein, Podolsky and Rosen (EPR) [2] were the first to introduce the idea that a "spooky action at a distance" seems to be needed in order to explain certain non-local properties of the quantum machinery, a characteristic that they would not want to be part of the theory.

Since then, the understanding of the concept of entanglement has played, and still plays, a key role in the discussions about the foundations of quantum mechanics. Bohr started [3], just five months right after the EPR paper was published, a debate than in different ways is still going on. In 1964, John S. Bell made arguably the biggest contribution to the discussion when he stated two important assumptions about the functioning of nature [4]:

Realism: all the observables must have a pre-existing outcome before any possible measurement is performed.
Locality: any outcome resulting of a measurement in one location can not be modified by any action performed at a spacelike separation.

Bell put forward an inequality, based on statistical correlations, where the two previous assumptions imposed a bound on the possible outcomes of experiments involving bipartite systems. Surprisingly, this bound or limit could be exceeded when the probabilities from the outcomes were obtained by measuring some entangled state, hence violating the Bell's inequality. Clauser, Horne, Shimony and Holt (CHSH) stated in 1969 a Bell-like inequality [5] suitable to be violated in the laboratory using photonic elements. However it was Aspect et al. [6, 7] who first convincingly demonstrated in 1981-2 the violation of a CHSH Bell-like inequality in the laboratory. Since then, many experiments have tested the quantum formalism [8, 9].

Goals of this thesis

The goals achieved in this thesis, all of them related to the fundamental concepts of entanglement and coherence, are

- To study and implement a new photonic platform for the generation of entanglement, in principle more adequate for the future implementation of quantum circuits in out-of-the-lab scenarios, a key element for the development of integrated quantum technologies (see Chapter 3).
- To analyse theoretically and experimentally the entanglement concept in new scenarios, that can help opening new connections between ideas and applications in classical and quantum optics, and between very different systems (see Chapters 2 and 4).
- To unveil new roles for the venerable Bell-like CHSH inequality and coherence outside the original scenario where they were invented for (see Chapter 5).

- To demonstrate a new application that can be facilitated by using frequency-entangled photons, in particular, a new way to realize optical coherence tomography (OCT) where coherence is not only used for axial sectioning of a measure of reflectivity, but it is also what carries the sought-after reflectivity information, which provides certain advantages (see Chapter 6).

Outline of the thesis

The work presented in this thesis is organized as follows.

In **Chapter 2** we briefly introduce the concepts of entanglement, Bell's inequalities and coherence, that will be used throughout the thesis. We will state the main ideas that constitute the framework of the different experiments presented. Finally, we will introduce a new, and very physical, view of the concept of entanglement by means of three examples: spatially separated entangled states, correlations between different degrees of freedom of a single system, even a classical one, and the functioning of pigment-proteins that constitute light-harvesting complexes of photosynthetic bacteria. All of these systems show similar types of correlations, even though they are different types of systems. The aim will be to show that the presence of entanglement in all of these different scenarios should not be unexpected, once it is realized that the very same mathematical structure can describe all of them. We show that the only condition for entanglement to exist is that a single excitation is coherently delocalized between the different subsystems that compose the system of interest.

In **Chapter 3** we demonstrate experimentally the generation of paired photons entangled in the polarization degree of freedom at the telecom wavelength of 1550 nm, by means of spontaneous parametric down-conversion in an AlGaAs semiconductor Bragg reflection waveguide. The pairs of photons show visibility higher than 90% in several polarization bases and violate a Clauser-Horne-Shimony-Holt (CHSH) Bell-like inequality by more than 3 standard deviations.

This represents a significant step towards the realization of efficient and versatile sources of entangled photon pairs on-chip.

In **Chapter 4** we show a scheme to generate non-coherent and coherent correlations, i.e., a tunable degree of entanglement, between degrees of freedom of a single photon. Its nature is analogous to the tuning of the purity (first-order coherence) of a single photon forming part of a two-photon state by tailoring the correlations between the paired photons. Therefore, well-known tools such as the CHSH inequality can also be used again to characterize entanglement between degrees of freedom. More specifically, CHSH inequality tests are performed, making use of the polarization and the spatial shape of a single photon. The four modes required are two polarization modes and two spatial modes with different orbital angular momentum.

We study in **Chapter 5** how coherence and correlations represent two related properties of a compound system. The system can be, for instance, the polarization of a photon, which forms part of a polarization-entangled two-photon state, or the spatial shape of a coherent beam, where each spatial mode bears different polarizations. Whereas a local unitary transformation of the system does not affect its coherence, global unitary transformations modifying both the system and its surroundings can enhance its coherence, transforming mutual correlations into coherence. The question naturally arises of what is the best measure that quantifies the correlations that can be turned into coherence, and how much coherence can be extracted. We answer both questions, and illustrate its application for some typical simple systems, with the aim at illuminating the general concept of enhancing coherence by modifying correlations.

In **Chapter 6** we consider a new type of optical coherence tomography (OCT) scheme. It makes use of frequency-entangled photons, and where the coherence of the photon sources play a new role. In the usual OCT scheme, an interferometer is used to measure the reflectivity of a sample. The low-coherence of the source is used to determine the axial location of such measure (axial sectioning), so that a map of reflectivities in the axial direction can be obtained. In our scheme, the reflectivity of the sample also translates in a change of coherence, that is the magnitude that is measured in the interferometer. Moreover, our *induced optical coherence* tomography scheme allows probing the sample with one wavelength and measuring light with another wavelength. Which could allow, for instance, further penetration depth into the sample by using longer wavelength, while still using the optimum wavelength for detection.

In **Chapter 7** we summarize the main results presented in this thesis and its possible implications in future research.

CHAPTER

TWO

SOME BASIC IDEAS ABOUT ENTANGLEMENT, BELL'S INEQUALITIES AND COHERENCE

Quantum entanglement is one of the most important and fundamental, and probably most surprising, concepts in Quantum Mechanics. It has been observed in many different types of quantum systems. For instance, it has been detected experimentally in continuous variable systems such as position-momentum [10], which it is the original scenario of the EPR [2] *gedanken* experiment, and in systems made of qubits, such as electron spins and photon-polarization [11], which are described by two-dimensional Hilbert spaces.

The most common scenario to observe entanglement is when a pair of parties interact in such a way that the resulting quantum state cannot be written as the direct product of quantum states describing each of the subsystem. The quantum state of each party is a mixed state, while the quantum state that describes the whole system is in a pure state. In other words, the two parties must be analysed as a whole system, being impossible to describe the whole system as the sum of descriptions for each part. This fact makes necessary the introduction of concepts such as non-locality, a property of quantum systems that is being actively investigated up to date [12] in the context of Bell's inequalities.

2.1 Entanglement

In general, a bipartite state (subsystems A and B) is said to be separable if it can be written as

$$\rho^{AB} = \sum_i p_i \, \rho_i^A \otimes \rho_i^B, \tag{2.1}$$

where $\rho_i^A = |\Psi_i\rangle_A \langle\Psi_i|_A$ is the density matrix that describes subsystem A, and $\rho_i^B = |\Psi_i\rangle_B \langle\Psi_i|_B$ describes subsystem B. A system that is not separable is entangled.

In order to simplify the analysis, we will consider entanglement shared by two two-dimensional systems, where pure states can be represented by qubits. The most general expression of a qubit reads as

$$|\psi\rangle = \alpha \, |0\rangle + \beta \, |1\rangle \, . \tag{2.2}$$

This is a superposition of two orthogonal states: $|0\rangle$ and $|1\rangle$.

2.1.1 Bell states

The four Bell states are quantum states that show maximum entanglement (1 ebit, 1 bit of entanglement). Let $|0\rangle_A$, $|1\rangle_A$ and $|0\rangle_B$, $|1\rangle_B$ be orthogonal bases in the two quantum subsystems that we label as A and B. The four Bell states write

$$\begin{aligned} \left|\psi^\pm\right\rangle &= \frac{1}{\sqrt{2}}(|0\rangle_A |1\rangle_B \pm |1\rangle_A |0\rangle_B), \\ \left|\phi^\pm\right\rangle &= \frac{1}{\sqrt{2}}(|0\rangle_A |0\rangle_B \pm |1\rangle_A |1\rangle_B). \end{aligned} \tag{2.3}$$

For the sake of simplicity, from now on we will write $|0\rangle_A |0\rangle_B \equiv |00\rangle$. The state $|\psi^+\rangle$, for instance, can be written as

$$\left|\psi^+\right\rangle = \frac{1}{\sqrt{2}}(|01\rangle + |10\rangle). \tag{2.4}$$

These four quantum states constitute an orthogonal bases of the global system AB, since any 2-qubit state can be represented as a linear combination of Bell states.

An entangled state can not be written as a product of quantum states that describe the two different parties A and B separately. This means that the quantum state must be taken into account as a whole, no matter how far apart the parties could be. The two different quantum subsystems are not independent, and each one is described by a maximally mixed state. However the global state that describe A and B is pure. The correlations between subsystems A and B that make the global system pure are called quantum correlations, and are different from the classical correlations given by Eq. (2.1).

2.1.2 Measures of entanglement for pure states

Entanglement can be quantified, so one can define a degree of entanglement between two parties. Some of these measures are entanglement of formation [13], entanglement of distillation [14], relative entropy of entanglement [15] or squashed entanglement [16].

There are some characteristics that any measure of entanglement M has to fulfil. The two most important are:

- $M = 0$ if the state is separable, i.e., $\rho = \sum_i p_i \rho_i^A \otimes \rho_i^B$.
- The quantity M can not increase under local unitary transformation, that is to say that M must be invariant to any choice of basis, and it cannot increase under the possibility of classical communications (LOCC: local operations classical communications).

For a bipartite pure state, one of the simplest measurements that fulfils all the previous characteristics is the entropy of entanglement

$$E(\psi) = -\mathrm{tr}\left\{\rho_A \log_2(\rho_A)\right\} = -\mathrm{tr}\left\{\rho_B \log_2(\rho_B)\right\}, \tag{2.5}$$

where ρ_A and ρ_B are the density matrices that characterize subsystems A and B and that are obtained by means of the partial trace of the density matrix $\rho_{AB} = |\psi\rangle\langle\psi|$. The entropy of entanglement vanishes when ρ_A and ρ_B are pure states, and it reaches its maximum value when ρ_A and ρ_B are completely mixed states.

2.1.3 The density matrix

Quantum states that cannot be represented by a pure state should be represented by a density matrix, a more general form to express the quantum state of a system. Any density matrix can be written as a sum of density matrices corresponding to pure state, i.e.,

$$\rho = \sum_i p_i |\psi_i\rangle\langle\psi_i|, \tag{2.6}$$

being p_i real and positive values. A pure state would correspond to the case where the expansion contains a single term.

A quantum system is in a *pure state* if and only if its density matrix fulfils the condition $\mathrm{tr}(\rho^2) = 1$, where $\mathrm{tr}(\cdots)$ stands for the trace. All four Bell states are maximally entangled pure states. One state that will be of interest to us in this thesis is

$$\rho = \varepsilon \left|\Psi^-\right\rangle\left\langle\Psi^-\right| + \frac{1-\varepsilon}{2}\left[|01\rangle\langle 01| + |10\rangle\langle 10|\right], \tag{2.7}$$

that is a Bell state (maximally entangled) for $\varepsilon = 1$ and a separable state for $\varepsilon = 0$. Therefore the degree of entanglement of this state goes from 1 to 0, when ε also goes from 1 to 0. Initially maximal entangled states can suffer degradation of the quality of entanglement, for instance, where there is a high coupling of the systems with the environment, or when the information of the state is coupled to another system, for instance another degree of freedom (DoF), as we will see in Chapter 4.

2.2 Generation of entanglement

To date, many quantum objects have been used to demonstrate entanglement, such as atoms [17], protons [18] and trapped ions [19]. Moreover, larger objects such as superconducting circuits [20], atomic ensembles [21] or even small diamonds [22] have also been entangled successfully. Unfortunately, entanglement is extremely fragile with respect to interactions with the environment, which makes it increasingly difficult to generate for correspondingly larger objects.

Optics provides a robust platform to generate practically all the important aspects of quantum entanglement. The notable variety of optical elements capable of manipulating all properties of photons makes light the easiest platform to work with. As we will see, two entangled photons can be created using an specific nonlinear medium with particular characteristics.

2.2.1 Nonlinear optics as a tool to generate entanglement

When light traverses a material medium, the molecules of the medium interacts with the electromagnetic field. The relationship of the light-induced polarization of the medium with the electric field of the light can be written

$$\mathbf{P} = \epsilon_0 \chi^{(1)} \mathbf{E} + \epsilon_0 \chi^{(2)} \mathbf{E}\mathbf{E} + \epsilon_0 \chi^{(3)} \mathbf{E}\mathbf{E}\mathbf{E} + ..., \tag{2.8}$$

being ϵ_0 the electric permittivity of vacuum, $\chi^{(1)}$ is the linear electric susceptibility of the medium, $\chi^{(2)}$ is the second-order nonlinear electric susceptibility and $\chi^{(3)}$ is the third-order nonlinear electric susceptibility.

The first term describes the realm of linear optics, and it is used to describe all the linear effects present in optics, such as the origin of the refractive index, reflection, refraction and absorption. For high intensity light beams, and under specific conditions, other terms of the expansion, such as the second and third-order terms of the polarization, are not negligible anymore. These terms are used to describe nonlinear optics effects such as second-harmonic generation, phase-conjugation or the intensity-dependent refractive index.

Spontaneous parametric down-conversion

The principal nonlinear effect that will be considered throughout this thesis is related to the second-order nonlinear coefficient $\chi^{(2)}$, that describes effects such as sum-frequency generation and difference-frequency generation. Here we are interested in the process of spontaneous parametric down-conversion (SPDC), the process most commonly used to generate entanglement, where a pair of photons is generated when a strong pump beam interacts with the molecules of a non-centrosymmetric crystal. The crystals with this kind of asymmetry are the only ones that presents a second-order nonlinear coefficient $\chi^{(2)} \neq 0$.

Spontaneous parametric down-conversion is a particular process, where a high energy photon, usually called the pump photon, is converted into two new photons of lower energy. These two photons are usually called *signal* and *idler* photons for historical reasons, and they can be correlated in many ways and in different degrees of freedom, i.e., polarization, momentum, frequency and spatial shape. There is a long list of materials where the SPDC process can happen. However it is a hot topic of research the finding of new materials where the efficiency of the process can be increased.

In addition to the specific nonlinear nature of the material, there are two more important conditions that must be fulfilled in all the scenarios.

- **Energy conservation**: the sum of the energies of the newly generated photons should be equal to the energy of the incoming pump photon, i.e.,

$$\hbar\omega_p = \hbar\omega_s + \hbar\omega_i, \tag{2.9}$$

where $\hbar$ is the Planck constant divided by 2π, and ω_j ($j = p, s, i$) are the angular frequencies of the pump, signal and idler photons, respectively.

- **Momentum conservation**: the sum of the momenta of signal and idler photons should equal the momentum of the pump photon, i.e.,

  $$\mathbf{k}_p = \mathbf{k}_s + \mathbf{k}_i, \tag{2.10}$$

  where $|\mathbf{k}_j| = k_j = 2\pi n_j/\lambda_j$ are the wave vectors, λ_j are wavelength in vacuum and n_j are refractive index at each wavelength, for the three photons involved in the process. This condition is equivalent to the phase-matching condition. This imply that the refractive index that every field sees inside the medium has to take particular values.

In the particular case where the two outgoing photons in the SPDC process are collinear and have the same wavelength (degenerate SPDC), the phase-matching condition reads

$$\Delta k = |\mathbf{k}_p - \mathbf{k}_s + \mathbf{k}_i| = |\frac{2\pi}{\lambda_s}(2n_p - n_s - n_i)| = 0, \tag{2.11}$$

gives the value that the refractive indexes for the two different wavelengths and polarizations have to obey. This condition is usually fulfilled by using birefringent materials, such as beta barium borate (β-BaB_2O_4 or BBO), potassium titanyl phosphate ($KTiOPO_4$ or KTP) or lithium niobate ($LiNbO_3$) [23]. Controlling the angle between the nonlinear crystal structure and the propagating light beam, or changing the temperature of the material, we can modify the refractive index that the different waves with a particular polarization see within the crystal.

BBO and $LiNbO_3$ are examples of uniaxial birefringent crystals. If all waves propagate along the same direction $\hat{\mathbf{z}}$ in an uniaxial crystal, forming an angle θ with the called optic axis $\hat{\mathbf{o}}$ of the crystal, one can define the principal plane of the crystal as the one containing both

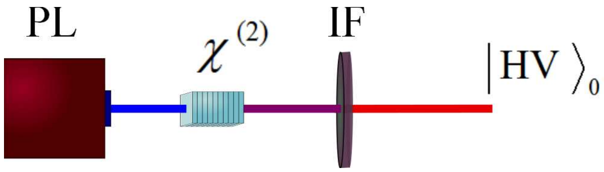

Figure 2.1: SPDC collinear type II scheme resulting in the generation of two photon with orthogonal polarizations: horizontal and vertical polarized. The notation is the following, PL: pumping laser. $\chi^{(2)}$: nonlinear crystal. IF: interference filter.

the propagation direction and the optic axis. Waves with orthogonal polarization to the principal plane are called *ordinary* (o), and waves with polarization contained in the principal plane are called *extraordinary* (e). This orthogonality and the birefringence brings the possibility of matching the same refractive index for different wavelengths and polarizations.

There are different types of SPDC polarization configurations. *Type-0* (eee) when all the polarizations involved are the same, *type-I* (oee) when the two output photons have the same polarization but orthogonal to the polarization of the pump wave, and *type-II* (eoe) when the two outgoing photons have orthogonal polarizations, as shown in Fig. 2.1.

Not all materials with non-zero second-order non-linear coefficient ($\chi^{(2)}$) have the birefringence necessary to fulfil the phase-matching condition in the usual way, by playing with polarization, wavelength or temperature tuning, even when considering all possible types described above. In Chapter 3 we will focus on our work exploiting this issue in order to be able to build more efficient and compact entanglement sources.

2.2.2 Engineering indistinguishability

In order to generate entanglement between two parties, one needs first to generate different correlations between the parties, but it is important as well to turn these different correlations into quantum correlations. For instance, if we want to generate the entangled state

$$\left|\psi^{+}\right\rangle = \frac{1}{\sqrt{2}}(|01\rangle + |10\rangle), \tag{2.12}$$

we need to generate two different types of correlations:

- $|01\rangle$ indicates that when the photon of party A has the value 0, the photon of party B has value 1.
- $|10\rangle$ indicates that when the photon of party A has the value 1, the photon of party B has value 0.

If 0 and 1 would refer to polarizations, this situation would correspond to the photons of both parties being always orthogonal, but each photon being able to have any polarization, horizontal or vertical.

In order to turn these correlations into quantum correlations it is necessary to erase any possible correlation of the photons with any other external system (distinguishing information) that could provide information about the correlations being observed in an experiment. There are many degrees of freedom (DoF) within a photon: spatial, temporal, frequency, modal, polarization, among others. The quality of the entanglement source is highly related to how uncoupled are the not-relevant DoF with respect to the DoF where entanglement information resides.

For instance, if horizontal and vertical photons have different group velocity, due to a different refractive index for each polarization within a birefringent material, we can distinguish the state $|01\rangle$ from $|10\rangle$ because of the different time of arrival sequence of photons to the detectors. Another resulting distinguishability could come from a different spectrum associated to each polarization, because of the dispersive properties of the nonlinear material. Some of the DoF can be uncoupled from the polarization right after the pair generation or even just before the detection is performed, as Gisin

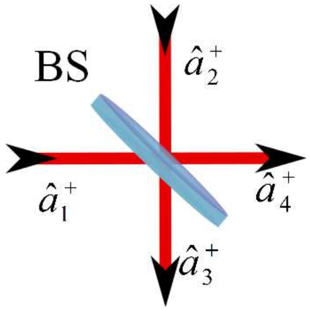

Figure 2.2: Hong-Ou-Mandel effect scheme.

demonstrated [24] by using interference filters to increase the quality of an entanglement source, as the on in Fig. 2.1.

There is a fundamental experiment done by Hong et al. [25] where it can be clearly identified the presence of any distinguishing information. This measurement, called the Hong-Ou-Mandel (HOM) effect, relates the existence of distinguishing information with a measure of visibility. We will use the HOM effect in all experiments to identify the existence of quantum correlations instead of just classical correlations, a key element to create a source of high-quality entanglement.

Hong-Ou-Mandel effect

The HOM effect is a very general idea that can take place with different quantum objects, i.e., photons [25] or atoms [26]. Let us consider the case of photons. If two photons spatially separated are perfectly indistinguishable, when they interfere in a 50:50 beam splitter, as the one depicted in Fig. 2.2, only two of the four possible outcomes indeed happen.

Let us analyse the beam splitter transformations between the four ports by using creation operators:

$$\begin{aligned} \hat{a}_1^\dagger &\rightarrow r\hat{a}_3^\dagger + t\hat{a}_4^\dagger, \\ \hat{a}_2^\dagger &\rightarrow t\hat{a}_3^\dagger + r\hat{a}_4^\dagger. \end{aligned} \tag{2.13}$$

We use particular values of the reflection $r = 1/\sqrt{2}$ and transmission $t = i/\sqrt{2}$ coefficients for a 50:50 symmetric beam splitter. If we take into account that photons in input ports 1 and 2 are completely indistinguishable, the quantum state of the incoming two-photon state after the BS is

$$\hat{a}_1^\dagger \hat{a}_2^\dagger |vac\rangle \rightarrow \frac{1}{2}(\hat{a}_3^\dagger + i\hat{a}_4^\dagger)(i\hat{a}_3^\dagger + \hat{a}_4^\dagger)|vac\rangle = \\ = \frac{1}{2}(i\hat{a}_3^\dagger\hat{a}_3^\dagger + \cancel{\hat{a}_3^\dagger\hat{a}_4^\dagger} - \cancel{\hat{a}_4^\dagger\hat{a}_3^\dagger} + i\hat{a}_4^\dagger\hat{a}_4^\dagger)|vac\rangle = \frac{i}{2}(\hat{a}_3^\dagger\hat{a}_3^\dagger + \hat{a}_4^\dagger\hat{a}_4^\dagger)|vac\rangle\,, \tag{2.14}$$

being $|vac\rangle$ the *vacuum*. Thus, the amplitude of each photon being at a different outcome port cancels out, resulting of having a zero in a coincidence measurement between the two output port detectors.

If there exist any difference between photons in input ports 1 and 2, for example the time of arrival of each photon to the beam splitter, this distinguishing information reflects in the measurement of a non-zero value of coincidences between the detectors in the two output port detectors. Any increase of the number of coincidences detected is a measure of the the amount of distinguishing information present between photons in both input ports.

Post-selection approach

One simple setup to achieve polarization entanglement is the one showed in Fig. 2.3, where all distinguishing information can be filtered out or compensated. When using a beam splitter 50:50 in order to separate the photons in two different paths, 1 and 2, we have four different cases, and the quantum state writes

$$|\psi\rangle = \frac{1}{2}(|H\rangle_1|V\rangle_2 + |V\rangle_1|H\rangle_2 + |H\rangle_1|V\rangle_1 + |H\rangle_2|V\rangle_2). \tag{2.15}$$

This quantum state is not entangled, since an unitary transformation (beam splitter) cannot generate entanglement.

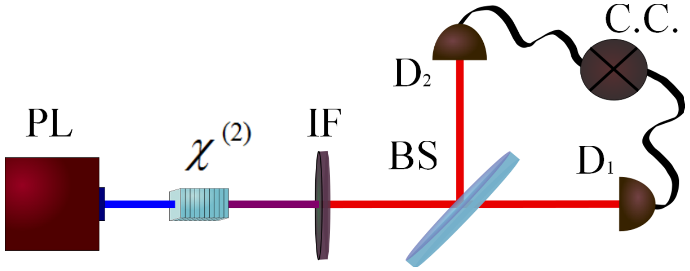

Figure 2.3: Polarization entanglement scheme using the post-selection approach. The notation is the following, PL: pumping laser. $\chi^{(2)}$: nonlinear crystal. IF: interference filter. BS: beam splitter 50:50. $D_{1\&2}$: single-photon detectors. C.C.: coincidence electronics.

One can consider entanglement in a sub-space, by *post-selection*, when we do not consider the cases where the two photons went through the same output port of the beam splitter. With this condition, the quantum state in this sub-space (one photon leaving the BS through one output port, the other photon leaving the BS through the remaining output port) becomes entangled and reads as

$$\left|\psi^+\right\rangle = \frac{1}{\sqrt{2}}(\left|H\right\rangle_1 \left|V\right\rangle_2 + \left|V\right\rangle_1 \left|H\right\rangle_2) = \frac{1}{\sqrt{2}}(\left|HV\right\rangle + \left|VH\right\rangle). \quad (2.16)$$

However, half of the photon pairs generated are lost because of it.

2.3 Bell's inequalities

Since the publication of the famous paper by Einstein et al. [2], discussing how they viewed quantum theory as a correct but incomplete theory, there have been many discussions about the possibility to prove/disprove the existence of a local hidden variable model (LHVM) that could explain all the experimental predictions of quantum theory. In 1964, John S. Bell put forward an inequality [4], that under simple and basic assumptions, could prove that the weird results obtained when measuring correlations in entangled states could

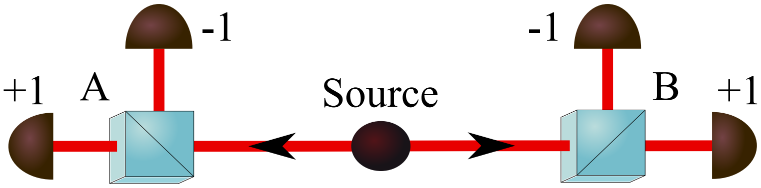

Figure 2.4: Bell inequality simple scheme.

not come from some sort of variables hidden in the parties all the time from its generation.

The most famous and used version of Bell’s inequalities are the CHSH inequality proposed by Clauser et al. [5], that will be the basis of experiments discussed in Chapters 3 and 4. In CHSH, we consider two photons, A and B, entangled in polarization. Each photon can be projected into one of two possible basis: A_1 or A_2 for photon A; B_1 or B_2 for photon B, so there are four possible experiments (see Fig. 2.4):

- **Experiment 1**: Photon A is projected into the basis A_1 with possible results $a_1 = \pm 1$; Photon B is projected into the basis B_1 with possible results $b_1 = \pm 1$.

- **Experiment 2**: Photon A is projected into the basis A_1 with possible results $a_1 = \pm 1$; Photon B is projected into the basis B_2 with possible results $b_2 = \pm 1$.

- **Experiment 3**: Photon A is projected into the basis A_2 with possible results $a_2 = \pm 1$; Photon B is projected into the basis B_1 with possible results $b_1 = \pm 1$.

- **Experiment 4**: Photon A is projected into the basis A_2 with possible results $a_2 = \pm 1$; Photon B is projected into the basis B_2 with possible results $b_2 = \pm 1$.

Under the assumption of the existence of certain hidden variables that determine the results of experiments, and that both parties cannot influence the results of experiments done by the other party, the inequality

$$|\langle S\rangle| = |\langle a_1 b_1\rangle - \langle a_1 b_2\rangle + \langle a_2 b_1\rangle + \langle a_2 b_2\rangle| \leq 2, \tag{2.17}$$

holds. However, using a pair of entangled photons, it can be seen that under appropriate conditions the S inequality bound is violated, being able to increase its value up to $|\langle S\rangle| \leq 2\sqrt{2}$, value commonly known as the Tsirelson's bound [27]. It is important to remark that the violation of a Bell's inequality requires the existence of entanglement. We will use this fact to demonstrate entanglement in some of the sources of entanglement demonstrated in this thesis. However, there exist entangled states that do not violate the inequality [28].

Bell's inequalities can also be used to unveil the presence of an eavesdropper in a cryptographic communication protocol, as it was shown by Ekert [29], or also the amount of coherence that could be recovered from a particular state, as we will be able to demonstrate in Chapter 5.

2.4 View of entanglement as coherent delocalization

The concept of entanglement has been always commonly linked to composite systems made up of two spatially separated subsystems. However, correlations of similar nature to the ones existing between physically separated subsystems may also exist when considering different degrees of freedom (DoF) of a single system [30]. Indeed, entanglement can be measured in this kind of systems, provided that one is able to perform independent measurements in the DoF involved.

Along these lines, Gadway et al. [31] demonstrated the presence of entanglement by measuring correlations in two degrees of freedom, polarization and path, of a single photon. Violation of Bell-like inequalities has also been used to characterize properties of classical beams containing many photons, i.e., intense beams. Borges et al. [32] considered coherent beams whose total electric field writes $\mathbf{E}(\mathbf{r}) = \Psi_H(\mathbf{r})\,\hat{\mathbf{e}}_H + \Psi_V(\mathbf{r})\,\hat{\mathbf{e}}_V$, and used a CHSH inequality [5] to characterize their coherence properties in one of the two degrees of freedom involved. Kagalwala et al. [33] added the consideration of partially coherent beams and also considered the relationship between the degree of Bell inequality violation and the degree of partial coherence in each degree of freedom. Svozilík et al. (see [34] and Chapter 5) demonstrated the clear link between amount of available coherence that can be unveiled by a global unitary transformation and the degree of violation of the CHSH inequality. The so-called *non-quantum entanglement* is being considered as a fundamental tool for investigating important properties of classical fields [35–40].

In this section we show that by looking at what is entanglement in specific, physically realistic scenarios, one can get a better understanding of what it means to be entangled. We will see that when considering systems in the single-excitation manifold, entanglement will always exist as long as the excitation is *coherently delocalized*. We will refer here to coherence as first-order coherence [41, 42], and delocalization as the fraction of parameter space where the single-excitation takes place. In general, coherence and entanglement do not imply each other, and might address different aspects of a particular physical system. However, in the single-excitation manifold [43], coherence and entanglement can become mathematically equivalent. In this particular regime the presence of entanglement entails coherence and vice versa, which means that any measure of entanglement is also a measure of coherence [44–47].

The consideration of the single-excitation regime could be seen as overrestricting our analysis. However, the great majority of studies of entanglement, both theoretical and experimental, can be easily demonstrated to belong to this category. Surely, the implications of being entangled in different contexts might not be the same, especially when considering subsystems spatially far away from each other. Notwithstanding, a common conceptual understanding of entanglement in all of these different scenarios is still valid and illuminating. For the sake of simplicity, and keeping a common notation, we will use a quantum language to describe all scenarios, even when we refer to systems that might as well be described using classical concepts.

In what follows, we will be more specific about what *single-excitation* regime, *localization* and *coherence* mean. By using different scenarios, the different terms will be described. Even though the appearance of entanglement in some of these cases might cause certain surprise, we will show that its presence should not be unexpected if one realizes that such systems can be described within the single-excitation manifold, and are therefore completely analogous to the systems where entanglement is usually considered. For that reason we will introduce the concepts starting from the most intriguing scenario.

2.4.1 Entanglement in light-harvesting complexes

Due to its importance and relevance for explaining and describing life on earth, photosynthetic light-harvesting complexes have been a topic of study for decades [48]. In recent years, they have attracted a renewed attention [49–51] mainly due to the experimental observation of long-lived electronic coherences in the energy transfer process of bacterial and algal light-harvesting complexes [52–55]. Although the relevance of some quantum-born concepts, such as entanglement, for explaining the highly efficient energy transport observed in photosynthetic systems is still under discussion [56–60], we will show that the presence of entanglement should not be unexpected anyway. In the following, we will see that the appearance of entanglement is a direct consequence of considering a coherent nature of the photosynthetic complex, provided the state describing its dynamics is defined within the single-excitation manifold.

In general, a single excitation in a network of N chromophores (or sites) can be represented by a density matrix of the form

$$\rho = \epsilon \left|\psi\right\rangle \left\langle\psi\right| + (1-\epsilon)I_D, \tag{2.18}$$

where

$$\begin{aligned} \left|\psi\right\rangle &= \sum_i^N \alpha_i \left|i\right\rangle, & (2.19)\\ I_D &= \sum_i^N \left|\alpha_i\right|^2 \left|i\right\rangle \left\langle i\right|, & (2.20)\end{aligned}$$

with $\left|i\right\rangle$ indicating that the excitation is on site i with probability $p_i = \left|\alpha_i\right|^2$. The key consideration of *single-excitation* implies that only one site at any time can be in the excited state. The parameter ϵ determines the degree of coherence of the system.

In order to quantify coherence we make use of the degree of coherence, a function that corresponds to the absolute value of the normalized first-order coherence function [61]. We can then write the degree of coherence as

$$g_{ij}^{(1)} = \frac{\mathrm{tr}\left(\rho\sigma_i^\dagger\sigma_j\right)}{\left[\mathrm{tr}\left(\rho\sigma_i^\dagger\sigma_i\right)\mathrm{tr}\left(\rho\sigma_j^\dagger\sigma_j\right)\right]^{1/2}}, \tag{2.21}$$

where $\sigma_i^\dagger$ and σ_i are the raising and lowering operators for the ith site, respectively, and $\mathrm{tr}\left(\cdots\right)$ stands for the trace. Making use of Eqs. (2.19) and (2.20), it is straightforward to find that for the state in Eq. (2.18), the degree of coherence writes

$$\left|g_{ij}^{(1)}\right| = \epsilon, \text{ for all } i \neq j. \tag{2.22}$$

Notice from Eq. (2.22) that, depending on the value ϵ, the degree of coherence can take values from 0, when there is no coherence, to 1, for a fully coherent system.

For the sake of simplicity, and to make more compelling the comparison with the other cases that will be discussed below, we restrict our attention to the case of two coupled sites or dimer. In this scenario, the density matrix in Eq. (2.18), in the basis $\{|1\rangle, |2\rangle\}$, reads

$$\rho = \begin{pmatrix} |\alpha_1|^2 & \epsilon\alpha_1^*\alpha_2 \\ \epsilon\alpha_1\alpha_2^* & |\alpha_2|^2 \end{pmatrix}. \tag{2.23}$$

Different measures, such as global entanglement [44] and logarithmic negativity [62], have been used for quantifying entanglement in light-harvesting complexes. Here, we will quantify the amount of entanglement present in a two-site system by making use of the concurrence [13,63], which for a density matrix of the form (2.23) is given by

$$C = 2\,\max\{0, \epsilon\sqrt{p_1\, p_2}\} = 2\epsilon\sqrt{p_1\, p_2}. \tag{2.24}$$

Finally, to quantify the degree of excitation's delocalization in the system given by Eq. (2.23), we introduce a measure of delocalization that can be defined as

$$D = 2\sqrt{p_1\, p_2}. \tag{2.25}$$

According to Eq. (2.25), if the excitation spreads equally over all sites (maximum delocalization), i.e., $p_1 = p_2 = 1/2$, one obtains $D = 1$; whereas if the excitation resides in a single site (maximum localization), i.e., $p_1 = 1$ and $p_2 = 0$, or $p_1 = 0$ and $p_2 = 1$, we obtain $D = 0$. Notice that local unitary transformations that affect the excitation in sites 1 and 2 independently do not affect the value of D. Moreover, for a coherent state ($\epsilon = 1$), Eq. (2.23) is equivalent to the Schmidt decomposition of the system [64], which justifies the validity of D as a good measure of the excitation's delocalization in the system.

Figure 2.5(a) shows the amount of entanglement (as quantified by the concurrence) as a function of the degree of coherence $[g_{12}^{(1)}]$ for a fixed value of the degree of delocalization. For a given delocalization, the degree of entanglement increases for increasingly larger values of the coherence. Also, Fig. 2.5(b) shows the amount of entanglement

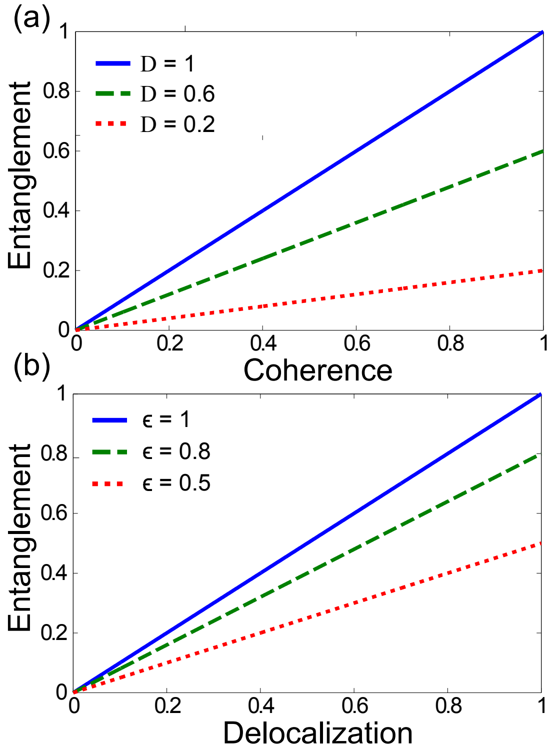

Figure 2.5: Entanglement, as quantified by the concurrence, as a function of: (a) degree of coherence ϵ; and (b) delocalization D of the single excitation.

as a function of the degree of delocalization for a fixed value of the coherence. Notice that also in this case, increasingly larger values of delocalization provide larger values of entanglement.

Using Eqs. (2.21), (2.24) and (2.25), and the results provided in Fig. 2.5, one can find that

$$\text{Entanglement} = \text{Delocalization} \times \text{Coherence}.$$

From this relationship, we can conclude that maximum entanglement always requires a maximum delocalization of the excitation with maximum degree of coherence. This situation has been defined by previous authors as *coherent delocalization* [65]. In contrast, a maximally delocalized excitation ($D = 1$) with no coherence, the so-called *incoherent delocalization*, produces no entanglement. Finally, as one can naturally expect, a fully coherent system with maximum localization ($D = 0$) will not exhibit entanglement.

In the following sections, we will show that similar results can explain the presence or lack of entanglement in different scenarios. Even though in the cases that we will describe below there is not an actual excitation being shared by the subsystems, we will borrow this term from the present discussion and use it to describe physical operations that modify certain properties of a photon, i.e., its polarization or its orbital angular momentum content. In this way, we will be able to define "ground" and "excited" states of each subsystem, thus allowing us to demonstrate the mathematical equivalence of all the cases considered in this work.

2.4.2 Polarization entanglement in a two-photon state

Polarization entanglement is the most common type of photonic entanglement, widely used in many quantum computing and quantum information applications [66, 67], mainly because of the ease with which it can be generated and manipulated, as can be seen in experiments of Chapter 3.

In general, the density matrix of the two-photon system can be written in the same form as Eq. (2.18), with

$$\begin{aligned} |\Psi\rangle &= \alpha_1 |\mathrm{H}\rangle_s |\mathrm{V}\rangle_i + \alpha_2 |\mathrm{V}\rangle_s |\mathrm{H}\rangle_i \,, && (2.26)\\ I_D &= |\alpha_1|^2 |\mathrm{H}\rangle_s |\mathrm{V}\rangle_i \langle\mathrm{H}|_s \langle\mathrm{V}|_i + |\alpha_2|^2 |\mathrm{V}\rangle_s |\mathrm{H}\rangle_i \langle\mathrm{V}|_s \langle\mathrm{H}|_i \,, && (2.27)\end{aligned}$$

where $|\mathrm{H}\rangle$ and $|\mathrm{V}\rangle$ stand for horizontal and vertical polarization states, respectively, and s, i are the commonly used labels for the signal and idler photons. Here, the values of $\alpha_{1,2}$ depend on specific polarization-dependent characteristics of the photon-generation process [68].

One can realize that the two-photon state defined by Eq. (2.26) is equivalent to considering a two-site state in the *single-excitation* manifold by identifying the corresponding "ground" and "excited" states of each photon (or subsystem). For this, we can take $|\mathrm{V}\rangle_{s,i}$ as the ground states and $|\mathrm{H}\rangle_{s,i}$ as the excited states, so we find that the state given by Eq. (2.26) lives in a Hilbert subspace where only one of the two photons can be in the excited state, that is, the single-excitation subspace.

The degree of coherence of this system can be written as

$$g^{(1)}_{H_sV_i;V_sH_i} = \frac{\mathrm{tr}\left(\rho A^{\dagger}_{H_sV_i} A_{V_sH_i}\right)}{\left[\mathrm{tr}\left(\rho A^{\dagger}_{H_sV_i} A_{H_sV_i}\right) \mathrm{tr}\left(\rho A^{\dagger}_{V_sH_i} A_{V_sH_i}\right)\right]^{1/2}}, \tag{2.28}$$

where $A^{\dagger}_{H_sV_i} = (a^{\dagger}_{H_s} a^{\dagger}_{V_i})$ and $A^{\dagger}_{V_sH_i} = (a^{\dagger}_{V_s} a^{\dagger}_{H_i})$, with $a^{\dagger}_{H_s,V_s}$ and $a^{\dagger}_{V_i,H_i}$ being the operators that create signal (s) and idler (i) photons with horizontal (H) and vertical (V) polarizations. Using Eqs. (2.18), (2.26) and (2.27), one obtains that the degree of coherence reads

$$\left|g^{(1)}_{H_sV_i;V_sH_i}\right| = \epsilon, \tag{2.29}$$

which is a result that one can anticipate from Eq. (2.22). On the other hand, it is easy to see that $D = 2|\alpha_1||\alpha_2|$.

Concurrence is again used for quantifying entanglement in this system, as well as Eq. (2.25) for the excitation's degree of localization. Notice that, in the present scenario, maximum delocalization ($D = 1$) designates the case where pairs of photons with polarization $|\mathrm{V}\rangle_s |\mathrm{H}\rangle_i$ are as likely to be generated as photons with polarization $|\mathrm{H}\rangle_s |\mathrm{V}\rangle_i$. Indeed, the same results as those discussed in the previous section can be obtained for the two-photon case, which means that measuring entanglement in this system is fully equivalent to measuring coherence.

Experimentally, the quantum state described by Eqs. (2.26) and (2.27) may be generated by using two second-order nonlinear crystals, where degenerate and collinear type-II SPDC can take place. The input pump beam is divided with the help of a beam splitter and illuminates both crystals. The probability of generating two pairs of photons, one pair in each crystal, is assumed to be negligible for sufficiently low values of the pumping power. Then, down-converted photons of each crystal are redirected to a polarizing beam splitter (PBS), where they enter through different input ports. In this way, in each output port of the PBS, horizontally and vertically polarized photons can be detected. The probabilities $p_{1,2}$ that the pair of photons originates in each of the two crystals may be engineered in several ways. For instance, one can control the phase-matching conditions, or the amount of pump power, independently in each crystal, effectively varying p_1 and p_2, and so D. In the case where all pairs of photons come from a single crystal one would obtain $D = 0$; whereas in the case when the pumping power and phase-matching conditions are equal in both crystals, one would have $D = 1$. The coherence ϵ can be controlled by introducing/removing delays between paired photons originating from different crystals, which effectively introduces/erases distinguishability between them [68].

It is important to remark that a two-photon entangled state could be described by a state of the form $|\Psi\rangle = \alpha_1 |\mathrm{V}\rangle_s |\mathrm{V}\rangle_i + \alpha_2 |\mathrm{H}\rangle_s |\mathrm{H}\rangle_i$. Note that, in this case, the signal photon’s polarization is rotated, which means that, in order to remain in the single-excitation manifold, its corresponding “excited” and “ground” states should rotate as well. Using these new states one can obtain the same results as the ones discussed previously. Finally, we highlight the fact that the density matrix of the two-photon system lies in the single-excitation subspace allows one to implement experimental setups, such as the one described in Ref. [69], in which the degree of entanglement between the two photons is controlled by directly modifying the offdiagonal terms of the system's density matrix, that is, the degree of coherence.

2.4.3 Spin-orbit entanglement in single photons

The spatial shape of photons, or its orbital angular momentum (OAM) content, is a degree of freedom that has received increasing attention in the last few years, because it has opened a new window, easily accessible experimentally, to explore high-dimensional quantum spaces encoded in single- or two-photon systems [70, 71].

Let us consider the case of a single-photon state in which the OAM and polarization degrees of freedom are used. It has been shown that it is possible to generate single-photon states in which the spatial shape and polarization degrees of freedom are effectively entangled [72, 73]. In this scenario, the quantum state of the photon would be described by the so-called single-photon spin-orbit state, whose density matrix has the same form as Eq. (2.18), with [74, 75]

$$\begin{aligned} |\Psi\rangle &= \alpha_1 |H,-1\rangle + \alpha_2 |V,+1\rangle \,, && (2.30)\\ I_D &= |\alpha_1|^2 |H,-1\rangle\langle H,-1| + |\alpha_2|^2 |V,+1\rangle\langle V,+1| \,. && (2.31) \end{aligned}$$

Here, the integer ±1 corresponds to the value of the OAM index ($m = \pm 1$) of the photon.

Again, we can see that the single-photon spin-orbit state lies within the single-excitation manifold by identifying the "ground" and "excited" states for each subsystem. If we define $|\mathrm{V}\rangle$ and $|-1\rangle$ as the ground states, and $|\mathrm{H}\rangle$ and $|+1\rangle$ as the excited states for the polarization and OAM degrees of freedom, we can readily find that Eqs. (2.30) and (2.31) describe a state that is equivalent to a Hilbert subspace where only one "excitation" in any of the two degrees of freedom can exist, i.e., the single-excitation subspace.

Following the same procedure as in previous sections, we can quantify coherence in the single-photon system by writing the first order correlation function as

$$g^{(1)}_{H-1;V+1} = \frac{\mathrm{tr}\left(\rho a^{\dagger}_{H-1} a_{V+1}\right)}{\left[\mathrm{tr}\left(\rho a^{\dagger}_{H-1} a_{H-1}\right) \mathrm{tr}\left(\rho a^{\dagger}_{V+1} a_{V+1}\right)\right]^{1/2}}, \tag{2.32}$$

where $a^{\dagger}_{jm}$ is the operator that creates a photon with the polarization state $j = H, V$ and OAM index $m = \pm 1$.

Using Eqs. (2.18), (2.30) and (2.31) we thus find that the degree of coherence of the single-photon system is given by

$$\left| g^{(1)}_{H-1;V+1} \right| = \epsilon. \tag{2.33}$$

Finally, for quantifying entanglement in this system, we can make use of the basis $\{|\mathrm{H}, +1\rangle, |\mathrm{H}, -1\rangle, |\mathrm{V}, +1\rangle, |\mathrm{V}, -1\rangle\}$ to write the density matrix of the single-photon system, and find that it has the exact same form as the one described in Eq. (2.23). It is then straightforward to obtain that the concurrence for this state is $C = 2\epsilon\sqrt{p_1 p_2}$.

In experiments as the one showed in Chapter 4, the quantum state described by Eqs. (2.30) and (2.31) may be generated by making use of a single-crystal collinear type-II SPDC configuration. In this configuration, one of the photons is projected into different polarization states while the remaining photon traverses an optical device that correlates polarization with OAM. We can control the values of $p_{1,2}$, and therefore D, by defining a proper polarization-state projection. For instance, by projecting one photon into the polarization state $|\mathrm{H}\rangle$, the remaining photon would be in the state $|\mathrm{V}, -1\rangle$, and therefore $D = 0$. Similarly, $D = 0$ if we project the photon into the polarization state $|\mathrm{V}\rangle$. Interestingly, if we project one photon into the state $|\mathrm{H}\rangle + |\mathrm{V}\rangle$, the remaining photon will be in a quantum superposition of both states, thus giving us a maximum value of delocalization, $D = 1$. Also, as discussed in the previous case, coherence can be controlled by introducing/removing delays between the generated pairs of photons.

Finally, from the results discussed in this section, we can conclude that measuring entanglement in a single-photon spin-orbit system is the same as measuring coherence. By identifying that the single-photon spin-orbit state lies within the single-excitation manifold, we can anticipate the existence of entanglement between the spin and OAM degrees of freedom, provided that coherence between them is preserved.

CHAPTER

THREE

GENERATION OF ENTANGLEMENT IN BRAGG REFLECTION WAVEGUIDES

3.1 Introduction

Entanglement is one of the most fundamental concepts in quantum information science, with profound implications regarding the way quantum mechanics describes Nature. Besides this, it is also a basic ingredient of many of the technological applications that has been put forward in quantum communications and quantum computing [76,77] in the last two decades. Entanglement can reside in any of the degrees of freedoms that characterize light: angular momentum (polarization and orbital angular momentum), momentum and frequency, or in several of them, what is known as hyper-entanglement. Undoubtedly, polarization, which provides a Hilbert space of dimension 2, is the most widely resource used to generate entanglement between photons, thanks to the existence of many optical elements that can control the polarization of light and to the easiness of its manipula-

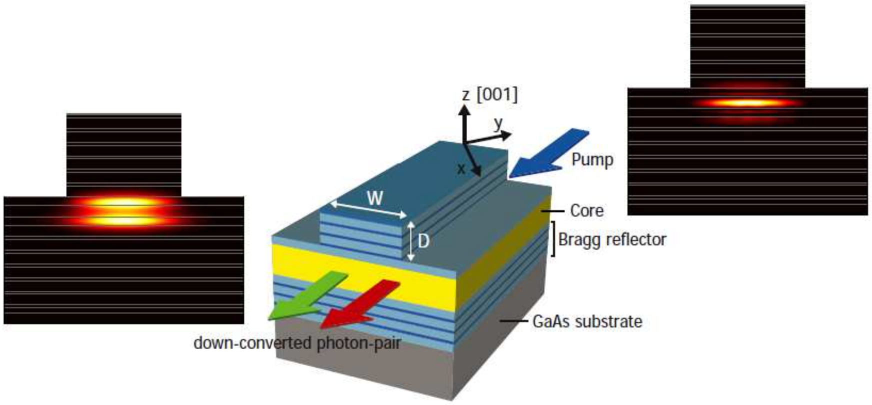

Figure 3.1: Bragg reflection waveguide structure used to generate paired photons correlated in time and polarization (type-II SPDC) at the telecommunication window (1550 nm). The insets show the spatial shape of the pump mode that propagates inside the waveguide as a Bragg mode, and the spatial shape of the down-converted, which are modes guided by total internal reflection (TIR). W: width of the ridge; D: depth of the ridge.

tion when compared to other characteristics of a light beam, e.g., its spatial shape or bandwidth.

The implementation of entanglement-based photonic technologies should consider the development of high-efficient, compact, and highly tunable sources of entangled photons. High efficiency helps to reduce the pump power required to generate a high flux of down-converted photons, and broad tunability allows the preparation of different types of quantum states. Compactness makes possible to use the entanglement source under a greater variety of circumstances, such as, for instance, would be the case in free space applications [78]. Along these lines, the use of waveguides is very advantageous. Contrary to the case of spontaneous parametric down-conversion (SPDC) in bulk crystals, where a very large number of spatial modes is generated, and only a few of them effectively contribute to the generated entangled state, the use of waveguides allows the reduction of the number of modes to a few guided modes [79], and, in this way, it contributes to enhance the overall efficiency of the nonlinear interaction [80].

The capability of integration of the SPDC source with other elements, such as the pumping laser or optical circuits, in a single platform, might be crucial for the implementation of entanglement-based quantum circuits in an out-of-the-lab environment. Semiconductor technologies are nowadays a mature technology that offers a myriad of possibilities, and that allows the fabrication of an integrated monolithic source of entangled photon pairs. Bragg reflection waveguides (BRWs) in AlGaAs could make possible the integration of all of these elements in a single semiconductor platform.

In the last few years, different nonlinear optics processes have been observed experimentally in AlGaAs BRWs, such as second-harmonic generation [81,82], difference-frequency generation [83] and spontaneous parametric down-conversion [84]. Also, BRWs have been demonstrated as edge-emitting diode lasers where the fundamental lasing mode is a photonic bandgap mode or a Bragg mode [85], and electrically pumped parametric fluorescence was demonstrated subsequently [86].

GaAs based waveguides show a broad transparency window ($1-17\ \mu$m), large damage threshold, low linear propagation loss and an extremely high non-linear coefficient [87]. This high nonlinear coefficient ($\chi^{(2)} \approx 240\,\mathrm{pm/V}$) [88] can provide around one order of magnitude greater efficiency, when compared with other nonlinear materials, such as KDP and $\mathrm{LiNbO_3}$, more well-known for frequency conversion. However, these materials show a large birefringence that makes easier its manipulation to obtain the required phase-matching conditions for efficient parametric down-conversion.

GaAs is an isotropic material, it does not show birefringence. Regardless of this, phase-matching can nevertheless be reached by using modal phase-matching between beams with different frequency. The higher frequency beam in parametric down-conversion should propagate as a photonic bandgap mode, or Bragg mode, and the lower frequency light beam should propagate as an usual guided mode, with evanescent decay into the substrate (see Fig. 3.1) [89]. Fortunately, strong modal dispersion in BRWs offers significant control over the properties of down-converted photons, i.e., the spectral width [90] of the photons and the type of spectral correlations between the photons emitted [91].

In this chapter, we demonstrate experimentally that the use of BRWs allows the generation of highly entangled pairs of photons in polarization at the telecom band via the observation of the violation of the Clauser-Horne-Shimony-Holt (CHSH) Bell-like inequality [5]. Bell's inequalities are a way to demonstrate entanglement [92], since the violation of a Bell's inequality makes impossible the existence of one joint distribution for all observables of the experiment, returning the measured experimental probabilities [93].

In a previous work [84], the existence of time-correlated paired photons generated by means of SPDC in BRWs was reported, but the existence, and quality, of the entanglement present was never explored. The generation of polarization entanglement in alternative semiconductor platforms has been demonstrated also in a silicon-based wire waveguide [94], making use of four-wave mixing, a different nonlinear process to the one considered here, and in an AlGaAs semiconductor waveguide [95], where as a consequence of the opposite propagation directions of the generated down-converted photons, two type-II phase-matched processes can occur simultaneously.

3.2 Device description and SHG characterization

Different layers in a BRW need to have particular Al and Ga concentrations, that determines the refractive index of each layer. Moreover, we should be able to vary the layer widths because of the need of having distinct modal propagation within the waveguide for dif-

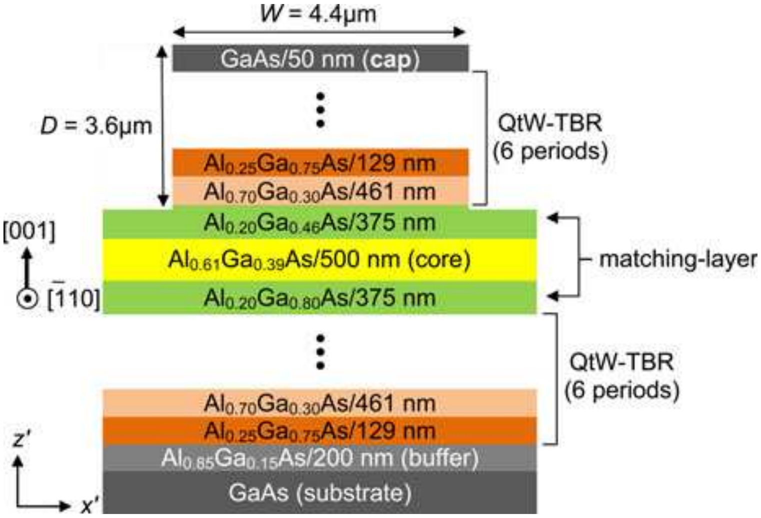

Figure 3.2: Epitaxial structure design of the BRW sample used in the experiments described in this chapter [87].

ferent wavelengths. With the proper design, the optical width of the cluster layers is equal to $\Delta w = \lambda/4$ just for a certain wavelength (λ). With this technique we can achieve destructive or constructive interference in certain parts of the waveguide, being able to generate the particular mode to obtain the desired modal phase-matching [96].

3.2.1 Structure design

A scheme of the BRW used in the experiment is shown in Fig. 3.2. Grown on an undoped (001) GaAs substrate, the epitaxial structure has a three-layer waveguide core consisting of a 500 nm thick $Al_{0.61}Ga_{0.39}As$ layer and a 375 nm $Al_{0.20}Ga_{0.80}As$ matching-layer on each side. These layers are sandwiched by two symmetric Bragg reflectors, consisting each of six periods of 461 nm $Al_{0.70}Ga_{0.30}As$/129 nm $Al_{0.25}Ga_{0.65}As$. A detailed description of the epitaxial structure can be found in [96]. The wafer was then dry etched along (110) direction to form ridge waveguides with different ridge widths. The device under test has a ridge width of 4.4 μm, a depth of 3.6 μm and a length of 1.2 mm.

For this particular case we will refer to the *ordinary* and *extraordinary* waves as *transverse-electric* (TE) and *transverse-magnetic* (TM), respectively. Taking into account the new notation for the polarization, this structure supports three distinct phase-matching schemes for SPDC, namely:

- *type-0* process where all three interacting photons are TM-polarized.
- *type-I* process where the pump is TM-polarized and the down-converted photon pairs are both TE-polarized;
- *type-II* process where the pump is TE-polarized while the photons of a pair have mutually orthogonal polarizations [87].

For the experiments described in this thesis, we investigate type-II SPDC, which is the nonlinear process that produce the polarizations of the down-converted photons required to generate polarization entanglement after certain operation. In particular, since both photons show orthogonal polarizations, after traversing a non-polarizing beam splitter (BS), introducing in advance an appropriate temporal delay between, and filtering out the distinguishing spectral information between both photons, they can result in a polarization-entangled pair when a *post-selection* process is electrically implemented to discard the cases where the two photons exits the BS by the same port.

3.2.2 Sample characterization

During the fabrication process of the BRW, slight changes in the thickness and aluminium concentration of each layer result in small displacements of the actual phase-matching wavelength from the design wavelength. For this reason, we first use second harmonic generation (SHG), before examining SPDC, to determine the pump phase-

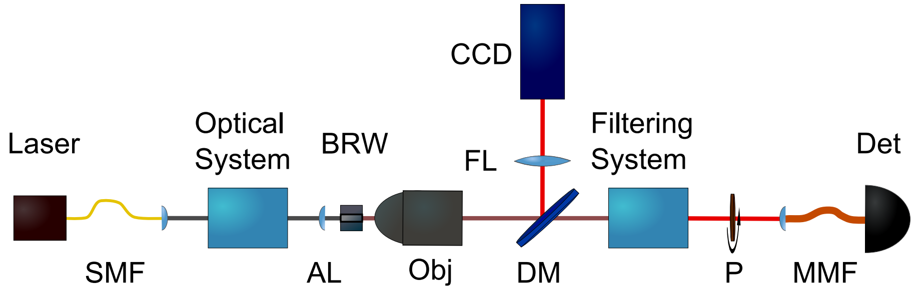

Figure 3.3: Experimental setup for SHG. The pump laser is a tunable external-cavity semiconductor laser (TLK-L1550R, Thorlabs). The Optical System consists of a linear power attenuator (LPA), polarizing beam splitter (PBS) and a half-wave plate (HWP). The Filtering System consists of a neutral density filter (NDF) and short-pass filter (SPF). SMF: single-mode fibre. AL: aspheric lens. BRW: Bragg reflection waveguide. Obj: Nikon 50×. DM: dichroic mirror. FL: Fourier lens. CCD: Retiga EXi Fast CCD camera (QImaging). P: polarizer. MMF: multi-mode fibre. Det: single-photon counting module (SPCM, PerkinElmer).

matching wavelengths for which the different schemes (type-0, type-I or type-II) are phase-matched.

The experimental arrangement for SHG is shown in Fig. 3.3. The wavelength of a single-frequency tunable laser (the fundamental beam) was tuned from 1545 nm to 1575 nm. An optical system shapes the light into a Gaussian-like mode, which is coupled into the BRW to generate the second harmonic beam by means of SHG. At the output, the power of the second harmonic wave is measured to determine the efficiency of the SHG process.

Figure 3.4(a) shows the phase-matching tuning curve i.e., how the generated second-harmonic power depends on the fundamental wavelength. From the figure, three resonance SH features could be resolved corresponding to the three supported phase-matching schemes. As mentioned earlier, the process of interest here is type-II. For this

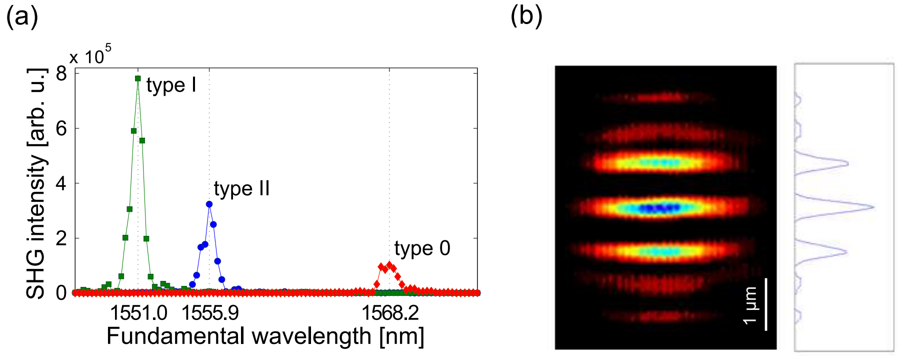

Figure 3.4: (a) Phase-matching curve of the BRW as a function of the wavelength of the fundamental wave. (b) Beam profile of the Bragg mode of the second harmonic wave generated by means of the SHG process, captured with a CCD camera after imaging with a magnification optical system of 100× (Fourier lens with focal length f=400 mm).

particular type of phase-matching, maximum efficiency takes place at the fundamental wavelength of 1555.9 nm. To generate the second harmonic beam by means of type-II SHG in Fig. 3.4(a), we use a half-wave plate to rotate the polarization of the fundamental light coming from the laser by 45-degrees, to generate the required fundamental beams with orthogonal polarizations.

As we said earlier at the beginning of this section, phase-matching in BRW takes place between different types of guided modes which propagate with different longitudinal wavevectors. The fundamental beam (around 1550 nm) corresponds to a total internal reflection (TIR) mode, and the second harmonic beam (around 775 nm) is a Bragg mode. The spatial profile of the Bragg mode is measured with an enhanced signal-to-noise ratio CCD camera, by means of decreasing the temperature of the sensors in order to diminish the background noise or dark counts. The capture of the spatial mode and the plot of the intensity profile of the resulting beam at 775 nm, are shown in Fig. 3.4(b).

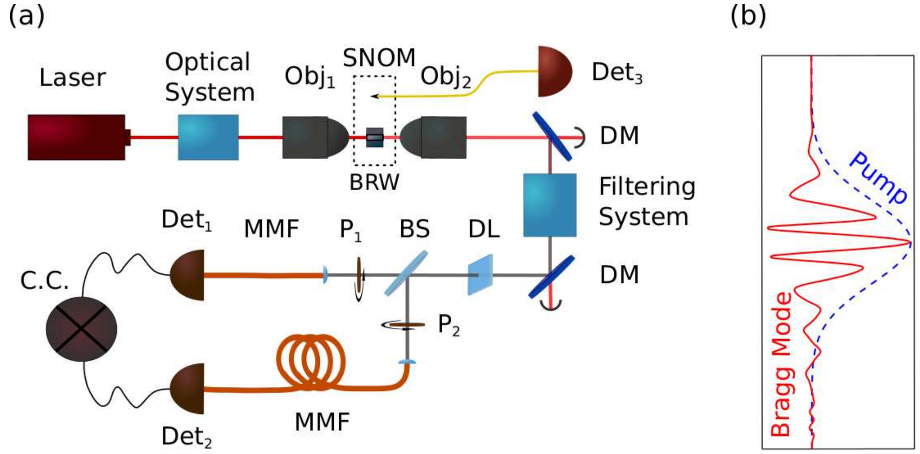

Figure 3.5: (a) Experimental setup for SPDC. The Optical System is composed of a linear power attenuator (LPA), spatial filter (SP) and beam expander (BE). SNOM: scanning near-field optical microscope probe. BRW: Bragg reflection waveguide. Objectives: Obj$_1$ (Nikon 100×) and Obj$_2$ (Nikon 50×). DM: dichroic mirror. Filtering System: 2 DMs, band-pass filter (BPF) and long-pass filter (LPF). DL: delay line (birefringent plate). BS: beam splitter. P$_{1\&2}$: linear film polarizers. MMF: multi-mode fibre. D$_{1\&2}$: InGaAs single-photon counting detection modules. D$_3$: low-power silicon detector. C.C.: coincidence-counting electronics. (b) Amplitude profiles of the theoretical Bragg mode and the Gaussian-like pump beam.

3.3 Experimental setup

The experimental setup used to generate polarization-entangled pairs of photons and the measurement of the violation of a Bell-like inequality is shown in Fig. 3.5(a). The generation of the appropriate shape of the pump beam to couple it to a waveguide mode was of great importance for this experiment. For that reason, we will describe the setup in two parts: first, the preparation of the pump beam, and secondly the measurement of the entanglement.

3.3.1 Setting the appropriate characteristics of the pump beam

The pump laser is a tunable single-frequency diode laser with an external-cavity (DLX 110, Toptica Photonics) tuned to 777.95 nm. Light from the laser traverses an optical system, with an attenuator module, spatial filter and beam expander, in order to obtain a proper input beam.

Even though the optimum option for exciting the pump Bragg mode would be to couple the beam directly into the photonic bandgap mode using a spatial light modulator (SLM), the small size of the characteristic features of the field profile of the Bragg mode and its oscillating nature imposed serious challenges for using an SLM. Therefore, we choose instead to pump the waveguide with a tightly focused Gaussian pump beam (see Fig. 3.5(b)) with a waist of $\sim 1.5\ \mu$m, that is coupled into the waveguide using a 100× objective. Our calculations show that the estimated modal overlap between the Gaussian pump beam and the Bragg mode of the waveguide is around 20%, which should be added to the total losses of the system.

A scanning near-field optical microscope (SNOM) probe was attached to the BRW support, in order to perform sub-micrometric 3D beam profile scans to maximize the coupling efficiency of the incident pump beam into the pump Bragg mode. The power of the laser light before the input objective was measured to be 13 mW. Taking into account the transmissivity of the objective for infrared light (70%), the transmissivity of the facets of the BRW (73%) and the calculated overlap between the laser light and the Bragg mode of the waveguide (around 20%), the estimated pump power available for SPDC process inside the waveguide is ~ 1.3 mW.

Figures 3.6 to 3.9 show some pictures taken from the setup used to characterize the samples, and parts of the setup that are being described in this section.

3.3.2 Measuring the relevant properties of the down-converted photons generated

The generated down-converted photons are collected using a 50× objective and separated from the pump photons using four dichroic mirrors (DM), band-pass and long-pass filters. Each DM has a 99% transmissivity at the pump wavelength. The attenuation of the band-pass filter (45 nm FWHM bandwidth centred at 1550 nm) is 10^{-4}, and the long-pass filter (cut-on wavelength: 1500 nm) introduces an additional attenuation of 10^{-3} at the pump wavelength.

In general, photons propagating in a waveguide with orthogonal polarizations have different group velocities (group velocity mismatch, GVM), which in conjunction with non-negligible group velocity dispersion (GVD), result in different spectra for the cross-polarized photons [97]. As a consequence, the polarization and frequency properties of the photons are coupled. The two photons of a pair could be, in principle, distinguished by their time of arrival at the detectors, as well as their spectra, which drastically reduces the quality of polarization entanglement achievable. In order to obtain high-quality polarization entanglement, it is thus necessary to remove all the distinguishing information coming from the temporal/frequency degree of freedom. For this reason, a 45 nm band-pass filter was applied to remove most of the distinguishing spectral information, and off-chip compensation was implemented with a delay line to remove arrival time information.

The calculated group velocities for TE and TM down-converted photons are 8.98×10^{7} m/s and 9.01×10^{7} m/s, respectively. The GVD parameter is $D \sim$ -7.9×10^{2} ps/(nm·km) for both polarizations. When considering these values of the GVM and GVD, our calculations show that the optimum delay for generating the highest degree of polarization entanglement is $\sim$ 31.2 fs. A quartz birefringent plate with a length of 1 mm, vertically tilted around 30° was used to introduce a $\sim$ 32 fs time delay between photons, which is the optimum value to erase temporal distinguishing information caused by the group veloc-

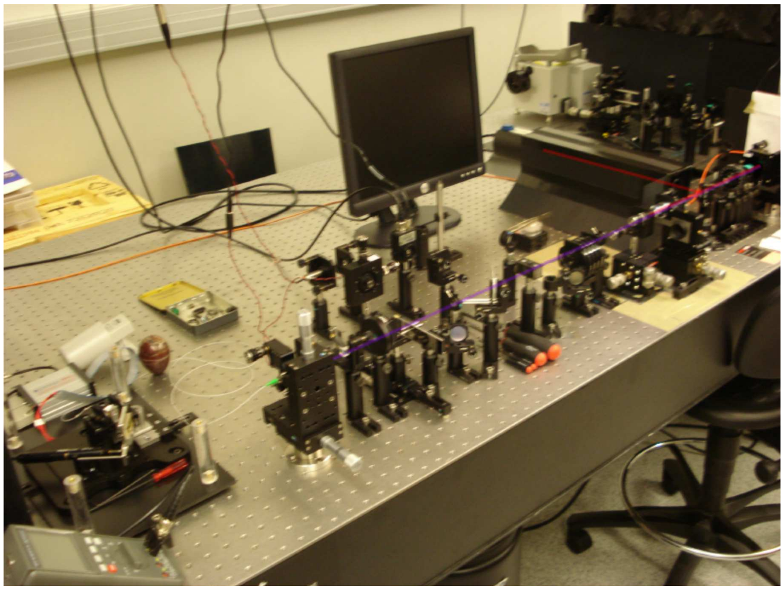

Figure 3.6: Picture of the section of the setup used to characterize the BRW sample by means of Second Harmonic Generation.

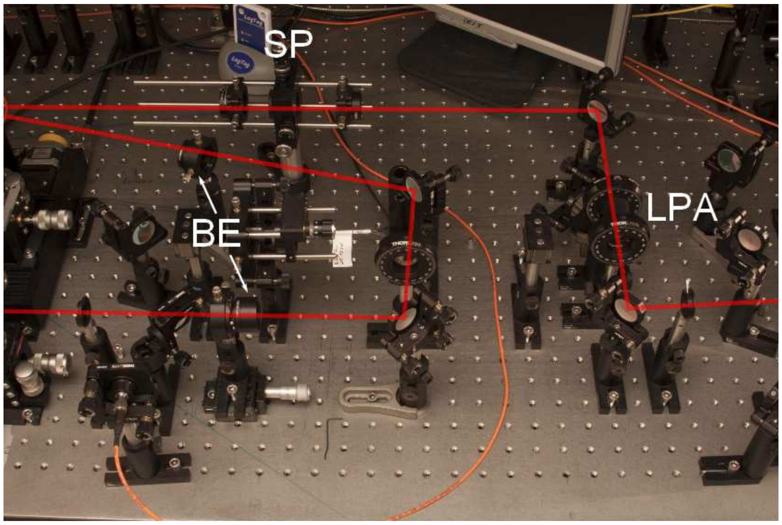

Figure 3.7: Picture of the section of the setup where the pump beam shape is optimized to increase the overlap with the Bragg mode.

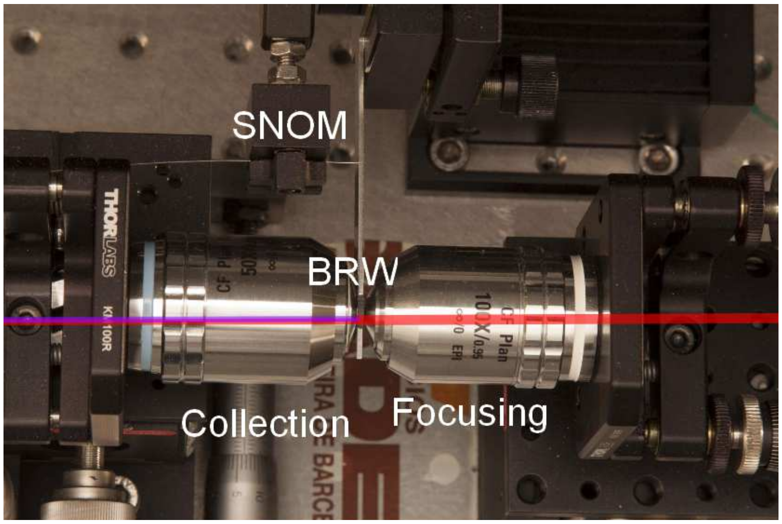

Figure 3.8: Picture of the section of the setup where the SPDC process occurs.

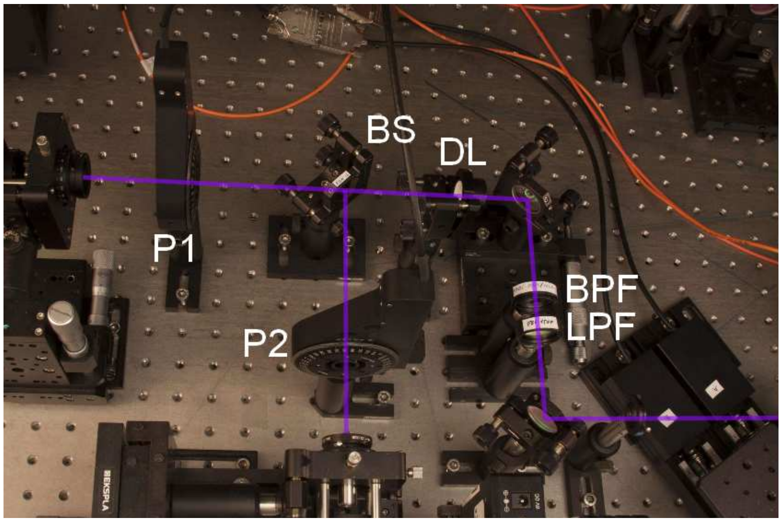

Figure 3.9: Picture of the section of the setup where the Bell inequality measurement is performed.

ity mismatch (GVM) and the GVD. In the experiment, we measured the erasure of photon distinguishability with a HOM scheme, but the difference of quartz thickness that could be obtained by tilting the plate was not enough to measure the whole HOM dip. Therefore, we decided to tilt the quartz plate until we obtained high-quality results in terms of the visibility measured.

The down-converted photons are separated into arms 1 and 2 with a 50:50 non-polarizing beam splitter (BS) in order to generate a polarization-entangled two-photon state of the form

$$\left|\Psi^{+}\right\rangle = \frac{1}{\sqrt{2}} \left\{ \left|H\right\rangle_1 \left|V\right\rangle_2 + \left|V\right\rangle_1 \left|H\right\rangle_2 \right\}, \tag{3.1}$$

where $|H\rangle$ and $|V\rangle$ denote the two possible polarizations of the photons (horizontal and vertical), propagating in arms 1 or 2. Horizontal (vertical) photons corresponds to photons propagating inside the waveguide as TE (TM) mode. We neglect cases where both photons leave the BS through the same output port, by measuring only coincidences between photons propagating in arms 1 and 2 (post-selection), which implies that 50% of the generated pairs are not considered. Finally, to measure Bell's inequality violations, the entangled photons are projected into different polarization states with linear film polarizers, and coupled into multi-mode fibres connected to InGaAs single-photon detection modules (id201, idQuantique), where optical and electronic delays are introduced to measure coincidental events with time-to-amplitude converter (TAC) electronics. The coincidence window for all measurements was set to 3 ns.

3.4 Results

In this section we will show the main results that demonstrate the generation of polarization entanglement by means of SPDC within a semiconductor BRW.

3.4.1 Coincidence fringes

To obtain a first indication that the pairs of photons propagating in arms 1 and 2 are truly entangled in the polarization degree of freedom, so that their quantum state can be written of the form given by Eq. (3.1), one detects one of the photons, i.e., the photon propagating in arm 1, after projection into a specific polarization state $|\Psi\rangle_1 = \cos\theta_1 |H\rangle_1 - \sin\theta_1 |V\rangle_1$, and measures in coincidence the remaining photon after projection into a set of polarization bases of the form $|\Psi\rangle_2 = \cos\theta_2 |V\rangle_2 + \sin\theta_2 |H\rangle_2$, with θ_2 spanning from 0 to 2π [98]. Note that the chosen polarization states mirror the experimental arrangement implemented. Ideally, the coincidence counts as a function of θ_2 should follow the form of $\cos^2(\theta_1 + \theta_2)$, which yields a visibility $V = (\text{Max} - \text{Min})/(\text{Max} + \text{Min})$ of 100%. Therefore, the highest the visibility measured, the highest the quality of the generated polarization-entangled state.

Figures 3.10(a) and (b) show the results of the measurements for two specific cases: $\theta_1 = 0°$ and $\theta_1 = 45°$. The measured visibility, subtracting the accidental coincidences, is 98% for $\theta_1 = 0°$, and 91% for $\theta_1 = 45°$. Without subtraction of accidental coincidences, the corresponding measured visibility is 80% for $\theta_1 = 0°$ and 77% for $\theta_1 = 45°$. The accidental coincidences, with respect to the total number of events counted, were measured experimentally, introducing an electronic delay in the trigger of the second detector driving it out of the detection window of the first detector. The same electronic delay had to be introduced before the TAC electronics in order to have the coincidence events from the same amount of single events, but totally uncorrelated in this case. This technique made possible to measure the correct visibility of the fringes using the maximum efficiency detector settings, in order to obtain lower standard deviation of the measurements. The optimum trigger rate for this experiment was found to be 100 KHz, measuring an average of 3550 and 6200 photon counts per second in each detector, and a maximum flux rate of coincidences of 3 pairs of photons per second. The low trigger

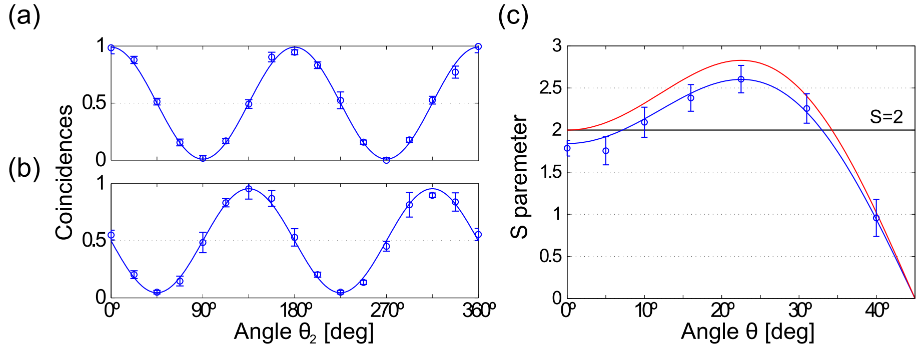

Figure 3.10: Normalized coincidence measurements as a function of the polarization state of photon 2 when photon 1 is projected into a polarization state with: (a) $\theta_1 = 0°$ and (b) $\theta_1 = 45°$. (c) Violation of the CHSH inequality. Parameter S as a function of the angle θ. The small blue circles with error bars represent the experimental data with their standard deviations. The blue solid curves in (a) and (b) are theoretical predictions assuming that the visibility is 98% in (a) and 91% in (b). The red (upper) curve in (c) is the theoretical prediction for S. The blue curve in (c) is the theoretical prediction for S, taking into account the visibility value V measured in the experiment. You can see Appendix A for an explanation and calculations of how this is done. The maximum value attained is $S = 2.61 \pm 0.16$.

rate is one of the reasons for the observation of such a low flux rate of down-converted photons observed, since it implies that the detectors are closed most of the time. The detection window for these measurements was set to 100 ns.

3.4.2 Violation of the CHSH inequality

In a CHSH inequality experiment [5], one measures photon coincidences between photon 1, after being projected into a polarization state defined by angles θ_1 or θ_1', and photon 2, after a similar polarization projection defined by angles θ_2 or θ_2'. The CHSH inequality holds if

$$S = |E(\theta_1, \theta_2) - E(\theta_1, \theta_2^{'}) + E(\theta_1^{'}, \theta_2) + E(\theta_1^{'}, \theta_2^{'})| \leq 2, \tag{3.2}$$

where

$$E(\theta_1, \theta_2) = \frac{C(\theta_1, \theta_2) + C(\theta_1^{\perp}, \theta_2^{\perp}) - C(\theta_1^{\perp}, \theta_2) - C(\theta_1, \theta_2^{\perp})}{C(\theta_1, \theta_2) + C(\theta_1^{\perp}, \theta_2^{\perp}) + C(\theta_1^{\perp}, \theta_2) + C(\theta_1, \theta_2^{\perp})}. \tag{3.3}$$

$C(\theta_1, \theta_2)$ is the number of photons detected in coincidences when its quantum state is projected into a polarization state determined by the angles θ_1 and θ_2, being $\theta_{1,2}^{\perp} = \theta_{1,2} + 90°$.

Figure 3.10(c) shows the value of the parameter S as a function of the angle θ, where $\theta \equiv \theta_2 - \theta_1 = \theta_2^{'} + \theta_1^{'} = -\theta_2 - \theta_1^{'}$, which attains the maximum possible violation, i.e., $S = 2\sqrt{2}$. For the ideal case, one would obtain $S(\theta) = 3\cos 2\theta - \cos 6\theta$, which is the red (upper) curve depicted in Fig. 3.10(c). However, if you take into account the imperfections of the optics, accidental coincidences and miss-alignments, the final values of S is decreased by an amount given by visibility value V, which is the blue (lower) curve. Why and how this is the case is explained and deduced in Appendix A. Sixteen measurements were performed for each value of the angle θ. For the maximum inequality violation ($\theta = 22.5°$), the polarizer settings were $\theta_1 = 0°$, $\theta_1^{'} = -45°$, $\theta_2 = 22.5°$ and $\theta_2' = 67.5°$. In this case, we obtained a value of the inequality of $S = 2.61 \pm 0.16$, which represents a violation by more than 3 standard deviations. This represents a stronger violation of the CHSH inequality than similar work previously reported [95] for a vertically pumped BRW structure, where the measured value was $S = 2.23 \pm 0.11$.

Regarding the measurements of the S parameter, no accidental coincidences were subtracted from the absolute measurement obtained. In order to increase the signal-to-noise ratio, the detection window in both detectors was decreased to 20% of its previous time duration (from 100 ns to 20 ns), having thus a corresponding decrease in the total number of single and coincidence counts detected. Now, the measured average flux rates are 600 and 500 photon counts per second in each detector, and a maximum value of coincidence counts of 0.3 pairs of photons per second.

To estimate the efficiency of the SPDC process, we take into account that the detection window is $\tau = 20$ ns, and the trigger rate of detection is 100 kHz. The efficiency of each single-photon detector is 25%. The pump power injected into the BRW waveguide is estimated to be around 1.3 mW. Assuming that the transmissivity of each optical system, traversed by signal/ idler photons, not including detection efficiency, is $\sim 10\%$, it results in an estimated SPDC efficiency of $\sim 10^{-10}$ in the filtering bandwidth. As can be deduced when comparing with, for instance, experimental work done in Steinlechner's PhD thesis [99], the value of the efficiency is not yet comparable with the efficiency of some of the brightest sources demonstrated of polarization entangled photons. However, there are still possible improvements of the BRW design and fabrication process in order to increase the generation efficiency. Some of them are discussed in Chapter 7.

CHAPTER

FOUR

GENERATION OF ENTANGLEMENT BETWEEN DEGREES OF FREEDOM

4.1 Introduction

One of the most relevant contribution to the discussion about entanglement, that started in 1935 between Einstein and Bohr, has been the introduction of the now well-known Bell inequality [4]. Originally, Bell’s inequalities were considered for composite systems made up of two separate subsystems, i.e., two subsystems propagating along different directions that had interacted in the past.

For instance, the two subsystems can be each one of the two photons generated by means of the nonlinear process of spontaneous parametric down-conversion (SPDC) [68]. Entanglement can reside in any of the degrees of freedom that characterize each of the photons, with being polarization and momentum the most common. In this case, one of the quantum states that allows a maximum violation of the CHSH inequality [5], Bell-like inequality described also in Chapter 3, can be written as $|\Phi\rangle = 1/\sqrt{2}\left[a^\dagger_{k_1,H} a^\dagger_{k_2,V} + a^\dagger_{k_1,V} a^\dagger_{k_2,H}\right]|\text{vac}\rangle$, where $a^\dagger_{k_i,H}$ designates the creation operator of a photon propagating along direction k_i $(i = 1, 2)$ with polarization H, similarly for $a^\dagger_{k_i,V}$, and $|\text{vac}\rangle$ is the vacuum state.

However, correlations of a nature similar to the ones existing between physically separated photons can also exist considering different degrees of freedom of a single system. Therefore, Bell's inequalities can be used as well to characterize these correlations existing between different parts of a single system. The key point to consider regarding Bell's inequalities in this scenario is the capability to perform independent measurements in any of the degrees of freedom involved. In Ref. [31], a single photon was generated in the quantum state $|\Phi\rangle = 1/\sqrt{2}\,[a^\dagger_{k_1,H} + a^\dagger_{k_2,V}]|\text{vac}\rangle$, which violates a Bell-like inequality involving two degrees of freedom (polarization and path).

Bell-like inequalities can be also used in particular cases to characterize beams containing many photons, i.e., intense beams, coherent or not. In Refs. [32, 33], the authors make use of coherent beams whose electric field reads $\mathbf{E}(\mathbf{r}) = 1/\sqrt{2}\,[\Psi_H(\mathbf{r})\,\hat{\mathbf{e}}_H + \Psi_V(\mathbf{r})\,\hat{\mathbf{e}}_V]$ and use a CHSH inequality [5] to characterize their coherence properties in one of the two degrees of freedom involved, i.e., polarization or the spatial shape. Entanglement, as the inseparability of degrees of freedom, has also been considered [36, 37] as a fundamental tool to address and shed new light on certain characteristics of classical fields, by applying analysis and techniques usually restricted to entanglement in a quantum scenario.

In this chapter we intend to move further into this analogy and show experimentally that one can generate tunable entanglement between two degrees of freedom of a single photon, going from the generation of coherent correlations to incoherent ones. For the single-photon case, the control of the degree of entanglement between degrees of freedom is fully equivalent to tuning the first-order coherence [42] of one of the degrees of freedom involved, in full analogy with the relationship existing between the degree of entanglement between separate photons and the first-order coherence of one of the photons that forms the pair.

Different types of quantum states provide different results in the measurement of the CHSH inequality. This notwithstanding, for any quantum state with any degree of first-order coherence or purity, we demonstrate that the results of a Bell's inequality measurement obtained using different degrees of freedom of a single photon, are the same as when using the properties of separate photons.

In our experiment we make use of single photons where the two degrees of freedom involved are the polarization (horizontal and vertical linear polarizations) and spatial modes (two spatial modes with orbital angular momentum index $m = \pm 1$). The orbital angular momentum (OAM) states allow for a relatively simple experimental generation, filtering, detection, and control [70]. These states are characterized by the index m, which can take any integer number, and determines the azimuthal phase dependence of the mode, which is of the form $\sim \exp(im\varphi)$. Each mode carries an OAM of $m\hbar$ per photon. The feasibility to generate entangled states in the laboratory using polarization and spatial modes with OAM is greatly facilitated by the use of the so-called q-plates [100]: Liquid crystal devices which couple together polarization and orbital angular momentum and allow the generation of states that have been recently exploited in fundamental quantum mechanics [101,102], quantum communications [103], and metrology [104]. In Ref. [72], Nagali et al. generated a single-photon quantum state with the OAM and polarization degrees of freedom with high purity. Karimi et al. [75] used this same state to demonstrate the violation of the CHSH inequality.

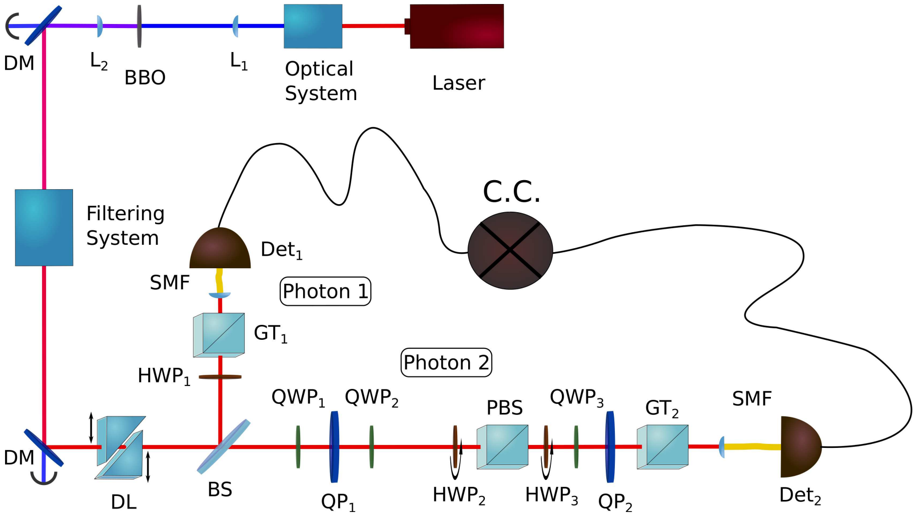

Figure 4.1: Experimental setup scheme. Laser: Mira 900 (Coherent). Optical system: second harmonic generation (Inspire Blue, Radiantis), cylindrical lenses (CL), spatial filter (SP), linear attenuator (LA), dichroic mirrors (DM), and short pass filter (SPF). $L_{1\&2}$: Fourier lenses. BBO: nonlinear crystal. Filtering system: long-pass and band-pass filters. DL: delay line. BS: beam splitter (50:50). $HWP_{1,2\&3}$: half-wave plates. PBS: polarization beam splitter. $GT_{1\&2}$: Glan-Thompson polarizers. $QWP_{1,2\&3}$: quarter-wave plates. $QP_{1\&2}$: q-plates. $Det_{1\&2}$: single-photon counting modules. C.C.: coincidence-counting electronics.

4.2 Experimental setup

The experimental setup used in our experiment is shown in Fig. 4.1. Paired photons are generated in a 2-mm-long β-barium borate (BBO) nonlinear crystal by means of SPDC. We choose a type-II source, where the photons generated have orthogonal (horizontal and vertical) polarizations in order to generate a polarization-entangled photon pair by post-selection with a beam splitter and a coincidence detection.

The pumping laser is a Mira 900 (Coherent) working in the picosecond regime and tuned to a central wavelength of 810 nm. In order to obtain the down-converted photons at 810 nm, light from Mira is frequency doubled in a second-harmonic setup (Inspire Blue, Radiantis). The output light at 405 nm traverses an optical system with five dichroic mirrors and a short-pass filter to filter out the remaining 810 nm light. A spatial filter tailors the spatial shape of the pump beam to obtain the sought-after Gaussian beam profile. We use a 750-mm focal distance lens to obtain a pump beam with 400-μm beam waist that is focused in the middle of the nonlinear crystal. A smaller beam waist would increase efficiency of the SPDC process; however, the spatial walkoff in the BBO crystal impedes tighter focusing, because it would also introduce harmful spatial distinguishability between the generated photons. The down-converted photons are collected with a 400-mm focal distance lens.

Another filtering system, formed by two dichroic mirrors, a long-pass filter, and a band-pass filter, removes the residual pump light at 405 nm. Different group velocities result in slightly different spectra of the orthogonal polarizations, thus mixing the polarization and frequency properties of the photons. The use of a filter with 3-nm full-width-half-maximum bandwidth centred at 810 nm helps reducing the spectral distinguishability between the photons.

After the beam splitter, the quantum state of the two photons, considering only the cases when the paired photons are detected in coincidence (post-selection), can be generally written as

$$\begin{aligned}\rho &= \epsilon|\Psi\rangle\langle\Psi| \\ &+\frac{1-\epsilon}{2}\times\left\{|H\rangle_1|V\rangle_2\langle H|_1\langle V|_2+|V\rangle_1|H\rangle_2\langle V|_1\langle H|_2\right\}, \qquad (4.1)\end{aligned}$$

where indexes 1 and 2 refers to paths 1 and 2 after the beam splitter, $|\Psi\rangle = 1/\sqrt{2}\ \{|H\rangle_1|V\rangle_2 + |V\rangle_1|H\rangle_2\}$, and ϵ depends on the delay (τ) between the two orthogonal photons generated. The form of the state given by Eq. (4.1) is due to the correlation exiting between the polarization of the photon generated and its group velocity, since the nonlinear crystal used (BBO) is a birefringent crystal. In particular, the group velocity of photons at 810 nm with horizontal polarization (ordinary wave) is $v_g^o = 1.7816 \times 10^8$ m/s, while the group velocity of photons with vertical polarization (extraordinary wave) is $v_g^e = 1.8439 \times 10^8$ m/s, which produces a group velocity mismatch (GVM) of $D_{BBO} = 1/v_g^o - 1/v_g^e = 189.6$ fs/mm. This distinguishability of photons by its group velocity cause the mixed character of the quantum state in polarization given by Eq. (4.1).

A delay line, formed by quartz prisms, can be used to tune its value. If photons could be distinguished by their time of arrival at the detectors, then $\epsilon = 0$ and the purity of the quantum state that describes the two photons generated is minimal ($\mathcal{P} = 1/2$). The purity of the quantum state can be increased by adding or removing the length of quartz that the photons traverse along its optical path [69], which is necessary to remove all distinguishing information coming from the temporal-frequency degree of freedom. The group velocity of ordinary waves in quartz is $v_g^o = 1.9305 \times 10^8$ m/s, while the group velocity of extraordinary waves is $v_g^e = 1.9187 \times 10^8$, which produces a GVM of $D_{quartz} = -31.8$ fs/mm. For a specific arrangement of the quartz prisms, that we define as $\tau = 0$, we can have $\epsilon = 1$. For the $L = 2$ mm long BBO crystal of our experiment, with group velocity mismatch of $D_{BBO} = 189.6$ fs/mm, this requires [98] compensating with the tunable delay line $D_{BBO} L/2 = 189.6/2$ fs/mm $\times$ 2 mm =189.6 fs.

To entangle the polarization and the orbital angular momentum (OAM) degrees of freedom in a single photon, the photon reflected from the beam splitter (photon 1) is projected into the linear diagonal polarization state: $1/\sqrt{2}\ \{|H\rangle \pm |V\rangle\}$, with a half-wave plate (HWP$_1$) and a Glan-Thompson polarizer (GT$_1$), coupled into a single mode fibre, to remove the remaining spatial distinguishability introduced by the presence of spatial walkoff in the BBO crystal, and detect it in coincidences (coincidence time window of 12.5 ns). The transmitted photon (photon 2) traverses a quarter-wave plate (QWP$_1$) to rotate its polarization from horizontal and vertical to circular right (**R**) and circular left (**L**), a q-plate (QP_1) correlates polarization with OAM, and another quarter-wave plate (QWP_2) transforms the polarization back from circular right and circular left to horizontal and vertical. In summary,

$$\begin{aligned}|\mathbf{H}\rangle \Longrightarrow |\mathbf{R}\rangle \Longrightarrow |\mathbf{L}, \mathbf{m} = -\mathbf{1}\rangle \Longrightarrow |\mathbf{H}, \mathbf{m} = -\mathbf{1}\rangle,\\ |\mathbf{V}\rangle \Longrightarrow |\mathbf{L}\rangle \Longrightarrow |\mathbf{R}, \mathbf{m} = +\mathbf{1}\rangle \Longrightarrow |\mathbf{V}, \mathbf{m} = +\mathbf{1}\rangle.\end{aligned} \tag{4.2}$$

After the second quarter-wave plate, the quantum state of photon 2, after projection and detection of photon 1, is written as

$$\begin{aligned}&\rho = \epsilon|\Psi^{\pm}\rangle\langle\Psi^{\pm}|\\ &+\frac{1-\epsilon}{2}\left\{|H, m = -1\rangle\langle H, m = -1| + |V, m = +1\rangle\langle V, m = +1|\right\},\end{aligned} \tag{4.3}$$

where

$$\left|\Psi^{\pm}\right\rangle = \frac{1}{\sqrt{2}}\left\{|H, m = -1\rangle \pm |V, m = +1\rangle\right\}. \tag{4.4}$$

The purity of the state is $\mathcal{P} = (1+\epsilon^2)/2$. If one would apply the concept of concurrence [13] to this single-photon state, considering as the two subsystems the polarization and OAM degrees of freedom of the photon, one would obtain $C = \epsilon$.

The measurement stage consist of projecting the quantum state generated into specific polarization and OAM states in two steps. First, the state of polarization is projected into the desired state with a half-wave plate (HWP_2) and a polarizing beam splitter (PBS). The OAM can be projected into any state using several polarization optic elements, before and after a second q-plate (QP_2) [72]. More specifically, the OAM state information is transferred into a polarization state with a half-wave plate (HWP_3) and a quarter-wave plate (QWP_3) located before the q-plate, to transform horizontal-vertical polarizations to right-left polarizations base, and another Glan-Thompson polarizer (GT_2) located after . Finally, the photon is spatially filtered by coupling it to a single-mode fibre and detecting it in coincidence with the other photon (photon 1).

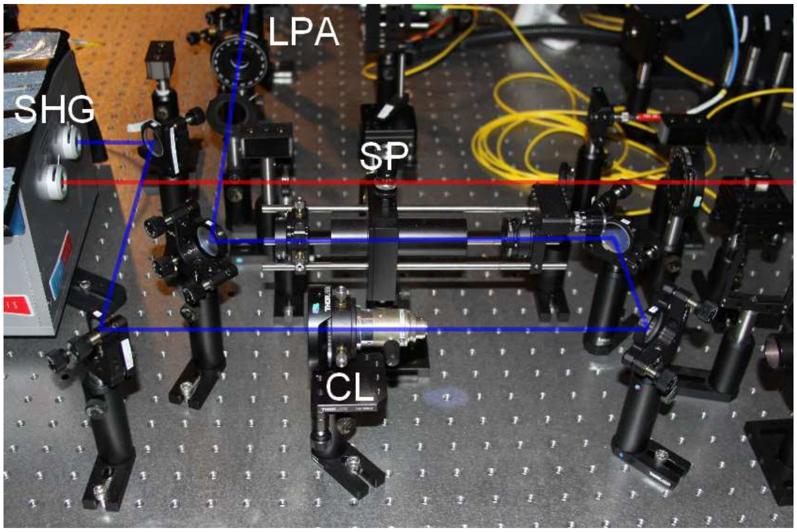

Figure 4.2: Picture of the section of the setup where the pumping beam is frequency doubled and spatially optimized.

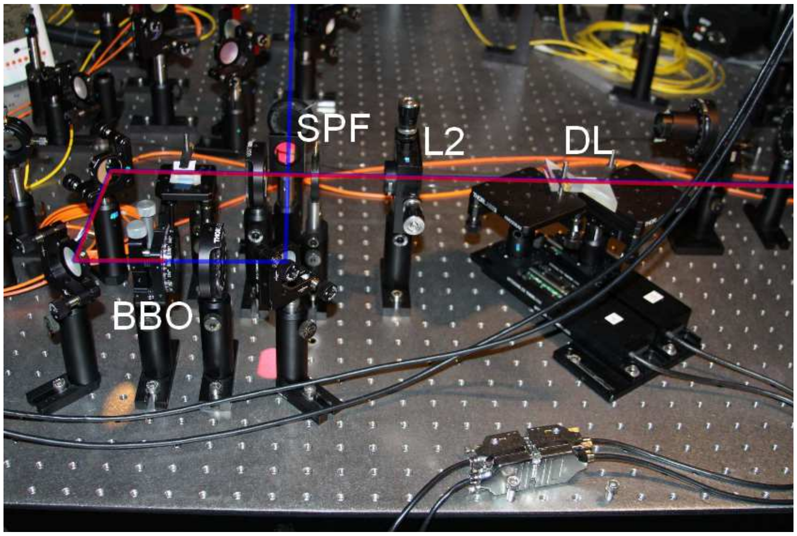

Figure 4.3: Picture of the section of the setup where the SPDC process and temporal compensation take place.

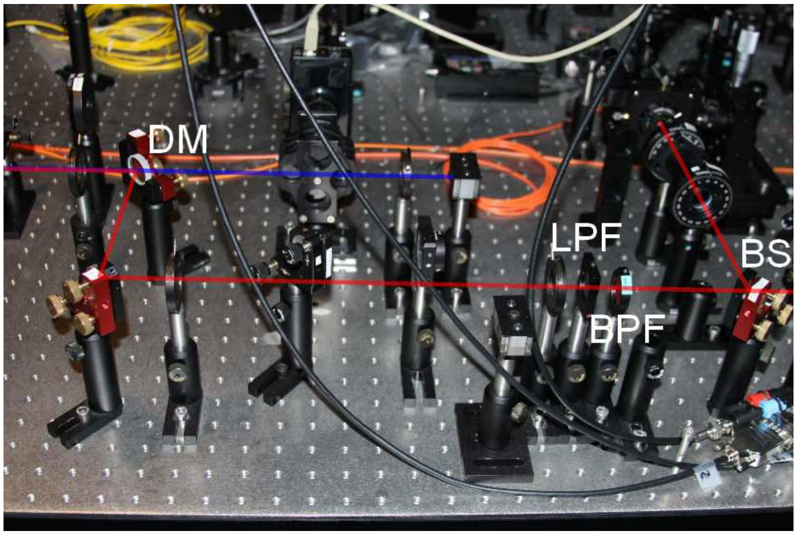

Figure 4.4: Picture of the section of the setup where the SPDC photon pairs are separated from the residual pump and spectrally filtered.

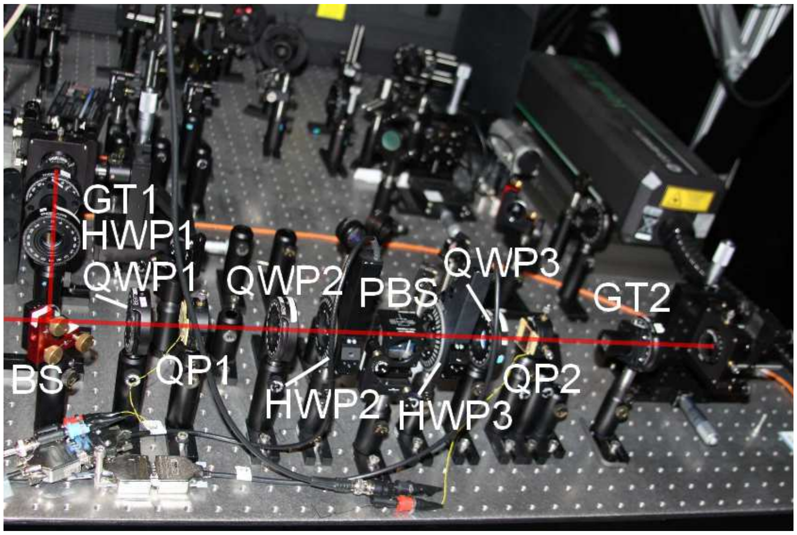

Figure 4.5: Picture of the section of the setup where the entanglement after the first QP is achieved and the Bell inequality measurement is performed.

In Figs. 4.2 to 4.5 are shown some pictures taken from the different parts of the setup used to measure the experimental results shown in the next section.

4.3 Results

In order to be able to relate the value of ϵ in Eq. (4.3) to the delay introduced by the delay line, and determine the value of the delay which makes the quantum state pure ($\epsilon = 1$), we construct a Hong-Ou-Mandel interferometer (HOM). If we choose the temporal delay introduced by the delay line so that coincidences are close to zero, the state given by Eq. (4.3) is pure ($\epsilon = 1$) and corresponds to a Bell state. We choose to generate the quantum state $|\Psi^-\rangle$ to obtain the HOM dip. Figure 4.6(a) shows the coincidence photons measured in detectors 1 and 2, and Fig. 4.6(b) shows the single photons detected in each detector. Figure 4.6(c) shows coincidence detections renormalized using the single measurements from detector 1. The oscillations in detector 1 are due to imperfections in the translation stage of the delay line (DL), causing deviations in the photon trajectories. Thus the single detections of detector 1 are clearly affected by these corresponding variations in the coupling efficiency. We should notice that all the results presented in this chapter are shown with no subtraction of the accidental coincidences (~ 4 pairs in 10 s).

When we change, with HWP$_1$, the projection of photon 1 from the state $1/\sqrt{2}\,[|H\rangle + |V\rangle]$ to $1/\sqrt{2}\,[|H\rangle - |V\rangle]$, we change the sign of the corresponding Bell state, from $|\Psi^-\rangle$ to $|\Psi^+\rangle$. By modifying the transformation of photon 2 from $L/R \Longrightarrow H/V$ to $L/R \Longrightarrow V/H$ with QWP$_2$, we can go from the generation of $|\Psi^\pm\rangle$ to $|\Phi^\pm\rangle$, where $\Phi^\pm$ can be written as

$$\left|\Phi^\pm\right\rangle = \frac{1}{\sqrt{2}}\left(|H, m = +1\rangle \pm |V, m = -1\rangle\right). \tag{4.5}$$

With this procedure we are able to create the four Bell states.

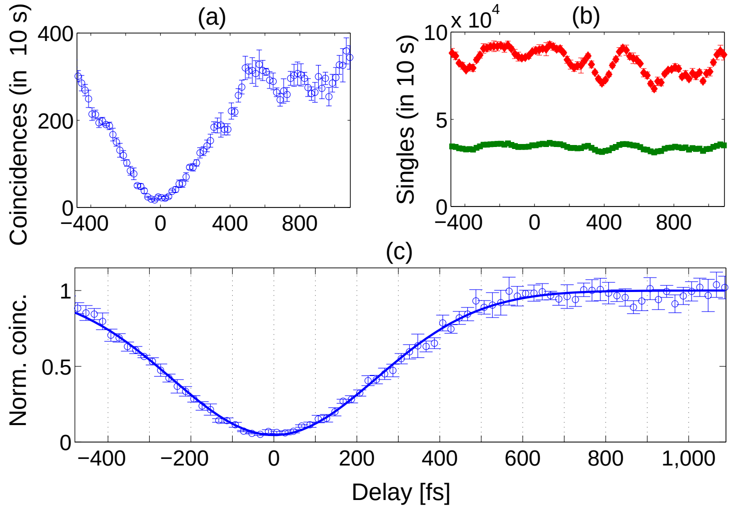

Figure 4.6: Coincidence and singles detections as a function of the temporal delay τ in a Hong-Ou-Mandel (HOM) interferometer. The raw data of the coincidences measured in 10 s are plotted in panel (a), and the singles detected for each detector are shown in panel (b). Closed diamonds (upper curve) correspond to singles detected with detector 1, and closed squares (lower curve) correspond to measurements in detector 2. The compensated and normalized number of coincidences is plotted in panel (c), using the coincidence data of panel (a) and the singles detected with detector 1 shown in panel (b).

Figure 4.7 shows the coincidences measured for each of the four Bell states. Photon 2 is projected first into the polarization state $\sim \cos\beta_1 |H\rangle + \sin\beta_1 |V\rangle$, with $\beta_1 = 0°$, $45°$, and after that a second projection is performed into a set of OAM states of the form $\sim \cos\beta_2 |+1\rangle + \sin\beta_2 |-1\rangle$, with β_2 spanning from 0 to 2π. Ideally, for the state $|\Psi^-\rangle$, coincidence counts as a function of β_2 follow the form of $\sin^2(\beta_1 - \beta_2)$, which yields a visibility [98] $V = (\text{Max} - \text{Min})/(\text{Max} + \text{Min})$ of 100%. Therefore, as the visibility measured increased, so did the quality of the generated entangled state.

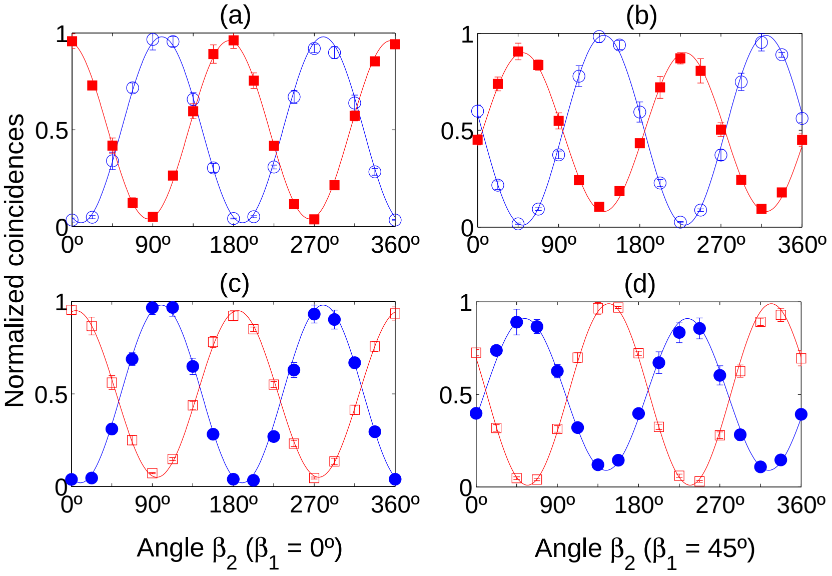

Figure 4.7: Normalized value of the coincidences as a function of the projection angle β_2. Panels (a) and (c): the angle of HWP$_2$ is set to $\beta_1 = 0°$; panels (b) and (d): the angle is set to $\beta_1 = 45°$. Curves corresponding to experimental values are shown with error bars. Solid lines are theoretical predictions. Open circles, $|\Psi^-\rangle$; closed circles, $|\Psi^+\rangle$; open squares, $|\Phi^-\rangle$; and closed squares, $|\Phi^+\rangle$.

The small phase shifts observed in the curves are due to some misalignment still present between the position of the centres of the vortex of the two OAM modes, $m = +1$ and $m = -1$, when going through the second q-plate (QP$_2$).

Measurements of the CHSH inequality [5] requires choosing two polarization states and two OAM states where the state of photon 2, given by Eq. (4.3), is projected. When considering any possible state projection, following Ref. [105], one finds that the maximum violation of the CHSH inequality for this state is

$$S_{max} = 2\sqrt{1+\epsilon^2}. \tag{4.6}$$

For $\epsilon = 1$ we reach the Tsirelson bound. We will restrict the discussion here to only projections into states of the form

$$\begin{aligned} |\mathbf{a}_i\rangle &= \frac{1}{\sqrt{2}}\left(\cos a_i\,|H\rangle + \sin a_i\,|V\rangle\right), \\ |\mathbf{b}_i\rangle &= \frac{1}{\sqrt{2}}\left(\cos b_i\,|m=+1\rangle + \sin b_i\,|m=-1\rangle\right), \end{aligned} \tag{4.7}$$

where states $\mathbf{a}_i$ $(i = 1, 2)$ refers to linear polarization states and $\mathbf{b}_i$ $(i = 1, 2)$ refer to OAM states which are linear combinations of modes $m = +1$ and $m = -1$. By proper combinations of all the polarization optical elements of the setup (half-wave and quarter-wave plates), one can project the photon into any combination $(\mathbf{a}_i, \mathbf{b}_i)$ as required.

For the single-photon case, restricting our attention to state projections of the form given in Eq. (4.7), the CHSH inequality can be written as

$$S = |E(a_1, b_1) - E(a_1, b_2) + E(a_2, b_1) + E(a_2 + b_2)| \leq 2, \tag{4.8}$$

where

$$E(a_i, b_i) = \frac{C(a_i, b_i) + C(a_i^\perp, b_i^\perp) - C(a_i, b_i^\perp) - C(a_i^\perp, b_i)}{C(a_i, b_i) + C(a_i^\perp, b_i^\perp) + C(a_i, b_i^\perp) + C(a_i^\perp, b_i)}. \tag{4.9}$$

Similarly as in Chapter 3, $C(a_i, b_i)$ is the number of photons detected in coincidences when its quantum state is projected into a polarization state determined by the angle a_i, and an OAM state determined by the angle b_i. All other cases follow similarly, taking into account that $a_i^\perp = a_i + 90°$, and $b_i^\perp = b_i + 90°$. One can find that for the state given by Eq. (4.3),

$$E(a_i, b_i) = \cos 2a_i \cos 2b_i + \epsilon \sin 2a_i \sin 2b_i. \tag{4.10}$$

Figure 4.8 shows the value of S measured when we go from a pure to a mixed state, i.e., for different values of ϵ from 0 to 1. It shows the value of S as a function of the angle θ, where $\theta \equiv b_1 - a_1 = b_2 + a_2 =$

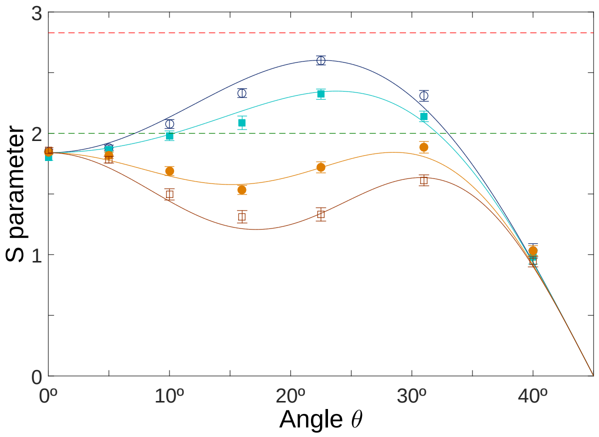

Figure 4.8: Value of the parameter S in a CHSH inequality as a function of the angle $\theta = b_1 - a_1$. The coloured symbols with error bars represent the experimental data with their standard deviations. The solid coloured curves are the theoretical predictions assuming different values of ϵ and a visibility of $V = 0.92$ (see Appendix A for an explanation). Open circles, $\epsilon = 1$; closed squares, $\epsilon = 0.8$; closed circles, $\epsilon = 0.32$; and open squares, $\epsilon = 0.03$. The values of ϵ correspond to delays of 0 fs ($\epsilon = 1$), 200 fs ($\epsilon = 0.8$), 400 fs ($\epsilon = 0.32$), and 600 fs ($\epsilon = 0.03$), as depicted in the HOM dip of Fig. 4.6. The dashed red line (upper) corresponds to the Tsirelson bound, and the dashed green line (lower) is the CHSH inequality limit.

$-b_1 - a_2$. For the case of a pure state, one would obtain $S(\theta) = 3\cos 2\theta - \cos 6\theta$. The experimental values measured decrease from the theoretical (ideal) expected values due to the existence of accidental coincidences or the inevitable misalignment of optical elements, by a factor V, the visibility measured in Fig. 4.7. In Appendix A we explain how this relationship is obtained and how is related to the coincidence fringes measurements. In our case, the maximum CHSH inequality value measured is $S(\theta = 22.5°) = 2.601 \pm 0.037$ and the visibility is $V = 0.92$.

Figure 4.8 shows that there is a complete analogy between a Bell-

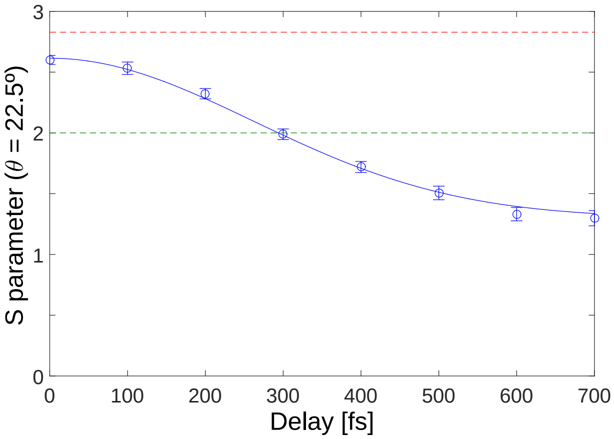

Figure 4.9: Value of the CHSH inequality for $\theta = 22.5°$ as a function of the temporal delay, as depicted in Fig. 4.6. The solid (blue) curve is the theoretical prediction assuming a visibility factor of $V = 0.92$. The dashed red line (upper) corresponds to the Tsirelson bound ($S_{max} = 2\sqrt{2}$), and the dashed green line (lower) is the CHSH inequality limit ($S = 2$).

like inequality involving the same degree of freedom of two separate photons [7,105] and that involving two distinct degrees of freedom of the same single photon, independent of the purity (or first-order coherence) of the quantum state. Figure 4.9 shows the CHSH violation measured for $\theta = 22.5°$, which gives the maximum violation for a pure state. When the delay increases or decreases from τ_0, the state becomes increasingly mixed and entanglement disappears. Figures 4.8 and 4.9 are very similar to what would have been obtained for the case of two separate correlated photons, even though here the measurement corresponds to measuring correlations between properties in different degrees of freedom of a single photon. The similarities in form between the quantum states with different numbers of photons are why we obtain similar results, as it has been pointed out in several theoretical papers [36,37,106], experiments [31,32], as and in Chapter 2.

CHAPTER
FIVE

REVEALING HIDDEN COHERENCE IN ENTANGLED SYSTEMS

5.1 Introduction

Coherence is one of the most important concepts needed to describe the characteristics of a stream of photons [41, 61]. In particular, it allows to characterize the interference capability of interacting fields. However its use is far more general as it plays a striking role in a whole range of physical, chemical, and biological phenomena [107]. Measures of coherence can be implemented using classical and quantum ideas, which lead to the question of in which sense quantum coherence might deviate from classical coherence phenomena [57], and to the evaluation of measures of coherence [65, 108, 109].

Coherence measures commonly used consider a physical system as a whole, omitting its structure. However, the knowledge of the internal distribution of coherence between subsystems and their correlations becomes necessary for predicting the evolution (migration) of coherence from one part of the system to another. The evolution of how coherence manifest in a twin beam from the near field into the far field represents a typical example occurring in nature [110]. The creation of entangled states by merging the initially separable incoherent and coherent states serves as another example [109]. Or, in quantum computing the controlled-NOT gate entangles (disentangles) two-qubit states [111, 112], at the expense (in favour) of coherence.

Many quantum metrology and communication applications benefit from the correlations of entangled photon pairs that originate in the nonlinear process of spontaneous parametric down-conversion process [113–115]. Even separable states of photon pairs, i.e., states with suppressed correlations, are very useful, e.g., in heralded single photon sources [116, 117]. For all of these, and many other examples, understanding the features of the common evolution of coherence and correlations is crucial.

The Clauser-Horne-Shimony-Holt (CHSH) Bell-like inequality [5, 105] has been usually considered to quantify nonclassical correlations present between physically separated photons that are entangled and so they can violate the bound set by the inequality. However, correlations of a similar nature can also exist when considering different degrees of freedom of a single system [31, 73]. The CHSH inequality can also be violated when considering intrabeam correlations between different degrees of freedom of intense beams, coherent or not [32]. This, sometimes referred to as nonquantum entanglement, or inseparability of degrees of freedom, has been considered [36, 37] as a tool to shed new light into certain characteristics of classical fields, by applying techniques usually restricted to a quantum scenario.

When the violation of the CHSH inequality between subsystems and the degree of first-order coherence, which characterizes the internal coherence of a physical subsystem [41], are combined together, it is possible to define a measure that encompasses all coherences and correlations in the system. This measure has been experimentally examined by Kagalwala et al. [33]. One fundamental problem of their formulation is that it varies under global unitary transformations. This means that, from this point of view, the amount of coherence in the system can be changed.

This behaviour has several general consequences for any partially coherent (mixed) state. First, the main point is that the coherence of each subsystem can be increased by means of a suitable unitary transformation affecting the whole system. So the hidden coherence stored in the correlations between two subsystems is made available. Second, for pure states, the roles of the degree of entanglement between subsystems, quantified by the concurrence [13, 63], and the maximum violation of the CHSH inequality ($B_{\max}$) [105] are interchangeable. However, this is not true for mixed states, where the maximal violation can take place for states that are not maximally entangled [118]. This raises the question of what is the appropriate measure to quantify hidden coherence unveiled by global unitary transformations: the degree of entanglement (concurrence) or $B_{\max}$.

In this chapter, we solve these two puzzles. First, given a generally mixed state, or equivalently a partially coherent light beam, we determine what is the maximum and minimum first-order coherence the subsystems can show under global unitary transformations. This will reveal how much hidden coherence is present in the correlations between subsystems. Second, we will determine if these maximal and minimal coherences are related to states with the maximal (minimal) degree of entanglement, or maximal or minimal violation of the CHSH inequality. This will solve the question of which of the two measures is the appropriate one to quantify hidden coherence. Our main results are expressed in two theorems valid for any mixed two-qubit quantum state, and their implication is illustrated by applying the theorems to four well-known classes of quantum states.

We restrict our attention to coherence manipulations by a general global unitary transformation. Experimentally, they can be implemented by various logical gates [115, 119, 120]. The coherence limits can be also viewed as the maximal coherence that a logical gate can provide for a given state, which is related to the entanglement power of a unitary operation [121].

5.2 General considerations

Let us consider a 2×2 dimensional quantum state, $\hat{\rho}$, composed of subsystems A and B. The state $\hat{\rho}$ can be generally written (spectral decomposition) as $\hat{\rho} = V\hat{E}V^{\dagger}$ [115], where $\hat{E}$ is a diagonal matrix with eigenvalues that satisfy $\sum_i \lambda_i = 1$ and $\lambda_1 \geq \lambda_2 \geq \lambda_3 \geq \lambda_4$. The matrix V contains the corresponding eigenvectors. Each subsystem is characterized by the corresponding density matrix, $\hat{\rho}_A$ and $\hat{\rho}_B$. The degree of first-order coherence of each subsystem is given $D_{A,B} = \sqrt{2\mathrm{tr}[\hat{\rho}_{A,B}^2] - 1}$ [61]. We introduce here a measure of coherence for both subsystems when they are considered independently $D^2 = (D_A^2 + D_B^2)/2$. When both subsystems are coherent, one has $D = 1$, while only if both subsystems show no coherence, $D = 0$.

Minimum first-order coherence.–There exists a unitary transformation U that when applied to $\hat{\rho}$ generates a new state $\hat{\rho}' = U\hat{\rho}U^{\dagger}$, so that the coherence D vanishes and the violation of the CHSH is maximized with value [105, 122]

$$B_{\max} = 2\sqrt{2}\sqrt{(\lambda_1 - \lambda_4)^2 + (\lambda_2 - \lambda_3)^2}. \tag{5.1}$$

The unitary transformation has the form $U = MV^{\dagger}$, where

$$M = \frac{1}{\sqrt{2}} \begin{pmatrix} 1 & 1 & 0 & 0 \\ 0 & 0 & 1 & 1 \\ 0 & 0 & 1 & -1 \\ 1 & -1 & 0 & 0 \end{pmatrix}. \tag{5.2}$$

It is straightforward to show (see Appendix B) that after the transformation $MV^{\dagger}$, $D_A = D_B = 0$, therefore $D = D_{\min} = 0$. One can always achieve no coherence for both subsystems. Therefore, the state with minimal coherence is the state that provides maximal violation of the CHSH inequality and it corresponds to the so-called Bell diagonal state [122].

The degree of entanglement (concurrence) of Bell diagonal states is $C_{BD} = \max\{0, 2\lambda_1 - 1\}$ [122]. The maximum concurrence that can be achieved by a unitary operation applied on $\hat{\rho}$ is $C_{\max} = \max\left\{0, \lambda_1 - \lambda_3 - 2\sqrt{\lambda_2\lambda_4}\right\}$ [123]. As we will see in example I, $C_{BD} \leq C_{\max}$ can happen for mixed states, which highlights the preference for using $B_{\max}$ over the concurrence for quantifying the coherence available for each subsystem.

Maximum first-order coherence.–There exists a unitary transformation U that when applied to an arbitrary state $\hat{\rho}$ generates a new state $\hat{\rho}' = U\hat{\rho}U^{\dagger}$ that maximizes the coherence D with value

$$D_{\max}^2 = (\lambda_1 - \lambda_4)^2 + (\lambda_2 - \lambda_3)^2, \tag{5.3}$$

and yields a violation of CHSH that is minimal, with value

$$B_{\max} = 2\left|\lambda_1 - \lambda_2 - \lambda_3 + \lambda_4\right|. \tag{5.4}$$

The unitary transformation U has the form $U = V^{\dagger}$.

The resulting state is a diagonal separable state, as it is shown in the Appendix B.

$D_{\max}$ can be called the degree of available coherence, since it represents the maximum first-order coherence that can be unveiled under a global unitary transformation. As we will show in example I below, correlations can be a source of coherence for a subsystem even when the CHSH inequality is not violated, i.e., $B_{\max} \leq 2$, and therefore the state is not entangled. Importantly, $D_{\max}$ is associated to a state with the minimum violation of the CHSH inequality, highlighting again the outstanding role of $B_{\max}$ over concurrence when considering the maximum and minimum values of the degree of coherence available.

We will now consider four examples where we apply the results mentioned above.

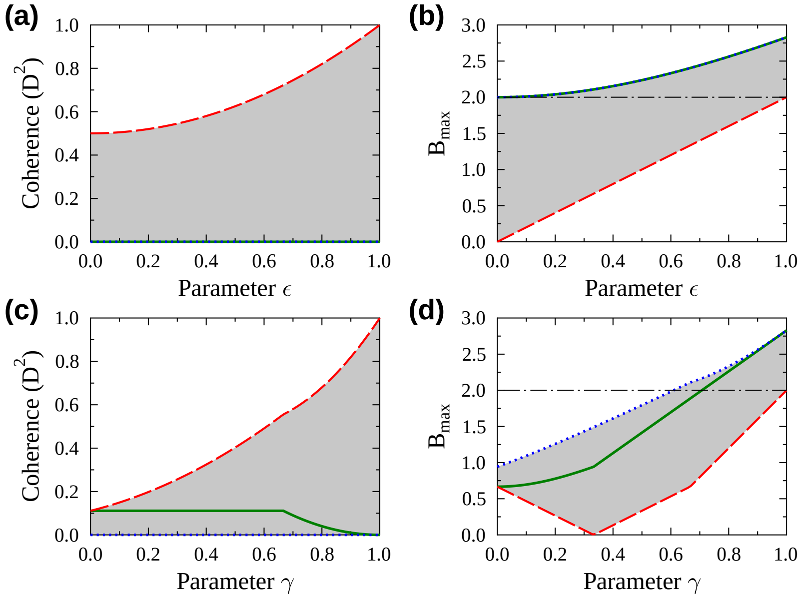

Figure 5.1: Coherence (D^2) and maximal violation of the CHSH inequality (B_{max}) for (a) and (b): example I ($\hat{\rho}_{\text{MNMS}}$), and (c) and (d): example II ($\hat{\rho}_{\text{MEMS}}$). Green lines depict the values of the original state, prior to any unitary transformation. The maximal coherence and minimal violation of the CHSH inequality are marked by dashed-red lines, and the minimal coherence and maximal violation of the CHSH inequality are marked by dotted-blue lines. The black dashed-dotted line represents the classical correlation limit $B_{\text{max}} = 2$. Grey areas correspond to all admissible values achievable by all unitary operations.

5.3 Examples

Example I: Maximally nonlocal mixed state (MNMS).– In a nonlinear process designed to generate entanglement in polarization [68,98], the state generated at the output of the nonlinear crystal can be generally written in the computational basis $\{|00\rangle, |01\rangle, |10\rangle, |11\rangle\}$ as [118,124]

$$\hat{\rho}_{\mathrm{MNMS}} = \begin{pmatrix} 1/2 & 0 & 0 & \epsilon/2 \\ 0 & 0 & 0 & 0 \\ 0 & 0 & 0 & 0 \\ \epsilon/2 & 0 & 0 & 1/2 \end{pmatrix} \quad \text{where } \epsilon \in \langle 0, 1\rangle. \tag{5.5}$$

The purity of the state is $\mathcal{P} = \mathrm{tr}[\hat{\rho}^2_{\mathrm{MNMS}}] = (1+\epsilon^2)/2$. The spectral representation of this state writes $\hat{\rho}_{\mathrm{MNMS}} = 1/2\,(1+\epsilon)|\Phi^+\rangle\langle\Phi^+| + 1/2\,(1-\epsilon)|\Phi^-\rangle\langle\Phi^-|$ This state is a Bell diagonal state, so it produces a maximal violation of the CHSH inequality. For each value of ϵ, the state $\hat{\rho}_{\mathrm{MNMS}}$ can be transformed using unitary operations to a new state $\hat{\rho}'_{\mathrm{MNMS}}$ with new values of D^2 [see Fig. 5.1(a)] and $B_{\max}$ [see Fig. 5.1(b)]. The grey areas in the figures show all possible values of D^2 and $B_{\max}$. In all cases presented here, and shown in Figs. 5.1 and 5.2, we performed extensive numerical simulations [125] generating 10^6 randomly generated unitary operations for each value of parameters, to check all of our predictions.

All of these values lie in intervals limited by states with minimal and maximal coherence. The state already yields minimal coherence ($D_A = D_B = 0$) and maximal violation of the CHSH inequality, as given by Eq. (5.1) [dotted-blue lines in Figs. 5.1(a) and 5.1(b)]

$$D_A = D_B = 0, \qquad B_{\max} = 2\sqrt{1+\epsilon^2}. \tag{5.6}$$

The case of maximal coherence and minimal violation of the CHSH inequality is given by Eqs. (5.3) and (5.4) [dashed-red lines in Figs. 5.1(a) and 5.1(b)]

$$D^2_{\max} = \frac{1+\epsilon^2}{2}, \qquad B_{\max} = 2|\epsilon|. \tag{5.7}$$

The degree of entanglement of the quantum state with minimum first-order coherence ($D_A = D_B = 0$), which corresponds to the maximal violation of the CHSH inequality, is $C_{BD} = \epsilon$. However, the maximum entanglement that can be achieved with a unitary operation is $C_{\max} = (1+\epsilon)/2$. Therefore $C_{BD} < C_{\max}$. This shows the relevant role $B_{\max}$ over the concurrence. The state which achieves minimal first-order coherence for a subsystem is also the state that maximally violates the CHSH inequality, but not the state that achieves maximum entanglement.

*Example II: Maximally entangled mixed state (MEMS)–*This state is defined as [126, 127]

$$\hat{\rho}_{MEMS} = \begin{cases} \begin{pmatrix} 1/3 & 0 & 0 & \gamma/2 \\ 0 & 1/3 & 0 & 0 \\ 0 & 0 & 0 & 0 \\ \gamma/2 & 0 & 0 & 1/3 \end{pmatrix} & \text{for } 0 \leq \gamma \leq \frac{2}{3} \\ \\ \begin{pmatrix} \gamma/2 & 0 & 0 & \gamma/2 \\ 0 & 1-\gamma & 0 & 0 \\ 0 & 0 & 0 & 0 \\ \gamma/2 & 0 & 0 & \gamma/2 \end{pmatrix} & \text{for } \frac{2}{3} \leq \gamma \leq 1 \end{cases} . \tag{5.8}$$

It maximizes the value of the concurrence for a given value of the purity. We have chosen the phases to be zero for the sake of simplicity. The purity is equal to $\mathcal{P} = \frac{1}{3} + \frac{\gamma^2}{2}$ for $0 \leq \gamma \leq \frac{2}{3}$ and $\mathcal{P} = \gamma^2 + (1-\gamma)^2$ for $\frac{2}{3} \leq \gamma \leq 1$. When the state is transformed to the new state using unitary operations [see Figs. 5.1(c) and 5.1(d)], we find that for $0 \leq \gamma \leq \frac{2}{3}$ the minimal coherence and maximal violation of the CHSH are [dotted-blue lines in Figs. 5.1(c) and 5.1(d)]

$$D_A = D_B = 0, \quad B_{\max} = 2\sqrt{2}\sqrt{\frac{\gamma^2}{4} + \left(\frac{1}{3} + \frac{\gamma}{2}\right)^2}, \tag{5.9}$$

and the maximal coherence and minimal violation of the CHSH are [dashed-red lines in Figs. 5.1(c) and 5.1(d)]

$$D^2_{\max} = \frac{\gamma^2}{4} + \left(\frac{1}{3} + \frac{\gamma}{2}\right)^2, \quad B_{\max} = 2\left|\gamma - \frac{1}{3}\right|. \tag{5.10}$$

For $\frac{2}{3} \leq \gamma \leq 1$, these limits are [dotted-blue and dashed-red lines in Figs. 5.1(c) and 5.1(d)]

$$D_A = D_B = 0, \quad B_{\max} = 2\sqrt{2}\sqrt{\gamma^2 + (1-\gamma)^2}, \tag{5.11}$$

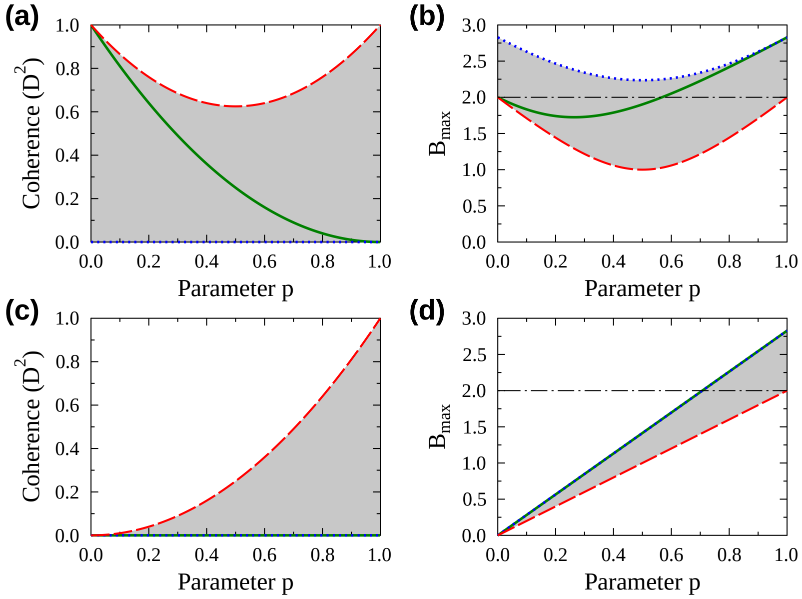

Figure 5.2: Coherence (D^2) and maximal violation of the CHSH inequality (B_{max}) for (a) and (b): example III ($\hat{\rho}_{\text{EXC}}$); and (c) and (d): example IV ($\hat{\rho}_{\text{W}}$). Green lines depict the values of the original state, prior to any unitary transformation. The maximal coherence and minimal violation of the CHSH inequality are marked by dashed-red lines, and the minimal coherence and maximal violation of the CHSH inequality are marked by dotted-blue lines. The black dashed-dotted line represents the classical correlation limit $B_{\text{max}} = 2$. Grey areas correspond to all admissible values achievable by all unitary operations.

and

$$D^2_{\text{max}} = \gamma^2 + (1-\gamma)^2 , \quad B_{\text{max}} = 2|2\gamma - 1|. \tag{5.12}$$

The green lines in Figs. 5.1(c) and 5.1(d) show the actual value of D^2 and B_{max}, prior to the application of any unitary transformation.

Example III: State considered in [33].–Kagalwala et al. investigated (example C) a state whose density matrix writes

$$\hat{\rho}_{EXC}(p) = \frac{1}{2}\begin{pmatrix} 1-p & 0 & 1-p & 0 \\ 0 & p & ip & 0 \\ 1-p & -ip & 1 & 0 \\ 0 & 0 & 0 & 0 \end{pmatrix} \text{ where } p \in \langle 0,1\rangle. \quad (5.13)$$

The purity of this state is $\mathcal{P} = 1-\frac{3}{2}p+\frac{3}{2}p^2$. In Figs. 5.2(a) and 5.2(b) all possible values of D^2 and $B_{\max}$ are shown for this particular case. The boundaries of the grey areas are formed by the states with minimal coherence and maximal violation of the CHSH inequality

$$D_1 = D_2 = 0, \quad B_{\max} = 2\sqrt{2}\sqrt{1-\frac{3}{2}p+\frac{3}{2}p^2}, \quad (5.14)$$

and the maximal coherence and correspondingly minimal violation of the CHSH inequality

$$D^2_{\max} = 1-\frac{3}{2}p+\frac{3}{2}p^2, \quad B_{\max} = 2\sqrt{1-3p+3p^2}. \quad (5.15)$$

Note that in [33], the $B_{\max}$ for the minimal coherence and maximal violation of the CHSH inequality case, is calculated considering only projections into a subset (equivalent to considering only linear polarization states) of all the possible states that should be considered. However, the correct calculation of $B_{\max}$ needs to consider all possible measurements (projections), as shown in [105].

Example IV: Werner state.–As a final example we consider the Werner state [28], which is defined as

$$\hat{\rho}_{\mathrm{W}}(p) = \frac{1}{4}\begin{pmatrix} 1+p & 0 & 0 & 2p \\ 0 & 1-p & 0 & 0 \\ 0 & 0 & 1-p & 0 \\ 2p & 0 & 0 & 1+p \end{pmatrix} \text{ where } p \in \langle 0,1\rangle. \quad (5.16)$$

The purity is $\mathcal{P} = (1 + 3p^2)/4$. When this state is transformed, D^2 and $B_{\max}$ can attain any value inside the grey areas in Figs. 5.2(c) and 5.2(d). For these plots, the limits are

$$D_1 = D_2 = 0, \quad B_{\max} = 2\sqrt{2}p, \tag{5.17}$$

for minimal coherence and maximal violation of the CHSH inequality and

$$D^2_{\max} = p^2, \quad B_{\max} = 2p, \tag{5.18}$$

for maximal coherence and minimal violation of the CHSH inequality

5.4 The relationship between coherence and correlations

For a given quantum state, the relationship between the degree of coherence of each subsystem and the correlations between subsystems is quantified by the measure $S_{A,B} = D^2_{A,B}/2 + \left(B_{\max}/2\sqrt{2}\right)^2$ called accessible coherence in the subsystem A, B [33]. Especially, for a pure state the statement

$$\frac{D^2_{A,B}}{2} + \left(\frac{B_{\max}}{2\sqrt{2}}\right)^2 = 1, \tag{5.19}$$

is valid. Any increase (or decrease) of the degree of coherence is compensated by a corresponding change of $B_{\max}$. This relationship is no longer true for mixed states as shown in the Appendix B.

What is then, for all states, the appropriate equation that relates first-order coherence and correlations? For a generally mixed state ($\mathrm{tr}[\hat{\rho}^2] \leq 1$), one can derive [105]

$$\frac{D^2_A + D^2_B}{4} + \mathcal{T} = \mathrm{tr}[\hat{\rho}^2], \tag{5.20}$$

where $\mathcal{T} = 1/4\,(1 + \sum_{i,j=1}^{3} t^2_{ij})$, $t_{ij} = \mathrm{tr}\,[\hat{\rho}\hat{\sigma}_i \otimes \hat{\sigma}_j]$, and $\sigma_{i,j}$ $(i, j = 1, 2, 3)$ are Pauli matrices. The values of t_{ij} can only be obtained by making coincidence measurements between the subsystems, therefore measuring the nature of its correlations. In general

$$\frac{(\lambda_1+\lambda_4)^2+(\lambda_2+\lambda_3)^2}{2} \leq \mathcal{T} \leq \mathrm{tr}[\hat{\rho}^2]. \tag{5.21}$$

For a pure state, $D_A = D_B$ and $\mathcal{T} = (B_{\max}/2\sqrt{2})^2$, so one obtains Eq. (5.19). For maximally entangled states, $B_{\max} = 2\sqrt{2}$, so $\mathcal{T} = 1$ achieves its maximum value, while for separable pure states, $B_{\max} = 2$ and $\mathcal{T} = 1/2$.

CHAPTER
SIX

INDUCED OPTICAL COHERENCE TOMOGRAPHY WITH FREQUENCY-ENTANGLED PHOTONS

Coherence is one of the most important and fundamental aspects of electromagnetic theory, both in the classical and quantum regimes. It is also a resource that can have important practical applications. In 1991, Huang et al. [128] demonstrated a new way of obtaining high-resolution images of three dimensional samples with great resolution in both the transverse and axial domains. In order to demonstrate the usefulness of the new scheme, they applied the interferometric measures to obtain accurate images of the different layers that make up the retina. They called the new method optical coherence tomography (OCT).

In OCT, different layers of the sample under study present a different reflectivity, and this is the variable that is measured. The reflection coefficient τ between two layers with refractive index n_1 and n_2, under normal incidence, is

$$|\tau| = \left| \frac{n_1 - n_2}{n_1 + n_2} \right| . \tag{6.1}$$

Now considering multiple layers, to differentiate light reflected from one specific layer from all others, one needs to use a low-coherence source, so this method could also have been called low-coherence interferometry. Therefore the role of coherence in optical coherence tomography is to separate one axial section of the sample from the rest of the sample, i.e., to select the measurement of reflectivity from a specific depth inside the sample.

In this chapter we present *a new type* of optical coherence scheme, where the reflectivity of the sample is no longer directly measured. Instead it induces a change of optical coherence that is indeed measured. Therefore optical coherence plays a double role in our scheme: i) it carries the sought-after information about the reflectivity of the sample and ii) it provides axial sectioning of the sample.

We consider first-order coherence [41,42] and make use of frequency-entangled photons generated in two separated SPDC sources [129]. In addition to subtle fundamental differences between *standard* OCT and our scheme, that it might be called *induced optical coherence* tomography (iOCT), our scheme can provide some practical advantages. For instance, it allows to use light at a certain wavelength to probe the sample, while measurements can be made at another wavelength more convenient for detection.

6.1 Introduction

Coherence plays a fundamental role in OCT, being one of these cases where fundamental results of optical coherence theory have found an application in biomedical science. OCT is a non-invasive opti-

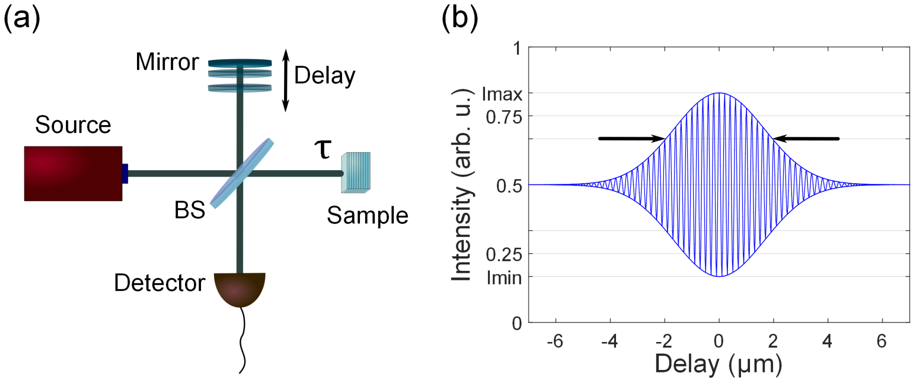

Figure 6.1: General scheme of an optical coherence tomography (OCT) setup. (a) Typical setup for OCT measurements. (b) Typical interferogram that is the result of the measurement. Here we show a particular example, with a chosen visibility of $V = 60\%$ and an axial resolution of approximately 3.5 μm.

cal imaging technique that permits cross-sectional and axial high-resolution tomographic imaging of biological tissue. Tissues such as coronary artery or retina are the ones that are more commonly diagnosed with this technique. OCT measures the interference of light reflected back from the sample with a reference beam reflected from a mirror [128], as it is shown in the example of Fig. 6.1(a).

High-resolution in the transverse domain is obtained by using highly focused beams, while high-resolution in the axial domain is obtained by making use of the interference of broadband light in a Michelson interferometer. One common and easy way to generate broadband light is by means of the generation of continuous-wave (CW) light with extremely low-coherence. In other words, the low-coherence of the source light holds the key to achieve high-resolution in the axial direction. Figure 6.1(b) shows a typical result of interference in an OCT scheme. As a result of interference, the output signal shows maxima and minima of intensity as a function of the path difference between the two arms of the interferometer. If τ designates

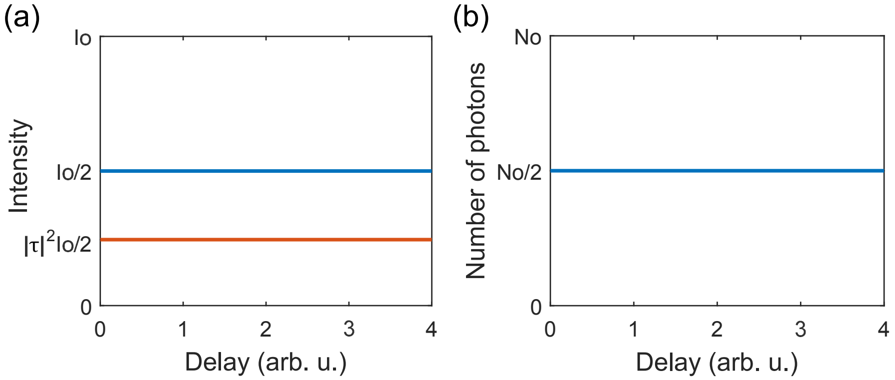

Figure 6.2: Some subtle differences between *standard* OCT and *induced optical coherence* tomography (iOCT), that can help to clarify differences between both schemes. We plot the intensity (or photon flux) traversing each of the two arms of the interferometer, before the BS. (a) In *standard* OCT, the intensity of the reference beam is $\mathrm{I}_0/2$, while the intensity coming from the sample is $|\tau|^2\mathrm{I}_0/2$. (b) In iOCT, the two signal beams in each arm, that are made interfere, contain $\mathrm{N}_0/2$ photons, independently of the reflectivity value (τ). I_0 is the total intensity and N_0 is the total number of photons propagating in the interferometer.

the reflectivity of a particular layer of the sample, the visibility of the interference pattern is

$$V = \frac{\mathrm{I}_{\max} - \mathrm{I}_{\min}}{\mathrm{I}_{\max} + \mathrm{I}_{\min}} = \frac{2|\tau|}{1 + |\tau|^2}, \tag{6.2}$$

where $\mathrm{I}_{\max}$ and $\mathrm{I}_{\min}$ are the maximum and minimum intensities detected after the BS. The bandwidth of the source, and thus its coherence length, determines the axial resolution of the measurement.

For each axial measurement, the two waves interfering show coherence at some selected axial distance, so the low-coherence provides the position of the reflectivity measurement, i.e., the exact depth into the tissue that is being analysed. However, OCT still performs direct measurements of the reflectivity (τ) of the sample. As we can see in Fig. 6.2(a), light traversing one of the two arms of the Michelson interferometer carries information about the reflectivity of the sample (τ). This means that OCT *does not measure coherence* as the name of the technique might wrongly induce to claim. This is why some people [130] like to clarify that the name of the technique should have been called more properly *white-light interferometry* or *broadband interferometry*.

The experimental setup we consider in this chapter is based on the concept of induced coherence, an idea put forward in 1991 by Zou et al. [129]. In their study they demonstrated the possibility of inducing coherence making use of low-efficiency spontaneous parametric down-conversion (SPDC) sources. In their experiments, they built a single-photon Mach-Zehnder interferometer formed by a pump beam that is divided to pump two nonlinear crystal starting the interferometer. The crystals are used to spontaneously generate two signal-idler photon pairs with low-efficiency.

The interference pattern appears when the two signal photon arms are recombined, only if the idler photons become indistinguishable. The degree of distinguishability of the idler photons generated in each nonlinear crystal, and its effect on the nature of the interference pattern of signal photons, is commonly called *which-way* information. The term comes from knowing in which of the two crystals the signal photon has been generated, just by having the possibility to detect the idlers. So, if we cannot differentiate the two idlers, there is no way to know in which of the two arms we have the signal photon.

Figure 6.2 shows a subtle difference between both approaches. We can see in Fig. 6.2(b) that the optical beams traversing the two arms of the interferometer in our scheme have the same photon flux $N_0/2$ for all the possible values of the reflectivity (τ). This is in contrast to the case of *standard* OCT, as shown in Fig. 6.2(a), where the intensity of light coming from the sample contains a different number of photons that the reference beam, the one reflected from the movable mirror.

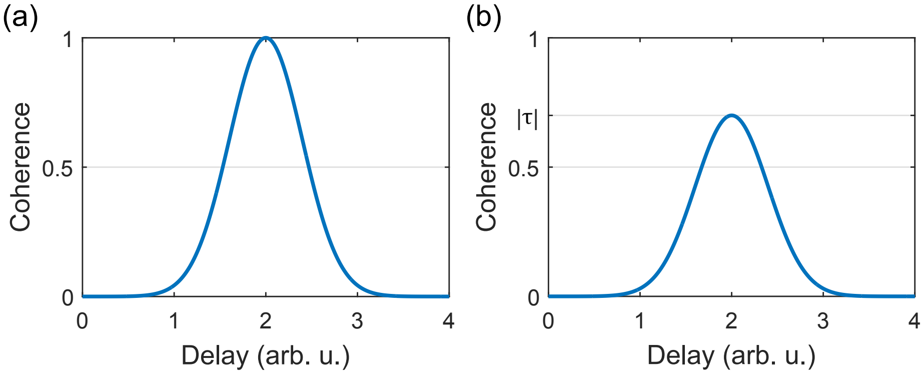

Figure 6.3: Degree of coherence between the light beams propagating in the two arms of the interferometer (as described in Appendix C). (a) Coherence in *standard* OCT, and (b) Coherence in *induced optical coherence* tomography (iOCT).

In the system that we describe in detail in the next section, the reflectivity (τ) of the sample, placed between the two crystals used to generate the signal-idler paired photons, is directly related to a loss of coherence between the two signal photons. Therefore, we measure coherence instead of reflectivity, even though this loss of coherence can be finally related linearly to the reflectivity of the sample. However, the curve shown in Fig. 6.1(b) still can be considered as an example of a possible experimental result when one uses our technique, so from this result one cannot deduce which approach was used since both give the same results, when having the same emitted bandwidth from the source. Our scheme provides no change of axial resolution nor the visibility when compared with *standard* OCT.

In other words, in spite that typical experimental outcomes, shown in Fig. 6.1(b), are equal for both techniques if the bandwidth of the light is similarly equal, there are subtle fundamental differences between the two techniques. Figures 6.2 and 6.3 summarizes schematically the main differences between *standard* OCT, an imaging system that measures reflectivity, and *induced optical coherence* tomography (iOCT), a system that measures the loss of coherence induced by the presence of a lower than 1 value of reflectivity.

Firstly, the variable that is measured is different. In Fig. 6.2(a) we see that the reflectivity (τ) of the sample changes the intensity of light that traverses one of the arms of the *standard* OCT interferometer, while Fig. 6.3(a) shows that the degree of coherence between the light beams traversing different arms remains unchanged (see Appendix C for a more detailed discussion). However, in our iOCT case, the same flux of photons traverses the two arms of the interferometer, as shown in Fig. 6.2(b), but the degree of coherence now changes, as it is depicted in Fig. 6.3(b). As we will see, this can offer some potential advantage over the use of *standard* OCT.

6.2 Experimental setup

Note: we acknowledge the restless contribution of Gerard Jiménez in the process of building the experimental setup and measuring the results, during his bachelor thesis under the supervision of J. P. Torres. The experimental setup used in our experiment is shown in Fig. 6.4. The laser that pumps the two nonlinear crystals is a high-power continuous-wave (CW) Verdi V10 (Coherent). It emits light at a wavelength of 532 nm. Right after the laser, a linear attenuator is implemented in order to control the polarization and power of the pump beam. We have also located a short-pass filter (SPF) in the pump beam path. The reason is that the Verdi V10 laser is pumped by two diodes centred at 808 nm, light that is absorbed by a neodymium-doped yttrium vanadate (Nd:YVO4) crystal, re-emitted at a wavelength of 1064 nm and frequency-doubled by a lithium triborate (LBO) crystal inside a ring cavity configuration. All these steps are necessary to obtain the desired 532 nm coherent pump beam. The residual 808 nm light coming from the diodes appeared in our first measurements as noise. This is why it has to be filtered out with the short-pass filter.

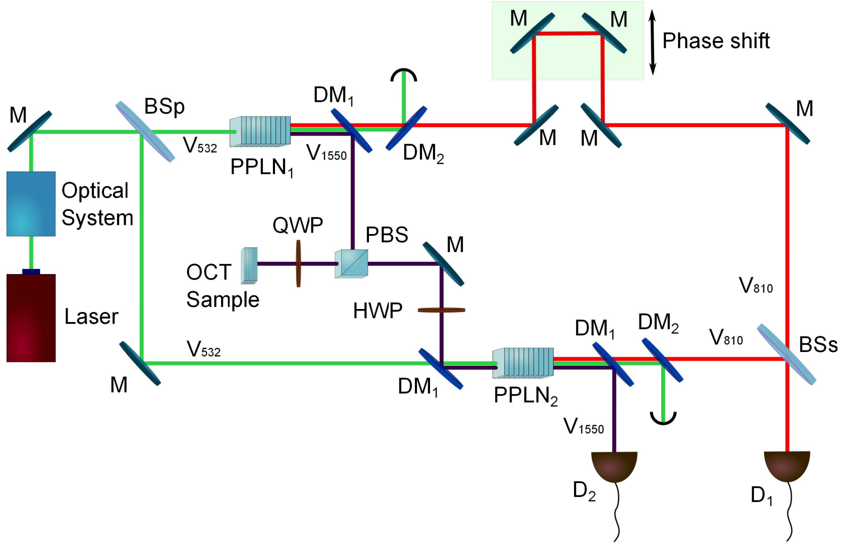

Figure 6.4: Experimental setup aimed at observing induced optical coherence. Laser: Verdi V10 (Coherent). Optical system: linear attenuator (LA) and short-pass filter (SPF). BSp&s: beam splitters for the pump and the signals. $PPLN_{1\&2}$: periodically-polled lithium niobate (nonlinear crystals). $DM_{1\&2}$: dichroic mirrors. OCT Sample: simulated by a mirror and a variable neutral density filter. Phase shift: 6-mm-long stepper motor (Thorlabs Z806). QWP: quarter-wave plate. HWP: half-wave plate. D_1: single-photon counting module. D_2: optical spectrum analyzer (OSA) for telecom band.

The pump beam is split with a 50:50 beam splitter (BSp), so that the same pump power illuminates the two nonlinear crystals. The two periodically-polled lithium niobate (PPLN) nonlinear crystals located in each beam of the pump, absorbs with very low probability a 532 nm pump photon and re-emits two lower-frequency photons, signal and idler, by means of the nonlinear process of spontaneous parametric down-conversion (SPDC). The SPDC process is non-degenerate type-0, meaning that all three photons, pump, signal and idler, have the same vertical polarization, and the resulting signal (810 nm) and idler

(1550 nm) photons are generated with different central wavelengths. The efficiency of the SPDC process is low, so we can neglect the probability to generate two pairs of signal-idler photons, each pair in a different crystal, at the same time.

The *induced optical coherence* tomography (iOCT) measurement is carried out by detecting the interference between the two 810 nm signal photons. Even though, it is the 1550 nm idler photon coming from PPLN_1 the one interacting with the sample. This can be done because, the signal and idler photons are separated by a dichroic mirror (DM_1), where the 810 nm signal photon from the first nonlinear crystal (PPLN_1) is transmitted, forming the upper arm of the Mach-Zehnder interferometer, until it arrives to the beam splitter of the signal photons (BSs). The 1550 nm idler photon coming from PPLN_1 is the one reflected in the dichroic mirror DM_1, starting the lower interferometer arm. It is reflected again in the polarization beam splitter (PBS), due to its vertical linear polarization, and then is being changed to circular polarization when traversing the quarter-wave plate (QWP).

The 1550 nm photon interacts with the sample, formed by a variable neutral density filter and a mirror, which reflects it back into the QWP again to change its polarization now to linear horizontal. This photon, now carrying the information of the sample (τ), is transmitted through the PBS this time, due to its horizontal polarization, but it has to be rotated again to vertical polarization with a half-wave plate (HWP) in order to be able to lose completely all the possible distinguishability with respect to the second 1550 nm idler photon. With another dichroic mirror DM_1, the 1550 nm idler photon that is generated in the first nonlinear crystal overlaps spatially with the pump beam that illuminates the second nonlinear crystal, and consequently also with the second 1550 nm idler photon.

In Figs. 6.5 to 6.8 are shown some pictures taken from different parts of the setup used to measure the *induced optical coherence* tomography (iOCT).

Note that for the sake of simplicity of the explanation of the

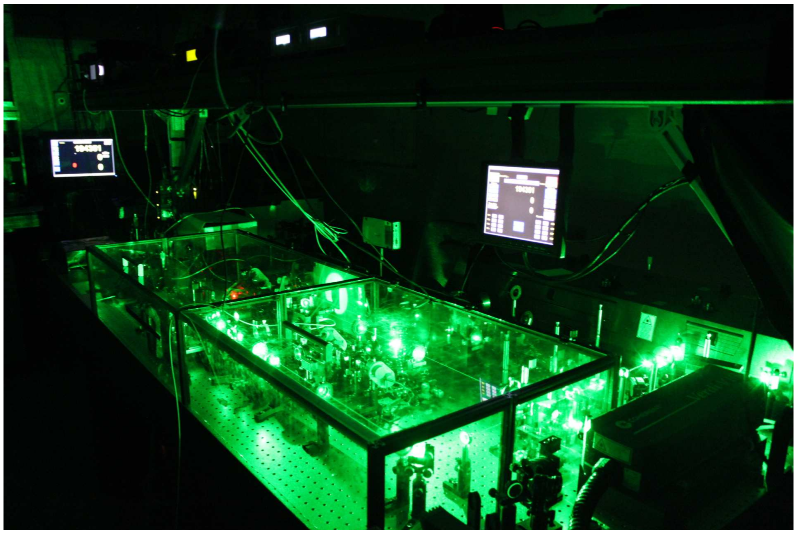

Figure 6.5: Picture of the whole setup covered with a methacrylate box to prevent air fluctuations in the interferometer.

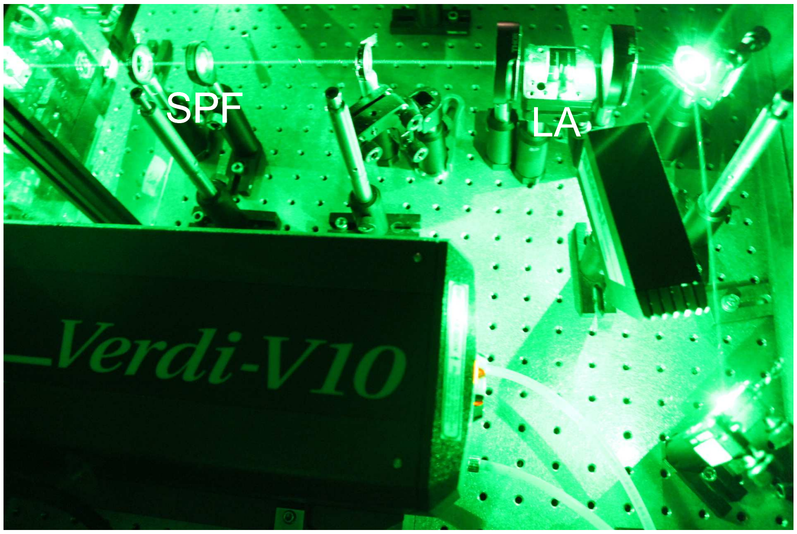

Figure 6.6: Picture of the section of the setup where the pumping beam is attenuated, filtered and correctly polarized.

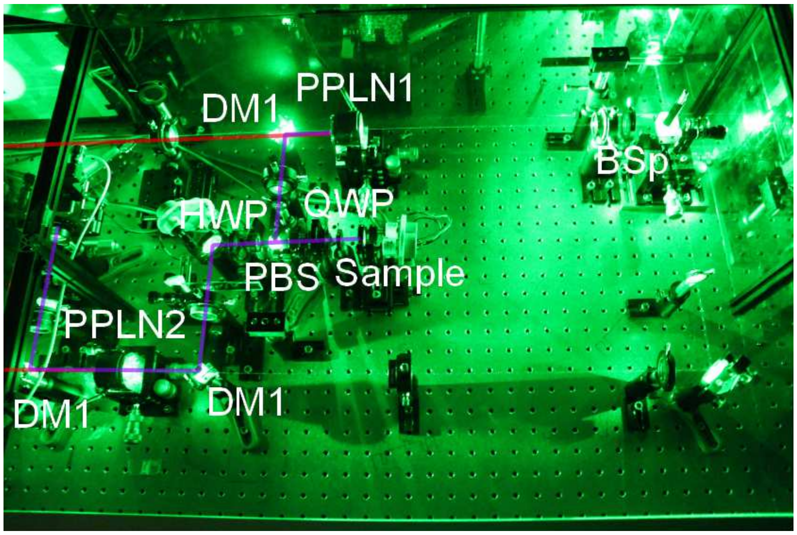

Figure 6.7: Picture of the section of the setup where the SPDC photon pairs are generated and the sample that induce coherence is located.

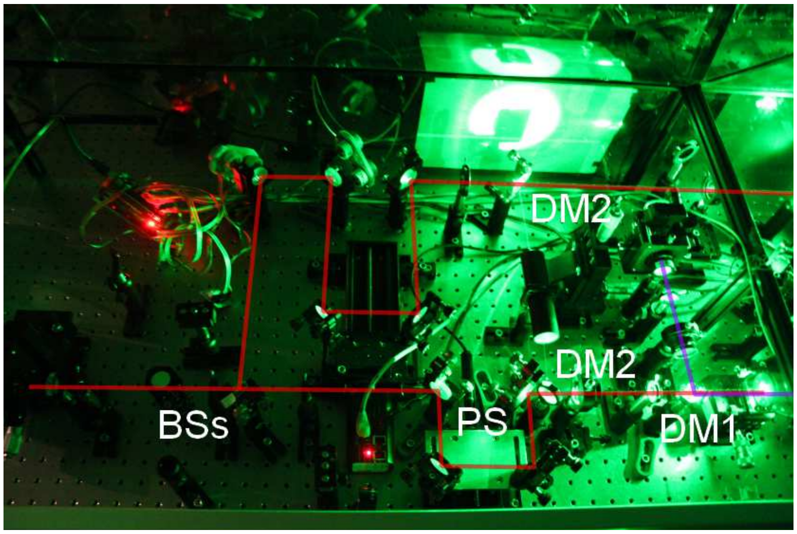

Figure 6.8: Picture of the section of the setup where photons traversing the two interference arms are recombined and fiber coupled.

setup, the focal distances and position specifications of the lenses are not shown. However the exact position of the lenses in this lower interference arm, have an important role when the distinguishability between the two idler spatial modes is at stake.

After the second nonlinear crystal (PPLN$_2$), the second signal photon is separated from the two spatially overlapped idler modes, that are reflected in the last DM$_1$ and coupled into a single mode fibre for alignment purposes. So, the second 810 nm signal photon continues the lower interferometer arm until it reaches the BSs. A phase shift is introduced in one of the two arms, formed by two mirrors implemented on top of a platform, and being able to perform steps of 30 nm thanks to a 6-mm stepper motor (Thorlabs Z806) attached to it. The two 20-mm-long PPLN crystals are mounted on top of ovens, being able to adjust their temperature by tenth of degrees Celsius. This change of temperature induces a variation in the response of the nonlinear crystals, leading to different phase-matching conditions for each temperature. The idler photons are coupled in order to be able to perform spectral measurements with an optical spectrum analyser (OSA), to oversee the spectral overlapping between the two PPLN crystals. Although, the detection of the 1550 nm photons is not necessary for the correct functioning of the iOCT setup, it is detected for monitoring purposes.

The pump beam at 532 nm is separated from the signal after being reflected in the dichroic mirrors DM$_2$. The residual pump power existing in the output port of the BSs, also overlapped with the interference signal from the two 810 nm photon input arms, is filtered out by a band-pass filter (BPF). Finally, the interference signal is coupled into a single mode fibre and measured with a silicon based single photon detectors (Perkin-Elmer).

The results presented in the next section are interferometric measurements, and for making it clearer, we describe in detail what constitute the arms of the interferometer. Here the Mach-Zehnder interferometer starts in the PPLN$_1$. One upper arm is formed by the 810 nm signal photon generated in the first nonlinear crystal until it reaches the beam splitter BSs. The lower arm is formed by the 1550 nm idler photon generated also in the first nonlinear crystal, until it reaches the second nonlinear crystal ($PPLN_2$). It continues with the 810 nm signal photon generated in the second nonlinear crystal until it reaches the other input port of the the beam splitter BSs.

6.3 Results

We should remark that the results obtained with the experimental setup just described, constitute a *proof-of-concept* of the idea of *induced optical coherence* tomography (iOCT). For the sake of comparison, *standard* OCT techniques commonly make use of broad-band LED light sources, with a spectral emission of more than 100 nm at full-width at half maximum (FWHM). In this way they are able to perform measurements with axial resolutions of the order of a few microns, as shown in the example of Fig. 6.1(b).

This means that the resolution and visibility of the curves shown in this section can be improved and further aligning improvements, among others, are being made while submitting this manuscript. Notice that erasure of distinguishability between paired photons generated in different nonlinear crystals is in general a highly demanding experimental task. In a recent work by Barreto et al. [131], they used a very similar experimental setup to the one we use and they obtained a visibility value of $V = 77\%$. In the original paper from 1991 where the idea of induced coherence was introduced by Zou et al. [129], they were able to obtain a visibility of $V = 30\%$. These values show how difficult can be to successfully overlap spatial modes when large bandwidths are considered, and to compensate all the different degrees of freedom involved in the system that can provide unwanted path distinguishability. We continue improving and *reshaping* things in order to increase the values of the visibility. The results could also be improved in the future by introducing new sources as proposed in the discussion section of Chapter 7.

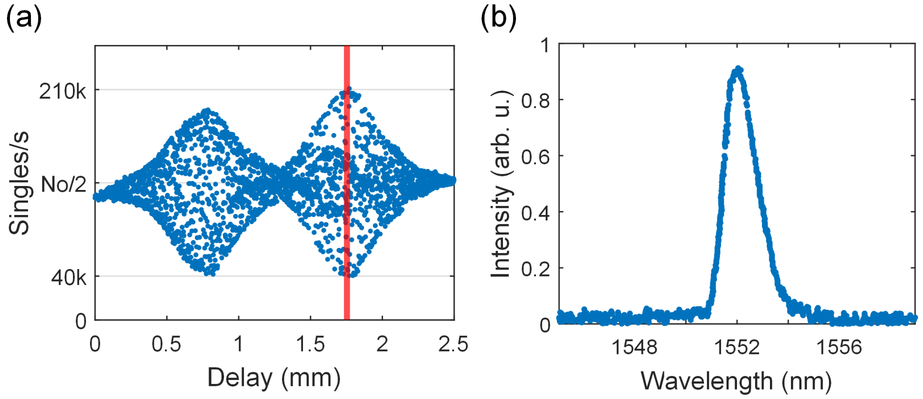

Figure 6.9: Experimental *induced optical coherence* tomography results. (a) Degree of coherence measured simulating two layer transitions 1-mm apart, by detecting the 809.4 nm photons at the output of BSs. Changing for every depicted point the path difference by micrometric steps ($1\,\mu$m), obtaining a maximum visibility value of $V = 68\%$ marked with the red rectangle. (b) Digitalized spectrum bandwidth measurement of the SPDC idler emission, centered at 1552.3 nm and with a 1.6 nm bandwidth at FWHM.

Figure 6.9(a) shows the measurement of the degree of coherence between signal photons, when the idler photon generated in the first nonlinear crystal is reflected from a mirror ($|\tau| = 1$) that can be moved between two positions. With this we aim at representing the detection of two reflecting layer transitions separated by 1-mm distance. The resulting measurement curve shows clearly the corresponding coherence function shapes simulating two layer transitions 1-mm apart. The coherence function on the left is of different visibility ($V = 64\%$) than the one on the right, with a visibility of $V = 68\%$. The difference is caused by the fact that signal coupling optimization was performed for one location of the mirror, so when displaced a small decrease of visibility can be expected. In these results we made use of the full bandwidth of the paired photons generated in both crystals, and changing the difference path length of

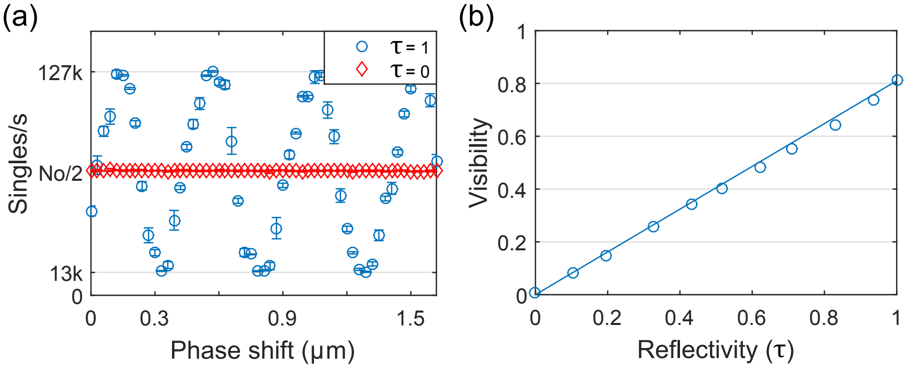

Figure 6.10: (a) Interference fringes for different values of the reflection coefficient (τ) measured with nanometric steps within the red area marked in Fig. 6.9(a), which corresponds to the maximum visibility position. The irregularities in the phase for each interference pattern are due to miss-alignment and malfunctioning of the stepper motor. Circles, $|\tau| = 1$; and diamonds, $|\tau| = 0$. The maximum visibility value obtained is $V = 81\%$. The error bars designates the standard deviation of the experimental measures. (b) Experimental relation of the interference pattern visibility with respect to the reflectivity (τ) values of the simulated OCT sample. The open circles are the experimental visibility measurements and the solid curve stands for the theoretical prediction for our particular visibility conditions (see Appendix C).

the two interferometric arms by micrometric steps (1 μm).

The coherence length and shape of the coherence functions are directly related with the shape and bandwidth of the emitting source, shown in Fig. 6.9(b). In our case, the 20-mm-long PPLN type-0 crystal generates a SPDC idler spectral emission bandwidth of about 1.6 nm at FWHM, measured with an optical spectrum analyser (OSA), corresponding to approximately 0.5-mm axial resolution in the interferometric measurements. The OSA that we used could not extract data from the measured spectrum. Therefore, we digitalized the measured spectrum bandwidth of the SPDC idler emission, by taking first a picture directly of the screen of the OSA, and digital rendering it with WebPlotDigitizer.

Measurements showed that the spectrum of the photon pairs that are fibre coupled from each crystal are slightly different. This is a source of spectral distinguishability between SPDC photons coupled from different crystals, and therefore of loss of coherence and decrease of visibility.

In Fig. 6.10(a) we show the number of signal photons detected in one of the output ports of the BSs, with respect to variations in length of one arm with respect to the other. The path difference in this case are steps of the order of tens of nanometres ($\sim$ 30 nm). Interference fringes appear ($|\tau| = 1$) with different visibility as the one shown in Fig. 6.9(a), where we marked with a red rectangle the small area where the nanometric step results have been carried out. We also show (red diamonds) the effect of blocking the first 1550 nm idler photon arm, that simulates the presence of a sample with no reflectivity ($|\tau| = 0$).

In these measurements the bandwidth of the signal photons is filtered with the help of a 10-mm fibre Bragg grating (FBG). The central wavelength of the FBG filters at room temperature is at 809.4 nm. This central wavelength can be modified by changing the temperature of the FBG or stretching it, but we decided to change the temperatures of the PPLN ovens instead. For that reason the central wavelength of the SPDC idler spectrum in Fig. 6.9(b) is around 1552.3 nm. Note that for the sake of simplicity in the setup description, we did not give the value of the central wavelength before.

On the one side, filtering out the bandwidth helps to reduce the distinguishability of paired photons that originates in different nonlinear crystal, erasing the undesired spectral distinguishability. For that reason, the maximum visibility measured in Fig. 6.10(a) increases now up to $V = 81\%$. On the other side, after filtering the signal photons with the FBG, the coherence length turns out to be of the order of tens of centimetres. This is due to the narrow bandwidth

($B_s \sim 0.1$ nm) that is reflected from the FBG. Therefore axial resolution degrades. Notwithstanding, we can still see the effect of changing reflectivity on the visibility. Figure 6.10(b) depicts the experimental relationship between the visibility of the interference pattern and the reflectivity. We consider for this plot more values of τ than the ones showed in Fig. 6.10(a), in order to avoid overpacked curves. The different experimental data corresponds to the visibility of the phase fringes measured with respect to the different values of the reflection coefficient (τ). The value of τ is introduced by a variable neutral density filter (NDF) in the path of the first 1550 nm idler photon. The variable NDF is formed by a long rectangular glass structure with different attenuation density indexes along its facet.

All the results shown in this chapter are raw experimental data. Meaning that no dark counts ($\sim$ 2k) have been removed from the measurements, neither for the visibility calculations or the curves depiction. This means that with dark count subtractions our results of visibility would be even higher.

CHAPTER

SEVEN

CONCLUSIONS

Here we summarize the main results and ideas presented all along the thesis. As it can be seen in this discussion section, we focus in the most technical part of this thesis, where we think further advances can still be made.

7.1 Summary

Entanglement seems to be a ubiquitous concept that, even though it was introduced to explain a very specific phenomenon of quantum theory, it can apply as well in many other different scenarios.

Here in **Chapter 2** we have shown that indeed this should not be unexpected, because when considering correlations between different parties—namely photons, degrees of freedom or sites in molecular systems—in the important case of the single-excitation manifold, entanglement is equivalent to coherence or, more specifically, to coherent delocalization. Thus, we have investigated the conditions for the existence of entanglement, or lack of it, in three different systems: i) the process of exciton transport in photosynthetic light-harvesting complexes, which is generally modelled as a single excitation propagating in an N-site network, ii) the two-photon state generated by means of spontaneous parametric down-conversion in nonlinear crystals and iii) the coupling between different degrees of freedom of a single photon.

Our results show that even though the physical scenarios of all the cases considered here are different, their mathematical equivalence is what allows one to expect and observe entanglement in each one of them. Furthermore, we have seen that within the single-excitation Hilbert subspace any measure of entanglement is equivalent to a measure of the degree of coherence and localization. This implies that any system that may be described in a similar manner to the single-excitation manifold will exhibit entanglement as long as coherence and delocalization between its subsystems are preserved.

Finally, we have explored the reason why entanglement can even be observed in classical coherent systems [31–33]. The analysis presented here demonstrates that the observation of entanglement, even if the system can be described classically, should not be unexpected because the concept of entanglement in the single-excitation manifold is essentially the same as coherence.

The results demonstrating the generation of polarization-entangled paired photons in a semiconductor platform, the Bragg reflection waveguide (BRW), are presented in **Chapter 3**. We have demonstrated visibilities higher than 90% in all the measured bases, a requisite for obtaining high quality entanglement. It has also been experimentally demonstrated that the generated two-photon state clearly violate the CHSH inequality, and that the presented BRW source can be considered an expedient source of high-quality polarization-entangled two-photon states, capable of being implemented in a integrated circuit. In the discussion section, there will be some examples showing in which direction this research area could thrive.

Following the statements of Chapter 2, we have demonstrated experimentally in **Chapter 4** that there exist a full analogy between the general quantum state (pure or mixed) that describes two-photon states entangled in its polarization degree of freedom and the correlations (coherent or noncoherent) existing between the polarization and spatial degrees of freedom of a single photon. Along these lines, concepts such as purity and degree of entanglement or concurrence can be used to describe coherent and noncoherent correlations between properties of a single system. This fact naturally allows one to use Bell's inequalities to characterize both types of systems, as we have demonstrated here.

In **Chapter 5** we have solved several puzzles about the relationship between coherence and certain measures of correlations between subsystems, as it is the case of the CHSH inequality. For the case of two correlated two-dimensional subsystems, we have obtained simple expressions that quantify the amount of first-order coherence that can be obtained in each subsystem (hidden coherence) by modifying correlations between the subsystems. We have shown that the relevant parameter to quantify the maximum hidden coherence is the degree of violation of the CHSH inequality, not the degree of entanglement between subsystems, i.e., the concurrence. Although we have considered here only a few systems as examples, their analysis, based on suitably defined quantities, illuminates the general concept of extracting coherence from manipulating the correlations between subsystems.

Lastly, in **Chapter 6** we have introduced the basic principles of a new type of optical coherence tomography (OCT) scheme that we call *induced optical coherence* tomography (iOCT). We have demonstrated it using frequency-entangled photons generated in a SPDC process. From a fundamental point of view, iOCT is a *proper* coherence measurement, in contrast to *standard* OCT. That is because *standard* OCT, in spite of its name, it does not measure coherence but reflectivity of the sample. In our scheme we measure coherence, whose value depends on the reflectivity of the sample, i.e., the change of reflectivity induces a direct change of the coherence of two streams of photons that are made to interfere. From a practical point of view, the photons that are being measured never interacts with the sample. That is to say, the *induced optical coherence* tomography (iOCT) measurement is able to work by detecting photons centred at the maximum efficiency of the silicon detectors, while the sample is being analysed with photons around the telecom band, photons around 1550 nm, that can penetrate deeper into human tissue.

7.2 Discussion

The results of the experiment presented in **Chapter 3** can signal a route towards the implementation of quantum technologies on-chip. The implementation of entanglement generators on semiconductor platforms, such as the Bragg reflection waveguide (BRW), can take the quantum communication and quantum computing fields to a higher level of industrial implementation [66]. As we stated in the main text, the brightness and quality of such sources are not yet ready to compete with the ones already in the market, for that reason we will discuss what we think would be the following steps to improve the present results and the possible outcomes for this research field.

Alternative BRW configurations with no need of post-selection of down-converted photons can be implemented using, for instance, the concurrency of two conversion processes [132], or non-degenerate SPDC, where signal and idler photons bear different wavelengths [133], also useful for their implementation in the iOCT scheme of Chapter 6 as a broadband coherent sources. For this, one can make use of the great versatility offered by BRWs and design the layer structure to achieve phase-matching at the required wavelengths.

Optimization of the generation rate of down-converted photons can be achieved by optimizing the layer thicknesses and Al concentrations, so that the mode overlap between photons at different wavelength increases. BRW made of AlGaAs can potentially offer higher generation rates than ferroelectrical waveguides made of PPLN or PPKTP, since they show a much higher second-order nonlinear coefficient. However, in practice, both the pump and the down-converted modes are subject to losses, chiefly by two processes: radiation losses, mainly in the Bragg modes, and scattering of light due to surface roughness [134]. Fortunately, improvements in design and fabrication of the BRW could reduce the losses of the pump and down-converted waves, and increase mode overlap and enhance the coupling efficiency of the pump light into the pump mode that propagates in the waveguide.

It is important to note that the platform described and used here, offers the unique possibility of integrating the pump laser with the nonlinear element to enable self-pumped on-chip generation of polarization entanglement, without the use of off-chip compensation and bandpass filtering, as it is done in this work. There are two theoretical proposals to achieve this aim, both use dispersion engineering of the BRWs. One uses type-II process in a BRW with zero-GVM [97], while the other one uses concurrent type-I and type-0 processes [132]. Regarding the self-pumping part, we could expect in the future an electrically injected entangled photon-pair source. There is some work already performed in Helmy's group, where they reported for the first time an edge-emitting Bragg reflection waveguide laser, where the fundamental lasing mode is a Bragg mode [85], and electrically pumped parametric fluorescence was demonstrated subsequently [86].

In combination with the development of quantum circuits composed of properly engineered arrays of waveguides, and the integration of the laser pump source in the same chip, our results show that semiconductor technology based on the use of BRW in AlGaAs is a promising path to develop integrated entanglement-based quantum circuits.

If we focus now in the results of **Chapter 6**, we can find some promising prospects for the near future. Firstly, as a general rule in OCT techniques, the broader is the spectrum bandwidth, the better is the axial resolution. Fortunately, we can increase the bandwidth of down-converted photons, and therefore the resolution of OCT measurements. Values of a few hundreds nanometres can be generated by using shorter crystals or by appropriately engineering the phase matching conditions of longer crystals and BRWs of Chapter 3.

Secondly, other options can be implemented as well for this setup. For instance, changing the last beam splitter, where signal photons are combined, by a polarizing beam splitter (PBS), and introducing a half-wave plate in one arm before the PBS, it allows to perform measurements of polarization coherence, being the results analogous to the ones shown in Chapter 2. This allows to use all signal photons generated in both crystals for any value of the degree of coherence.

Finally, we want to remark that new connections between classical and quantum optics are being opened. Part of the work in this thesis goes along this direction, and specifically aims at opening such windows. This can help to better understand what is entanglement and what it means to violate a Bell's inequality. Or it can pave a new route towards the *simulation* of certain quantum features in new scenarios, making use of the mathematical similarities that underlie the functioning of different systems.

APPENDIX
A

THE CHSH INEQUALITY WHEN EXPERIMENTAL IMPERFECTIONS ARE CONSIDERED

A general expression of the CHSH inequality that takes into account certain experimental imperfections is deduced. As we will see, the relevant experimental parameter is the visibility that we observe in coincidence measurements results when performing a projection into an ensemble of quantum state, for instance, states of the form $\cos\alpha|H\rangle + \sin\alpha|V\rangle$.

Let us consider a quantum state of the form, similar to the one described in Chapter 4,

$$\begin{aligned}\rho &= \epsilon|\Psi\rangle\langle\Psi| \\ &\quad + \frac{1-\epsilon}{2} \times \left\{ |H\rangle_1|H\rangle_2\langle H|_1\langle H|_2 + |V\rangle_1|V\rangle_2\langle V|_1\langle V|_2 \right\}, \end{aligned} \tag{A.1}$$

where

$$|\Psi\rangle = 1/\sqrt{2}\,\left\{ |H\rangle_1|H\rangle_2 + |V\rangle_1|V\rangle_2 \right\}, \tag{A.2}$$

indexes 1 and 2 refers to photons 1 and 2. ϵ depends on the temporal delay (τ) between the photons with orthogonal polarization.

The purity of the state writes

$$\mathcal{P} = \mathrm{tr}(\rho^2) = \frac{1-\epsilon^2}{2}, \tag{A.3}$$

where tr $(\cdots)$ designates the trace. $\epsilon = 1$ corresponds to a pure state (optimum temporal delay), while $\epsilon = 0$ corresponds to a mixed state with the minimum purity, i.e., $\mathcal{P} = 1/2$ for a two dimensional system.

Given angles a (for photon 1) and b (for photon 2), the probabilities to detect in coincidence photon 1, when it is projected into the state $\cos a|H\rangle_1 + \sin a|V\rangle_1$ (with assigned value $+1$) or $-\sin a|H\rangle_1 + \cos a|V\rangle_1$ (with assigned value -1), and photon 2, when it is projected into the state $\cos b|H\rangle_2 + \sin b|V\rangle_2$ (with assigned value $+1$) or $-\sin b|H\rangle_2 + \cos b|V\rangle_2$ (with assigned value -1), are

$$\begin{aligned}
P_{++} &= \frac{\epsilon}{2}\cos^2(a-b) + \frac{1-\epsilon}{2}[\cos^2 a\cos^2 b + \sin^2 a \sin^2 b],\\
P_{--} &= \frac{\epsilon}{2}\cos^2(a-b) + \frac{1-\epsilon}{2}[\cos^2 a\cos^2 b + \sin^2 a \sin^2 b],\\
P_{+-} &= \frac{\epsilon}{2}\sin^2(a-b) + \frac{1-\epsilon}{2}[\cos^2 a\sin^2 b + \sin^2 a \cos^2 b],\\
P_{-+} &= \frac{\epsilon}{2}\sin^2(a-b) + \frac{1-\epsilon}{2}[\cos^2 a\sin^2 b + \sin^2 a \cos^2 b], \qquad (A.4)
\end{aligned}$$

where P_{++} designate the probability that photon 1 is projected into the state with assigned value $+1$ and photon 2 into the state with assigned value $+1$. Similarly for all other cases. Notice that $P_{++} + P_{--} + P_{+-} + P_{-+} = 1$.

The CHSH inequality consider expressions of the form

$$E(a,b) = P_{++} + P_{--} - P_{+-} - P_{-+}, \tag{A.5}$$

that reads

$$\begin{aligned}
E(a,b) &= \epsilon\cos 2(a-b) + (1-\epsilon)\cos 2a \cos 2b\\
&= \cos 2a\cos 2b + \epsilon \sin 2a \sin 2b. \qquad (A.6)
\end{aligned}$$

The CHSH inequality writes

$$S = E(a_1, b_1) - E(a_1, b_2) + E(a_2, b_1) + E(a_2, b_2), \tag{A.7}$$

The indexes 1 and 2 designate here two different angles for the projection of each photon. For $\epsilon = 1$, the maximum violation takes place for (first derivative with respect to a_1, b_1, a_2 and b_2 equal to zero)

$$\begin{aligned} &\sin(a_1 - b_1) = \sin(a_1 - b_2), \\ &-\sin(a_2 - b_1) = \sin(b_1 - a_2) = \sin(a_1 - b_1), \\ &\sin(a_2 - b_1) = -\sin(a_2 - b_2) = \sin(b_2 - a_2), \\ &\sin(a_1 - b_2) = \sin(a_2 - b_2). \end{aligned} \tag{A.8}$$

We consider the following angle relations between photon projections

$$\begin{aligned} a_1 - b_1 &= \theta, \\ b_1 - a_2 &= \theta, \\ a_2 - b_1 &= \theta, \end{aligned} \tag{A.9}$$

so that

$$a_1 - b_2 = 3\theta. \tag{A.10}$$

Thus, the value of the S parameter under these perfect conditions is

$$S = 3\cos 2\theta - \cos 6\theta. \tag{A.11}$$

Now, if we take into account accidental coincidences, optical element imperfections and/or miss-alignments during the measurement process, the S parameter can decrease its value.

For the sake of simplicity, let us consider the case $\epsilon = 1$. In the lab, the real coincidence fringe pattern measured follows the equation

$$N_{++} = \frac{A}{2}\cos^2(a - b) + C, \tag{A.12}$$

being N_{++} the number of coincidence detections when photon 1 it is projected into the state with assigned value +1 and photon 2 is projected into the state with assigned value +1. A and C are constants. C give the number of coincidences that are measured where none would be expected under ideal conditions, and A is the total number of coincidences (considering all possible projections) that would be expected under ideal conditions.

The maximum of N_{++} as a function of a (or b) is $\mathrm{Max} = A/2 + C$ and the minimum is $\mathrm{Min} = C$. These values are shown, for instance, in Figs. 3.10(a)-(b), and Fig. 4.7. We obtain that the visibility of the curve of coincidence measurements is a function of the constants A and C for different projections. The visibility is

$$V = \frac{\mathrm{Max} - \mathrm{Min}}{\mathrm{Max} + \mathrm{Min}} = \frac{A}{A + 4C}. \tag{A.13}$$

Under experimental conditions, we would obtain $E(a, b)$ as

$$\begin{aligned} E(a,b) &= \frac{N_{++} + N_{--} - N_{+-} - N_{-+}}{N_{++} + N_{--} + N_{+-} + N_{-+}} \\ &= \frac{[A\cos^2(a-b) + 2C] - \left[A\sin^2(a-b) + 2C\right]}{[A\cos^2(a-b) + 2C] + \left[A\sin^2(a-b) + 2C\right]} \\ &= \frac{A}{A+4C}\cos 2(a-b) = V\cos 2(a-b), \end{aligned} \tag{A.14}$$

for general angles a and b. V is the visibility of Eq. (A.13). If we assume that the visibility is the same for different projections, the new value of S expected in the experiment is thus

$$S = \frac{A}{A+4C}[3\cos 2\theta - \cos 6\theta] = V[3\cos 2\theta - \cos 6\theta], \tag{A.15}$$

For $\theta = 0°$ we obtain $S = 2V$, as can be seen in Fig. 3.10(c) for a particular visibility value of $V = 0.92$. The different theoretical CHSH curves that can be seen in Fig. 4.8 are the predictions considering different values of ϵ, that comes from introducing a different temporal delay between orthogonal photons with the help of the delay line.

APPENDIX

B

PROOFS OF THEOREMS STATED IN CHAPTER 5

Let $\hat{\rho}$ be a general 4 dimensional complex Hermitian matrix, that could represent a 2×2 – dimensional mixed quantum state, or a partially coherent beam describing coherent or incoherent superposition of four modes. In general, $\hat{\rho}$ can be always written as (*spectral decomposition*)

$$\hat{\rho} = V\hat{E}V^{\dagger} = \lambda_1|a\rangle\langle a| + \lambda_2|b\rangle\langle b| + \lambda_3|c\rangle\langle c| + \lambda_4|d\rangle\langle d|, \qquad \text{(B.1)}$$

where the diagonal matrix $\hat{E}$ contains eigenvalues λ_i and the matrix V consists of the corresponding eigenvectors $\{|a\rangle, |b\rangle, |c\rangle, |d\rangle\}$ forming an orthonormal basis. We assume that $\lambda_1 \geq \lambda_2 \geq \lambda_3 \geq \lambda_4$ and $\sum_i \lambda_i = 1$. When a unitary transformation U is applied to the state $\hat{\rho}$, a new state $\hat{\rho}' = U\hat{\rho}U^{\dagger}$ is obtained,

$$\hat{\rho}' = \lambda_1|a'\rangle\langle a'| + \lambda_2|b'\rangle\langle b'| + \lambda_3|c'\rangle\langle c'| + \lambda_4|d'\rangle\langle d'|. \qquad \text{(B.2)}$$

Notice that all states connected by the means of unitary transformations share the same eigenvalues, i.e., the eigenvalues λ_i are invariant under the unitary transformations. However, the eigenvectors change.

Minimal first-order coherence

Theorem:

There exists a unitary transformation U that when applied to $\hat{\rho}$ generates a new state $\hat{\rho}' = U\hat{\rho}U^\dagger$ so that the coherence D vanishes and the violation of the CHSH is maximized with value [105, 122]

$$B_{\max} = 2\sqrt{2}\sqrt{(\lambda_1 - \lambda_4)^2 + (\lambda_2 - \lambda_3)^2}. \tag{B.3}$$

The unitary transformation has the form $U = MV^\dagger$, where

$$M = \frac{1}{\sqrt{2}} \begin{pmatrix} 1 & 1 & 0 & 0 \\ 0 & 0 & 1 & 1 \\ 0 & 0 & 1 & -1 \\ 1 & -1 & 0 & 0 \end{pmatrix}. \tag{B.4}$$

Proof:

First, we need to transform $\hat{\rho}$ to a diagonal form in the computational basis $\{|0\rangle_A|0\rangle_B, |0\rangle_A|1\rangle_B, |1\rangle_A|0\rangle_B, |1\rangle_A|1\rangle_B\}$. This is done with the help of the matrix V that contains the eigenvectors of $\hat{\rho}$, so that

$$\hat{\rho} \to \hat{E} = V^\dagger \hat{\rho} V. \tag{B.5}$$

From [122], it can be shown that the violation of the CHSH inequality is maximized for a Bell diagonal state of the form

$$\begin{aligned} \hat{\rho} = {} & \lambda_1|\Phi^+\rangle\langle\Phi^+| + \lambda_2|\Phi^-\rangle\langle\Phi^-| \\ & + \lambda_3|\Psi^+\rangle\langle\Psi^+| + \lambda_4|\Psi^-\rangle\langle\Psi^-|, \end{aligned} \tag{B.6}$$

where $|\Phi^\pm\rangle$ and $|\Psi^\pm\rangle$ are the maximally entangled Bell states. Any unitary transformation applied on the state given by Eq. (B.6) cannot increase the degree of violation of the inequality.

A general Bell diagonal state in the computational basis writes as

$$\hat{\rho}_{\text{Bell}} = \frac{1}{2} \begin{pmatrix} \lambda_1 + \lambda_2 & 0 & 0 & \lambda_1 - \lambda_2 \\ 0 & \lambda_3 + \lambda_4 & \lambda_3 - \lambda_4 & 0 \\ 0 & \lambda_3 - \lambda_4 & \lambda_3 + \lambda_4 & 0 \\ \lambda_1 - \lambda_2 & 0 & 0 & \lambda_1 + \lambda_2 \end{pmatrix}. \tag{B.7}$$

The matrix M performs the transformation [135]

$$\{|00\rangle, |01\rangle, |10\rangle, |11\rangle\} \Longrightarrow \left\{|\Phi^+\rangle, |\Phi^-\rangle, |\Psi^+\rangle, |\Psi^-\rangle\right\} \tag{B.8}$$

that can be easily demonstrated by direct inspection. After combining both transformations, now we have

$$\hat{\rho} \Longrightarrow \hat{\rho}' = M\hat{E}M^\dagger = MV^\dagger\hat{\rho}VM^\dagger. \tag{B.9}$$

The unitary transformation $U = MV^\dagger$ generates the state given in Eq. (B.6). From here, one can use the Horodecki's approach [105] to get Eq. (B.3) [122].

The coherence (D) for the state of the form given in Eq. (B.7) is

$$D_A^2 = 2\text{tr}\left[\frac{1}{4}\begin{pmatrix} \sum_{i=1}^4 \lambda_i & 0 \\ 0 & \sum_{i=1}^4 \lambda_i \end{pmatrix}^2\right] - 1 = 0. \tag{B.10}$$

Similarly, we obtain $D_B^2 = 0$. That leads to $D^2 = (D_A^2 + D_B^2)/2 = 0$.

By means of a unitary transformation, we can generate a new state where both subsystems show no coherence $D = 0$. It corresponds to the state that shows the maximal violation of the CHSH inequality achievable for states connected through the unitary transformations.

Maximal first-order coherence

Theorem:

There exists a unitary transformation U that when applied to an arbitrary state $\hat{\rho}$ generates a new state $\hat{\rho}' = U\hat{\rho}U^\dagger$ that maximizes the coherence D with value

$$D_{\max}^2 = (\lambda_1 - \lambda_4)^2 + (\lambda_2 - \lambda_3)^2 \tag{B.11}$$

and yields a violation of CHSH that is minimal, with value

$$B_{\max} = 2\left|\lambda_1 - \lambda_2 - \lambda_3 + \lambda_4\right|. \tag{B.12}$$

The unitary transformation U has the form $U = V^\dagger$.

Proof:

The unitary transformation $U = V^\dagger$ transforms an arbitrary state $\hat{\rho}$ into the state $\hat{E}$ that is diagonal in the following computational basis $\{|0\rangle_A|0\rangle_B, |0\rangle_A|1\rangle_B, |1\rangle_A|0\rangle_B, |1\rangle_A|1\rangle_B, \}$, so it performs the transformation

$$\{|a\rangle, |b\rangle, |c\rangle, |d\rangle\} \Longrightarrow \{|0\rangle_A|0\rangle_B, |0\rangle_A|1\rangle_B, |1\rangle_A|0\rangle_B, |1\rangle_A|1\rangle_B\}\,. \quad \text{(B.13)}$$

Therefore

$$\hat{\rho} \Longrightarrow \hat{\rho}' = V^\dagger \hat{\rho} V. \quad \text{(B.14)}$$

One can see by performing extensive numerical simulations that the degree of coherence D cannot be increased by applying additional unitary transformations W on $\hat{E}$.

Moreover, when considering the Jarlskog recursive parametrization [125] of an arbitrary unitary transformation $W(\vec{\alpha})$ with parameter $\vec{\alpha}$, we can demonstrate that the function that gives the degree of coherence after the unitary transformation, $D[W(\vec{\alpha})\hat{E}W^\dagger(\vec{\alpha})]$ has a maximum for $\vec{\alpha} = 0$, which corresponds to the identity transformation, since

$$\left.\frac{\partial D\left[W(\vec{\alpha})\hat{E}W^\dagger(\vec{\alpha})\right]}{\partial \vec{\alpha}}\right|_{\vec{\alpha}=\vec{0}} = 0. \quad \text{(B.15)}$$

Direct calculation of the Hessian matrix of second derivatives confirms that the state $\hat{E}$ has the maximal degree of coherence D. In this proof, alternating signs of the determinants of leading sub-matrices with the increasing rank have been obtained.

The degree of coherence D of the state $\hat{E}$ with diagonal elements λ_i is easily obtained to be

$$D^2_{\max} = \frac{D_A^2 + D_B^2}{2} = (\lambda_1 - \lambda_4)^2 + (\lambda_2 - \lambda_3)^2\,. \quad \text{(B.16)}$$

For the state $\hat{E}$, the only non-vanishing element of the matrix T_ρ

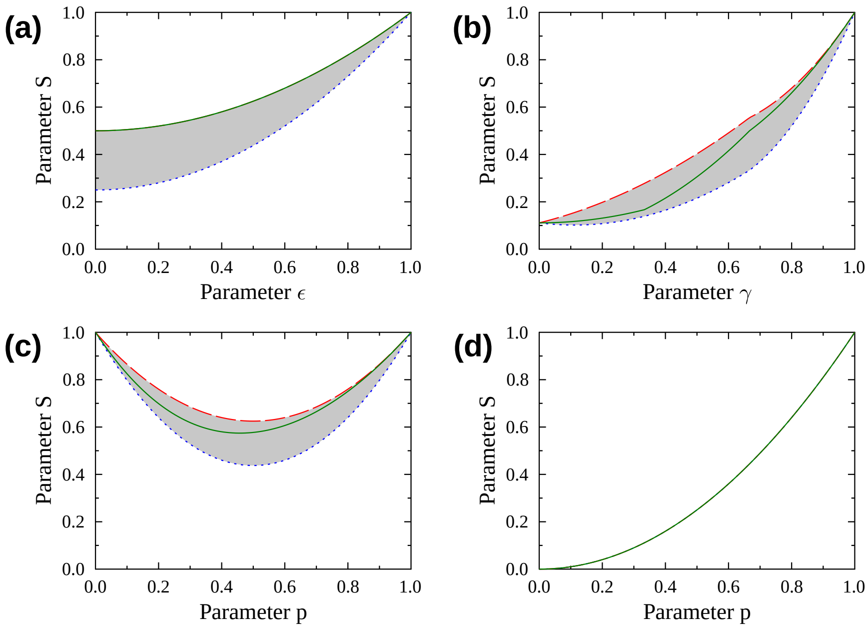

Figure B.1: Maximum and minimum values of S for examples I-IV. (a) MNMS state, (b) MEMS state, (c) example C in [33] and (d) Werner state. The green line depicts the original value, prior to any unitary transformation. The dashed-red line depicts S_{max}, and the dotted-blued line depicts S_{min}. Grey areas mark all possible values of S.

is t_{33}, that reads

$$T_{\hat{E}} = \begin{pmatrix} 0 & 0 & 0 \\ 0 & 0 & 0 \\ 0 & 0 & \lambda_1 - \lambda_2 - \lambda_3 + \lambda_4 \end{pmatrix}. \tag{B.17}$$

The value of B_{max} is $B_{\text{max}} = 2\sqrt{\mu}$, where $\mu = (\lambda_1 - \lambda_2 - \lambda_3 + \lambda_4)^2$ is the only non-zero eigenvalue of $T_{\hat{E}}^T T_{\hat{E}}$. In this case

$$B_{\text{max}} = 2|\lambda_1 - \lambda_2 - \lambda_3 + \lambda_4|. \tag{B.18}$$

General invariant involving coherence

One can be tempted to look for an expression similar to the one defined in [33] and define a parameter S as

$$S = \frac{D_A^2 + D_B^2}{4} + \left(\frac{B_{\max}}{2\sqrt{2}}\right)^2. \tag{B.19}$$

For certain states, it can be found that this parameter is indeed constant under unitary transformations. This is the case of the Werner state (example IV in Chapter 5), as it is demonstrated below and can be observed in Fig. B.1(d). However, in general, this is not the case. Examples I-III of Chapter 5 correspond to this situation, as it can be seen in Figs. B.1(a) to B.1(c), that show all possible values of S (grey areas) obtained by unitary transformations.

It can be easily shown using Eqs. (5.1) to (5.4), that all values of S are between upper and lower boundaries: $S_{\max} = P - 2(\lambda_1\lambda_4 + \lambda_2\lambda_3)$ and $S_{\min} = P - (\lambda_1 + \lambda_4)(\lambda_2 + \lambda_3)$, where $\mathcal{P}$ stands for the purity of the state. $S_{\max}$ corresponds to the maximal violation of the CHSH inequality and the minimal first-order coherence, whereas $S_{\min}$ corresponds to the minimal violation of the CHSH inequality and the maximal first-order coherence.

For a general mixed state ($\mathrm{tr}\hat{\rho}^2 \leq 1$), one can derive [105]

$$\frac{D_A^2 + D_B^2}{4} + \mathcal{T} = \mathrm{tr}\hat{\rho}^2, \tag{B.20}$$

where $\mathcal{T} = 1/4\,(1 + \sum_{i,j=1}^{3} t_{ij}^2)$, $t_{ij} = \mathrm{tr}\,[\hat{\rho}\hat{\sigma}_i \otimes \hat{\sigma}_j]$ and $\sigma_{i,j}$ $(i,j = 1,2,3)$ are the Pauli matrices. The values of t_{ij} can be only obtained by making coincidence measurements between the subsystems, therefore measuring the nature of their correlations. Any increase/decrease of the degree of coherence is accompanied by a corresponding decrease/increase of $\mathcal{T}$. For a pure state, $D_A = D_B$ and $\mathcal{T} = (B_{\max}/2\sqrt{2})^2$ (see below), so one obtains

$$\frac{D_{A,B}^2}{2} + \left(\frac{B_{\max}}{2\sqrt{2}}\right)^2 = 1. \tag{B.21}$$

Pure states: Derivation of Eq. (B.21)

Any pure state can be written as a Schmidt decomposition that reads [64]

$$|\Psi\rangle = \kappa_1|x_1\rangle_A|y_1\rangle_B + \kappa_2|x_2\rangle_A|y_2\rangle_B, \tag{B.22}$$

where $\kappa_1^2+\kappa_2^2 = 1$, $\{|x_1\rangle_A, |x_2\rangle_A\}$ is an orthonormal basis in subsystem A and $\{|y_1\rangle_B, |y_2\rangle_B\}$ is an orthonormal basis in subsystem B. For the sake of simplicity we assume $\kappa_{1,2}$ to be real. Following [136], one obtains that

$$\sum_{i,j=1}^{3} t_{ij}^2 = 1 + 8\kappa_1^2\kappa_2^2, \tag{B.23}$$

$$B_{\max} = 2\sqrt{1 + 4\kappa_1^2\kappa_2^2}. \tag{B.24}$$

Therefore

$$\begin{aligned} \mathcal{T} &= \frac{1+\sum_{i,j=1}^{3} t_{ij}^2}{4} = \frac{1+4\kappa_1^2\kappa_2^2}{2} \\ &= \frac{1}{2}\left[1 + \left(\frac{B_{\max}^2}{4} - 1\right)\right] = \left(\frac{B_{\max}}{2\sqrt{2}}\right)^2. \end{aligned} \tag{B.25}$$

Substitution of Eq. (B.25) into Eq. (B.20) yields straightforwardly Eq. (B.21).

Werner state: Invariance of the parameter S under global unitary transformations

The Werner state (example IV of Chapter 5) can be written as [137]

$$\hat{\rho}_W = \frac{1-p}{4} I_4 + p|\Phi^+\rangle\langle\Phi^+|, \tag{B.26}$$

where $|\Phi^+\rangle = 1/\sqrt{2}\,(|0\rangle_A|0\rangle_B + |1\rangle_A|1\rangle_B)$ is the maximally entangled Bell state. The Werner state can be generalized considering the state $|\Psi\rangle$ given by Eq. (B.22) instead of $|\Phi^+\rangle$. The spectral decomposition of the generalized state can be written as

$$\begin{aligned}\hat{\rho}_W = \frac{1+3p}{4}|\Psi\rangle\langle\Psi| + \frac{1-p}{4}|\Psi^\perp\rangle\langle\Psi^\perp| \\ +\frac{1-p}{4}\left\{|x_1\rangle_A|y_2\rangle_B\langle x_1|_A\langle y_2|_B + |x_2\rangle_A|y_1\rangle_B\langle x_2|_A\langle y_1|_B\right\},\end{aligned} \quad \text{(B.27)}$$

where $|\Psi^\perp\rangle = -\kappa_2|x_1\rangle_A|y_1\rangle_B + \kappa_1|x_2\rangle_A|y_2\rangle_B$. The corresponding matrix T_ρ writes

$$T_\rho = \begin{pmatrix} 2p\kappa_1\kappa_2 & 0 & 0 \\ 0 & -2p\kappa_1\kappa_2 & 0 \\ 0 & 0 & p \end{pmatrix}. \quad \text{(B.28)}$$

The maximal violation of the CHSH inequality writes

$$B_{\max} = 2p\sqrt{1+4\kappa_1^2\kappa_2^2}, \quad \text{(B.29)}$$

and

$$\mathcal{T} = \frac{1+p^2+8p^2\kappa_1^2\kappa_2^2}{4}. \quad \text{(B.30)}$$

Substituting Eq. (B.30) into Eq. (B.20), and making use of Eq. (B.29), one obtains that

$$\frac{D^2}{2} + \left(\frac{B_{\max}}{2\sqrt{2}}\right)^2 = p^2. \quad \text{(B.31)}$$

For $p = 1$ (pure state) we recover Eq. (B.21).

APPENDIX

C

CALCULATION OF COHERENCE IN INDUCED OPTICAL COHERENCE TOMOGRAPHY

C.1 Input-output relationship in parametric down-conversion

Note: we acknowledge the contribution of A. Barja in the calculations of this Appendix C, during his summer fellowship under the supervision of J. P. Torres.

Let $\hat{b}_s(\omega)$ and $\hat{b}_i(\omega)$ designate the operators corresponding to the signal and idler modes, respectively, at the input face of the nonlinear crystal. Let $\hat{a}_s(\omega)$ and $\hat{a}_i(\omega)$ designate the operators corresponding to the same modes at the output face of the nonlinear crystal after the interaction of the input waves with the molecules of the crystal. Under the condition that the pump beam is undepleted, and the efficiency of the parametric process is low, the relationship between input and output modes is a Bogoliuvov transformation that reads as [68]

$$\begin{aligned}\hat{a}_s(\omega_1) &= \int d\omega_3 \left[C_s(\omega_1,\omega_3)\hat{b}_s(\omega_3) + S_s(\omega_1,\omega_3)\hat{b}_i^{\dagger}(\omega_3) \right], \\ \hat{a}_i(\omega_2) &= \int d\omega_3 \left[C_i(\omega_2,\omega_3)\hat{b}_i(\omega_3) + S_i(\omega_1,\omega_3)\hat{b}_s^{\dagger}(\omega_3) \right], \end{aligned} \tag{C.1}$$

where

$$\begin{aligned} C_s(\omega_1,\omega_2) &= \delta(\omega_1-\omega_2)\exp\left[ik_s(\omega_1)\right], \\ S_s(\omega_1,\omega_2) &= \sigma L F_p(\omega_1+\omega_2)\exp\left\{\frac{i}{2}\left[k_p(\omega_1+\omega_2)+k_s(\omega_1)-k_i(\omega_2)\right]\right\} \\ &\quad \times \mathrm{sinc}\left\{\frac{L}{2}\left[k_p(\omega_1+\omega_3)-k_s(\omega_1)-k_i(\omega_2)\right]\right\}, \\ C_i(\omega_1,\omega_2) &= \delta(\omega_1-\omega_2)\exp\left[ik_i(\omega_1)\right], \\ S_i(\omega_1,\omega_2) &= \sigma L F_p(\omega_1+\omega_2)\exp\left\{\frac{i}{2}\left[k_p(\omega_1+\omega_2)+k_i(\omega_1)-k_s(\omega_2)\right]\right\} \\ &\quad \times \mathrm{sinc}\left\{\frac{L}{2}\left[k_p(\omega_1+\omega_2)-k_s(\omega_1)-k_i(\omega_2)\right]\right\}, \end{aligned} \tag{C.2}$$

σ is the nonlinear coefficient of the parametric down-conversion process and L is the length is the nonlinear crystal. The wavenumbers of the signal, idler and pump waves inside the nonlinear crystal read as $k_s(\omega) = \omega n_s/c$, $k_i(\omega) = \omega n_i/c$ and $k_p(\omega) = \omega n_p/c$. $n_{s,i,p}$ designate the corresponding refractive index for each wave. F_p is the normalized frequency shape of the pump beam, i.e., $\int d\omega |F_p(\omega)|^2 = 1$. We approximate the shape of the pump beam with a Gaussian function, so we can write

$$F_p(\omega_p) = \frac{1}{(\pi B_p)^{1/4}} \exp\left[-\frac{1}{2}\frac{(\omega_p-\omega_p^0)^2}{B_p^2}\right], \tag{C.3}$$

where B_p is the bandwidth of the pump beam.

C.2 Calculation of the first-order coherence function between signal photons

We want to calculate the normalized first-order coherence function ($g^{(1)}$) between signal photons (what we call coherence in this thesis), that read as

$$g^{(1)} = \frac{\int d\omega \langle a_2^\dagger(\omega) d_2(\omega)\rangle}{\sqrt{\int d\omega \langle a_2^\dagger(\omega) a_2(\omega)\rangle}\sqrt{\int d\omega \langle d_2^\dagger(\omega) d_2(\omega)\rangle}}. \tag{C.4}$$

Following the operators indicated in Fig. C.1, we can write

$$\begin{aligned}
a_2(\omega_1) &= \exp\left[i\frac{\omega_1}{c}z_1\right]\left\{\int d\omega_0 \left[C_s(\omega_1,\omega_0)a_1(\omega_0) + S_s(\omega_1,\omega_0)b_1^\dagger(\omega_0)\right]\right\}, \\
b_2(\omega_2) &= \exp\left[i\frac{\omega_2}{c}z_2\right]\left\{\int d\omega_0 \left[C_i(\omega_2,\omega_0)b_1(\omega_0) + S_i(\omega_2,\omega_0)a_1^\dagger(\omega_0)\right]\right\}, \\
e_1(\omega_2) &= \exp\left[i\frac{\omega_2}{c}z_3\right]\left[\tau b_2(\omega_2) + f(\omega_2)\right], \\
d_2(\omega_3) &= \int d\omega_2 C_s(\omega_3,\omega_2) d_1(\omega_2)\exp\left[i\frac{\omega_3}{c}z_4\right] \qquad (C.5) \\
&+ \int d\omega_2 S_s(\omega_3,\omega_2) f^\dagger(\omega_2)\exp\left[-i\frac{\omega_2}{c}z_3 + i\frac{\omega_3}{c}z_4\right] \\
&+\tau^* \int d\omega_2 d\omega_0 S_s(\omega_3,\omega_2) C_s^*(\omega_2,\omega_0) b_1^\dagger(\omega_0)\exp\left[-i\frac{\omega_2}{c}(z_2+z_3) + i\frac{\omega_3}{c}z_4\right] \\
&+\tau^* \int d\omega_2 d\omega_0 S_s(\omega_3,\omega_2) S_s^*(\omega_2,\omega_0) a_1(\omega_0)\exp\left[-i\frac{\omega_2}{c}(z_2+z_3) + i\frac{\omega_3}{c}z_4\right].
\end{aligned}$$

The operator f, associated with the presence of loss in the sample, fulfils the commutation relationship

$$\left[f(\omega_1), f^\dagger(\omega_2)\right] = \delta(\omega_1 - \omega_2)(1 - |\tau|^2). \tag{C.6}$$

We have:

- $$\int d\omega \langle a_2^\dagger(\omega) a_2(\omega)\rangle = \int d\omega_1 d\omega_2 |S_s(\omega_1,\omega_2)|^2 = N, \tag{C.7}$$

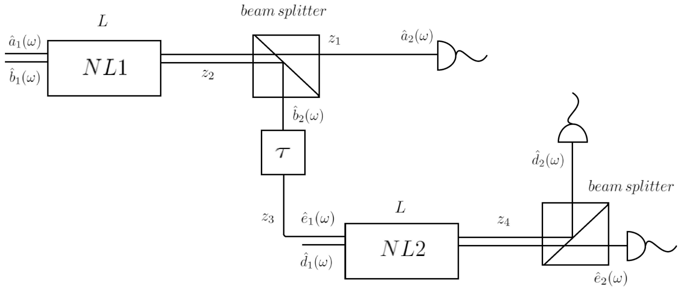

Figure C.1: Simple scheme of the iOCT sources to indicate each of the operators used in the calculations.

being N the number of signal photons that are generated in the first nonlinear crystal.

- $$\int d\omega\langle d_2^\dagger(\omega)d_2(\omega)\rangle = (1-|\tau|^2)\int d\omega_1 d\omega_2 |S_s(\omega_1,\omega_2)|^2 + |\tau|^2 \int d\omega_1 d\omega_1' d\omega_2 d\omega_2' S_s^*(\omega_1,\omega_2')S_s(\omega_1,\omega_2)C(\omega_2',\omega_1')C^*(\omega_2,\omega_1') = (1-|\tau|^2)N + |\tau|^2 N = N, \tag{C.8}$$

- $$\int d\omega\langle a_2^\dagger(\omega)d_2(\omega)\rangle \tag{C.9}$$
$$= \tau^* \int d\omega_1 d\omega_2 |S(\omega_1,\omega_2)|^2 \exp\left[-ik_i(\omega_2)L - i\frac{\omega_2}{c}(z_2+z_3) - i\frac{\omega_1}{c}(z_1-z_4)\right].$$

Making use of all of these expressions, we finally obtain that the normalized first-order coherence functions (*the coherence*) is

$$|g^{(1)}| = |\tau| \frac{\int d\omega_1 d\omega_2 |S_s(\omega_1,\omega_2)|^2 \exp\left[-ik_i(\omega_1)L - i\frac{\omega_2}{c}(z_2+z_3) - i\frac{\omega_1}{c}(z_1-z_4)\right]}{\int d\omega_1 d\omega_2 |S(\omega_1,\omega_2)|^2}. \tag{C.10}$$

C.3 Some analytical results

We can get some analytic results integrating explicitly the formulas. We can approximate the wavenumbers to first order in the frequency as

$$\begin{aligned} k_p(\omega) &= k_p^0 + N_p(\omega_p - \omega_p^0), \\ k_s(\omega) &= k_s^0 + N_s(\omega_s - \omega_s^0), \\ k_s(\omega) &= k_i^0 + N_i(\omega_i - \omega_i^0), \end{aligned} \tag{C.11}$$

where ω_j^0 $(j = s, i, p)$ are the central frequencies, k_j^0 are the wavenumbers at the corresponding central frequencies and N_j are the inverse group velocities. For the sake on convenience, we define the parameters

$$\begin{aligned} D_+ &= N_p - \frac{N_s + N_i}{2}, \\ D &= N_s - N_i. \end{aligned} \tag{C.12}$$

The number of photons N is

$$\begin{aligned} N &= \int d\omega_1 d\omega_2 |S(\omega_1, \omega_2)|^2 \\ &= \frac{\sigma^2 L^2}{\sqrt{\pi B_p^2}} \int d\omega_1 d\omega_2 \exp\left[-\frac{(\omega_1+\omega_2)^2}{B_p^2}\right] \\ &\times \text{sinc}^2 \left\{ \frac{L}{2} \left[D_+(\omega_1+\omega_2) + \frac{D}{2}(\omega_1 - \omega_2) \right] \right\}. \end{aligned} \tag{C.13}$$

We perform a change of variables

$$\begin{aligned} \omega_p &= \omega_1 + \omega_2, \\ \omega &= \frac{L}{2}(D_+(\omega_1+\omega_2) + \frac{D}{2}(\omega_1 - \omega_2)), \end{aligned} \tag{C.14}$$

so that we obtain

$$N = \frac{2\sigma^2 L}{|D|\sqrt{\pi B_p^2}} \int d\omega d\omega_p \exp\left[-\frac{\omega_p^2}{B_p^2}\right] \mathrm{sinc}^2(\omega)$$
$$= \frac{2\sigma^2 L}{|D|\sqrt{\pi B_p^2}} \int d\omega_p \exp\left[-\frac{\omega_p^2}{B_p^2}\right] \int d\omega sinc^2(\omega) = \frac{2\sigma^2 L\pi}{|D|}. \quad \text{(C.15)}$$

Now, let us compute $\left|\int d\omega \langle a_2^\dagger(\omega) d_2(\omega)\rangle\right|$. We have

$$\left|\int d\omega \langle a_2^\dagger(\omega) d_2(\omega)\rangle\right| = |\tau| \frac{\sigma^2 L^2}{\sqrt{\pi B_p^2}} \int d\omega_1 d\omega_2 \exp\left[-\frac{(\omega_1+\omega_2)^2}{B_p^2}\right]$$
$$\times \mathrm{sinc}^2\left(\frac{L}{2}(D_+(\omega_1+\omega_2) + \frac{D}{2}(\omega_1-\omega_2))\right) \exp\left[-i\omega_2 \frac{z}{c} - i\omega_1 \frac{x}{c}\right], \quad \text{(C.16)}$$

where $z = N_i Lc + z_2 + z_3$ and $x = z_1 - z_4$. By doing the same change of variables as before, we can write

$$\left|\int d\omega \langle a_2^\dagger(\omega) d_2(\omega)\rangle\right| = \frac{2\sigma^2 L|\tau|}{|D|\sqrt{\pi B_p^2}}$$
$$\times \int d\omega_p d\omega \mathrm{sinc}^2(\omega) \exp\left[-\frac{\omega_p^2}{B_p^2} - i\alpha\omega_p - i\beta\omega\right], \quad \text{(C.17)}$$

with

$$\alpha = \frac{z}{c}\left(\frac{1}{2} + \frac{D_+}{D}\right) + \frac{x}{c}\left(\frac{1}{2} - \frac{D_+}{D}\right),$$
$$\beta = \frac{2}{LDc}(x - z). \quad \text{(C.18)}$$

Since these integrals are the Fourier transforms of a Gaussian functions and a sinc squared function, we can integrate them analytically to obtain

$$|g^{(1)}| = |\tau| \exp\left\{-\frac{B_p^2}{4c^2}\left[z\left(\frac{1}{2} + \frac{D_+}{D}\right) + x\left(\frac{1}{2} - \frac{D_+}{D}\right)\right]^2\right\}$$
$$\times \Lambda\left[\frac{1}{LDc}(x - z)\right], \quad \text{(C.19)}$$

where Λ is the triangular function.

We are interested in the case of a narrowband pump beam ($B_p \sim 0$). In this case,

$$|g^{(1)}| = |\tau|\Lambda\left[\frac{1}{LDc}(x-z)\right]. \tag{C.20}$$

This expression describes the result shown in Fig. 6.9(a), where one can see the triangular shape of the coherence function.

LIST OF PUBLICATIONS

The work presented in this thesis is based in the following publications:

- A. Vallés, M. Hendrych, J. Svozilík, R. Machulka, P. Abolghasem, D. Kang, B. J. Bijlani, A. S. Helmy, and J. P. Torres, "Generation of polarization-entangled photon pairs in a Bragg reflection waveguide," *Opt. Express*, **21**, 10841, (2013).
- A. Vallés, V. D'Ambrosio, M. Hendrych, M. Mičuda, L. Marrucci, F. Sciarrino, and J. P. Torres,"Generation of tunable entanglement and violation of a Bell-like inequality between different degrees of freedom of a single photon," *Phys. Rev. A*, **90**, 052326, (2014).
- R. de J. León-Montiel, A. Vallés, H. M. Moya-Cessa and J. P. Torres, "Coherent delocalization: views of entanglement in different scenarios," *Laser Phys. Lett.*, **12**, 085204, (2015).
- J. Svozilík, A. Vallés, J. Peřina Jr., and J. P. Torres, "Revealing hidden coherence in partially coherent light," *Phys. Rev. Lett.*, **115**, 220501, (2015).
- A. Vallés, G. Jiménez, A. Barja, L. J. Salazar-Serrano, and J. P. Torres, "Induced optical coherence tomography," *In preparation*, (2017).

BIBLIOGRAPHY

[1] E. Schrödinger, "Die gegenwärtige Situation in der Quantenmechanik," *Naturwissenschaften*, vol. 23, p. 807, 1935.

[2] A. Einstein, B. Podolsky, and N. Rosen, "Can Quantum-Mechanical Description of Physical Reality be Considered Complete?," *Phys. Rev.*, vol. 47, p. 777, 1935.

[3] N. Bohr, "Can Quantum-Mechanical Description of Physical Reality be Considered Complete?," *Phys. Rev.*, vol. 48, p. 696, 1935.

[4] J. S. Bell, "On the Einstein Podolsky Rosen Paradox," *Physics (Long Island City, N.Y.)*, vol. 1, p. 195, 1964.

[5] J. F. Clauser, M. A. Horne, A. Shimony, and R. A. Holt, "Proposed Experiment to Test Local Hidden-Variable Theories," *Phys. Rev. Lett.*, vol. 23, p. 880, 1969.

[6] A. Aspect, P. Grangier, and G. Roger, "Experimental Tests of Realistic Local Theories via Bell's Theorem," *Phys. Rev. Lett.*, vol. 47, p. 460, 1981.

[7] A. Aspect, J. Dalibard, and G. Roger, "Experimental Test of Bell's Inequalities Using Time-Varying Analyzers," *Phys. Rev. Lett.*, vol. 49, p. 1804, 1982.

[8] G. Weihs, T. Jennewein, C. Simon, H. Weinfurter, and A. Zeilinger, "Violation of Bell's Inequality under Strict Einstein Locality Conditions," *Phys. Rev. Lett.*, vol. 81, p. 5039, 1998.

[9] R. Horodecki, P. Horodecki, M. Horodecki, and K. Horodecki, "Quantum entanglement," *Rev. Mod. Phys.*, vol. 81, p. 865, 2009.

[10] J. C. Howell, R. S. Bennink, S. J. Bentley, and R. W. Boyd, "Realization of the Einstein-Podolsky-Rosen Paradox Using Momentum- and Position-Entangled Photons from Spontaneous Parametric Down Conversion," *Phys. Rev. Lett.*, vol. 92, p. 210403, 2004.

[11] I. Žutić, J. Fabian, and S. D. Sarma, "Spintronics: Fundamentals and applications," *Rev. Mod. Phys.*, vol. 76, p. 323, 2004.

[12] B. Hensen, H. Bernien, A. E. Dréau, A. Reiserer, N. Kalb, M. S. Blok, J. Ruitenberg, R. F. L. Vermeulen, R. N. Schouten, C. Abellán, W. Amaya, V. Pruneri, M. W. Mitchell, M. Markham, D. J. Twitchen, D. Elkouss, S. Wehner, T. H. Taminiau, and R. Hanson, "Loophole-free Bell inequality violation using electron spins separated by 1.3 kilometres," *Nature*, vol. 526, p. 682, 2015.

[13] W. K. Wootters, "Entanglement of Formation of an Arbitrary State of Two Qubits," *Phys. Rev. Lett.*, vol. 80, p. 2245, 1998.

[14] E. M. Rains, "Rigorous treatment of distillable entanglement," *Phys. Rev. A*, vol. 60, p. 173, 1999.

[15] V. Vedral, M. B. Plenio, M. A. Rippin, and P. L. Knight, "Quantifying Entanglement," *Phys. Rev. Lett.*, vol. 78, p. 2275, 1997.

[16] M. Christandl and A. Winter, "Squashed entanglement: An additive entanglement measure," *J. Math. Phys.*, vol. 45, p. 829, 2004.

[17] E. Hagley, X. Maître, G. Nogues, C. Wunderlich, M. Brune, J. M. Raimond, and S. Haroche, "Generation of Einstein-Podolsky-Rosen Pairs of Atoms," *Phys. Rev. Lett.*, vol. 79, p. 1, 1997.

[18] M. Lamehi-Rachti and W. Mittig, "Quantum mechanics and hidden variables: A test of Bell's inequality by the measurement of the spin correlation in low-energy proton-proton scattering," *Phys. Rev. D*, vol. 14, p. 2543, 1976.

[19] Q. A. Turchette, C. S. Wood, B. E. King, C. J. Myatt, D. Leibfried, W. M. Itano, C. Monroe, and D. J. Wineland, "Deterministic Entanglement of Two Trapped Ions," *Phys. Rev. Lett.*, vol. 81, p. 3631, 1998.

[20] M. Steffen, M. Ansmann, R. McDermott, N. Katz, R. C. Bialczak, E. Lucero, M. Neeley, E. M. Weig, A. N. Cleland, and J. M. Martinis, "State Tomography of Capacitively Shunted Phase Qubits with High Fidelity," *Phys. Rev. Lett.*, vol. 97, p. 050502, 2006.

[21] B. Julsgaard, A. Kozhekin, and E. S. Polzik, "Experimental long-lived entanglement of two macroscopic objects," *Nature*, vol. 413, p. 400, 2001.

[22] K. C. Lee, M. R. Sprague, B. J. Sussman, J. Nunn, N. K. Langford, X.-M. Jin, T. Champion, P. Michelberger, K. F. Reim, D. England, D. Jaksch, and I. A. Walmsley, "Entangling Macroscopic Diamonds at Room Temperature," *Science*, vol. 334, p. 1253, 2011.

[23] V. G. Dmitriev, G. G. Gurzadyan, and D. N. Nikogosyan, "Handbook of Nonlinear Optical Crystals," *(Springer, Berlin)*, 1997.

[24] N. Gisin, "Hidden quantum nonlocality revealed by local filters," *Phys. Lett. A*, vol. 210, p. 151, 1996.

[25] C. K. Hong, Z. Y. Ou, and L. Mandel, "Measurement of Subpicosecond Time Intervals between Two Photons by Interference," *Phys. Rev. Lett.*, vol. 59, p. 2044, 1987.

[26] R. Lopes, A. Imanaliev, A. Aspect, M. Cheneau, D. Boiron, and C. I. Westbrook, "Atomic Hong-Ou-Mandel experiment," *Nature*, vol. 520, p. 66, 2015.

[27] B. S. Cirel'son, "Quantum generalizations of Bell's inequality," *Lett. Math. Phys.*, vol. 4, p. 93, 1980.

[28] R. F. Werner, "Quantum states with Einstein-Podolsky-Rosen correlations admitting a hidden-variable model," *Phys. Rev. A*, vol. 40, p. 4277, 1989.

[29] A. K. Ekert, "Quantum cryptography based on Bell's theorem," *Phys. Rev. Lett.*, vol. 67, p. 661, 1991.

[30] R. J. C. Spreeuw, "A Classical Analogy of Entanglement," *Found. Phys.*, vol. 28, p. 361, 1998.

[31] B. R. Gadway, E. J. Galvez, and F. De Zela, "Bell-inequality violations with single photons entangled in momentum and polarization," *J. Phys. B: At. Mol. Opt. Phys.*, vol. 42, p. 015503, 2009.

[32] C. V. S. Borges, M. Hor-Meyll, J. A. O. Huguenin, and A. Z. Khoury, "Bell-like inequality for the spin-orbit separability of a laser beam," *Phys. Rev. A*, vol. 82, p. 033833, 2010.

[33] K. H. Kagalwala, G. D. Giuseppe, A. F. Abouraddy, and B. E. A. Saleh, "Bell's measure in classical optical coherence," *Nature Photonics*, vol. 7, p. 72, 2013.

[34] J. Svozilík, A. Vallés, J. Peřina Jr., and J. P. Torres, "Revealing Hidden Coherence in Partially Coherent Light," *Phys. Rev. Lett.*, vol. 115, p. 220501, 2015.

[35] A. Luis, "Coherence, polarization, and entanglement for classical light fields," *Opt. Commun.*, vol. 282, p. 3665, 2009.

[36] B. N. Simon, S. Simon, F. Gori, M. Santarsiero, R. Borghi, N. Mukunda, and R. Simon, "Nonquantum Entanglement Resolves a Basic Issue in Polarization Optics," *Phys. Rev. Lett.*, vol. 104, p. 023901, 2010.

[37] X.-F. Qian and J. H. Eberly, "Entanglement and classical polarization states," *Opt. Lett.*, vol. 36, p. 4110, 2011.

[38] P. Ghose and A. Mukherjee, "Entanglement in Classical Optics," *Rev. Theor. Sci.*, vol. 2, p. 274, 2014.

[39] F. Töppel, A. Aiello, C. Marquardt, E. Giacobino, and G. Leuchs, "Classical entanglement in polarization metrology," *New J. Phys.*, vol. 16, p. 073019, 2014.

[40] A. Aiello, F. Töppel, C. Marquardt, E. Giacobino, and G. Leuchs, "Quantum-like nonseparable structures in optical beams," *New J. Phys.*, vol. 17, p. 043024, 2015.

[41] R. J. Glauber, "The Quantum Theory of Optical Coherence," *Phys. Rev.*, vol. 130, p. 2529, 1963.

[42] U. M. Titulaer and R. J. Glauber, "Density Operators for Coherent Fields," *Phys. Rev.*, vol. 145, p. 1041, 1966.

[43] C. Smyth, F. Fassioli, and G. D. Scholes, "Measures and implications of electronic coherence in photosynthetic light-harvesting," *J. Phil. Trans. R. Soc. A*, vol. 370, p. 3728, 2012.

[44] M. Sarovar, A. Ishizaki, G. R. Fleming, and K. B. Whaley, "Quantum entanglement in photosynthetic light-harvesting complexes," *Nat. Phys.*, vol. 6, p. 462, 2010.

[45] F. Caruso, A. W. Chin, A. Datta, S. F. Huelga, and M. B. Plenio, "Entanglement and entangling power of the dynamics in light-harvesting complexes," *Phys. Rev. A*, vol. 81, p. 062346, 2010.

[46] F. Fassioli and A. Olaya-Castro, "Distribution of entanglement in light-harvesting complexes and their quantum efficiency," *New J. Phys.*, vol. 12, p. 085006, 2010.

[47] A. Ishizaki and G. R. Fleming, "Quantum superpositions in photosynthetic light harvesting: delocalization and entanglement," *New J. Phys.*, vol. 12, p. 055004, 2010.

[48] R. E. Blankenship, "Molecular Mechanisms of Photosynthesis," *(Malden, MA: Blackwell)*, 2002.

[49] P. Ball, "Physics of life: The dawn of quantum biology," *Nature*, vol. 474, p. 272, 2011.

[50] N. Lambert, Y.-N. Chen, Y.-C. Cheng, C.-M. Li, G.-Y. Chen, and F. Nori, "Quantum biology," *Nat. Phys.*, vol. 9, p. 10, 2013.

[51] S. F. Huelga and M. B. Plenio, "Vibrations, quanta and biology," *Contemp. Phys.*, vol. 54, p. 181, 2013.

[52] G. S. Engel, T. R. Calhoun, E. L. Read, T.-K. Ahn, T. Mančal, Y.-C. Cheng, R. E. Blankenship, and G. R. Fleming, "Evidence for wavelike energy transfer through quantum coherence in photosynthetic systems," *Nature*, vol. 446, p. 782, 2007.

[53] G. Panitchayangkoon, D. Hayes, K. A. Fransted, J. R. Caram, E. Harel, J. Wen, R. E. Blankenship, and G. S. Engel, "Long-lived quantum coherence in photosynthetic complexes at physiological temperature," *Proc. Natl. Acad. Sci.*, vol. 107, p. 12766, 2010.

[54] E. Collini, C. Y. Wong, K. E. Wilk, P. M. G. Curmi, P. Brumer, and G. D. Scholes, "Coherently wired light-harvesting in photosynthetic marine algae at ambient temperature," *Nature*, vol. 463, p. 644, 2010.

[55] C. Y. Wong, R. M. Alvey, D. B. Turner, K. E. Wilk, D. A. Bryant, P. M. G. Curmi, R. J. Silbe, and G. D. Scholes, "Electronic coherence lineshapes reveal hidden excitonic correlations in photosynthetic light harvesting," *Nat. Chem.*, vol. 4, p. 396, 2012.

[56] M. Tiersch, S. Popescu, and H. J. Briegel, "A critical view on transport and entanglement in models of photosynthesis," *Phil. Trans. R. Soc. A*, vol. 370, p. 3771, 2012.

[57] W. H. Miller, "Perspective: Quantum or classical coherence?," *J. Chem. Phys.*, vol. 136, p. 210901, 2012.

[58] R. de J. León-Montiel and J. P. Torres, "Highly Efficient Noise-Assisted Energy Transport in Classical Oscillator Systems," *Phys. Rev. Lett.*, vol. 110, p. 218101, 2013.

[59] T. Mančal, "Excitation Energy Transfer in a Classical Analogue of Photosynthetic Antennae," *J. Phys. Chem. B*, vol. 117, p. 11282, 2013.

[60] R. de J. León-Montiel, I. Kassal, and J. P. Torres, "Importance of Excitation and Trapping Conditions in Photosynthetic Environment-Assisted Energy Transport," *J. Phys. Chem. B*, vol. 118, p. 10588, 2014.

[61] L. Mandel and E. Wolf, "Optical Coherence and Quantum Optics," *(Cambridge: Cambridge University Press)*, 1995.

[62] F. Caruso, A. W. Chin, A. Datta, S. F. Huelga, and M. B. Plenio, "Highly efficient energy excitation transfer in light-harvesting complexes: The fundamental role of noise-assisted transport," *J. Chem. Phys.*, vol. 131, p. 105106, 2009.

[63] S. Hill and W. K. Wootters, "Entanglement of a Pair of Quantum Bits," *Phys. Rev. Lett.*, vol. 78, p. 5022, 1997.

[64] A. Peres, "Quantum Theory: Concepts and Methods," *(New York: Kluwer)*, 1998.

[65] F. Levi and F. Mintert, "A quantitative theory of coherent delocalization," *New J. Phys.*, vol. 16, p. 033007, 2014.

[66] D. Bouwmeester, A. K. Ekert, and A. Zeilinger, "The Physics of Quantum Information," *(Berlin: Springer)*, 2000.

[67] A. Vallés, M. Hendrych, J. Svozilík, R. Machulka, P. Abolghasem, D. Kang, B. J. Bijlani, A. S. Helmy, and J. P. Torres, "Generation of polarization-entangled photon pairs in a Bragg reflection waveguide," *Opt. Express*, vol. 21, p. 10841, 2013.

[68] J. P. Torres, K. Banaszek, and I. A. Walmsley, "Engineering Nonlinear Optic Sources of Photonic Entanglement," *Prog. Optics*, vol. 56, p. 227, 2011.

[69] M. Hendrych, R. Gallego, M. Mičuda, N. Brunner, A. Acín, and J. P. Torres, "Experimental estimation of the dimension of classical and quantum systems," *Nat. Phys.*, vol. 8, p. 588, 2012.

[70] G. Molina-Terriza, J. P. Torres, and L. Torner, "Twisted photons," *Nat. Phys.*, vol. 3, p. 305, 2007.

[71] S. Franke-Arnold, L. Allen, and M. Padgett, "Advances in optical angular momentum," *Laser Photon. Rev.*, vol. 2, p. 299, 2008.

[72] E. Nagali, F. Sciarrino, F. D. Martini, L. Marrucci, B. Piccirillo, E. Karimi, and E. Santamato, "Quantum Information Transfer from Spin to Orbital Angular Momentum of Photons," *Phys. Rev. Lett.*, vol. 103, p. 013601, 2009.

[73] A. Vallés, V. D'Ambrosio, M. Hendrych, M. Mičuda, L. Marrucci, F. Sciarrino, and J. P. Torres, "Generation of tunable entanglement and violation of a Bell-like inequality between different degrees of freedom of a single photon," *Phys. Rev. A*, vol. 90, p. 052326, 2014.

[74] L. Chen and W. She, "Single-photon spin-orbit entanglement violating a Bell-like inequality," *J. Opt. Soc. Am. B*, vol. 27, p. A7, 2010.

[75] E. Karimi, J. Leach, S. Slussarenko, B. Piccirillo, L. Marrucci, L. Chen, W. She, S. Franke-Arnold, M. J. Padgett, and E. Santamato, "Spin-orbit hybrid entanglement of photons and quantum contextuality," *Phys. Rev. A*, vol. 82, p. 022115, 2010.

[76] M. A. Nielsen and I. L. Chuang, "Quantum Computation and Quantum Information," *(Cambridge University Press)*, 2000.

[77] D. Bouwmeester, A. K. Ekert, and A. Zeilinger, "The Physics of Quantum Information," *(Springer Verlag, 2000)*, 2000.

[78] F. Steinlechner, M. Gilaberte, M. Jofre, T. Scheidl, J. P. Torres, V. Pruneri, and R. Ursin, "Efficient heralding of polarization-entangled photons from type-0 and type-II spontaneous parametric downconversion in periodically poled KTiOPO$_4$," *J. Opt. Soc. Am. B*, vol. 31, p. 2068, 2014.

[79] K. Banaszek, A. B. U'Ren, and I. A. Walmsley, "Generation of correlated photons in controlled spatial modes by downconversion in nonlinear waveguides," *Opt. Lett.*, vol. 26, p. 1367, 2001.

[80] M. Fiorentino, S. M. Spillane, R. G. Beausoleil, T. D. Roberts, P. Battle, and M. W. Munro, "Spontaneous parametric down-conversion in periodically poled KTP waveguides and bulk crystals," *Opt. Express*, vol. 15, p. 7479, 2007.

[81] A. S. Helmy, B. Bijlani, and P. Abolghasem, "Phase matching in monolithic Bragg reflection waveguides," *Opt. Lett.*, vol. 32, p. 2399, 2007.

[82] P. Abolghasem, J. Han, B. J. Bijlani, A. Arjmand, and A. S. Helmy, "Continuous-wave second harmonic generation in Bragg reflection waveguides," *Opt. Express*, vol. 17, p. 9460, 2009.

[83] J.-B. Han, P. Abolghasem, D. Kang, B. J. Bijlani, and A. S. Helmy, "Difference-frequency generation in AlGaAs Bragg reflection waveguides," *Opt. Lett.*, vol. 35, p. 2334, 2010.

[84] R. Horn, P. Abolghasem, B. J. Bijlani, D. Kang, A. S. Helmy, and G. Weihs, "Monolithic Source of Photon Pairs," *Phys. Rev. Lett.*, vol. 108, p. 153605, 2012.

[85] B. J. Bijlani and A. S. Helmy, "Bragg reflection waveguide diode lasers," *Opt. Lett.*, vol. 34, p. 3734, 2009.

[86] B. J. Bijlani, P. Abolghasem, A. Reijnders, and A. S. Helmy, "Intracavity Parametric Fluorescence in Diode Lasers," *in CLEO: 2011 Postdeadline Papers (Optical Society of America, Washington, DC), Report No. PDPA3.*, 2011.

[87] P. Abolghasem, J. Han, D. Kang, B. J. Bijlani, and A. S. Helmy, "Monolithic Photonics Using Second-Order Optical Nonlinearities in Multilayer-Core Bragg Reflection Waveguides," *IEEE J. Selected Topics Quantum Electron*, vol. 18, p. 812, 2012.

[88] A. Fiore, V. Berger, E. Rosencher, P. Bravetti, and J. Nagle, "Phase matching using an isotropic nonlinear optical material," *Nature*, vol. 391, p. 463, 1998.

[89] A. S. Helmy, "Phase matching using Bragg reflection waveguides for monolithic nonlinear optics applications," *Opt. Express*, vol. 14, p. 1243, 2006.

[90] P. Abolghasem, M. Hendrych, X. Shi, J. P. Torres, and A. S. Helmy, "Bandwidth control of paired photons generated in monolithic Bragg reflection waveguides," *Opt. Lett.*, vol. 34, p. 2000, 2009.

[91] J. Svozilík, M. Hendrych, A. S. Helmy, and J. P. Torres, "Generation of paired photons in a quantum separable state in Bragg reflection waveguides," *Opt. Express*, vol. 19, p. 3115, 2011.

[92] N. Gisin, "Bell's inequality holds for all non-product states," *Phys. Lett. A*, vol. 154, p. 201, 1991.

[93] A. Fine, "Hidden Variables, Joint Probability, and the Bell Inequalities," *Phys. Rev. Lett.*, vol. 48, p. 291, 1982.

[94] N. Matsuda, H. L. Jeannic, H. Fukuda, T. Tsuchizawa, W. J. Munro, K. Shimizu, K. Yamada, Y. Tokura, and H. Takesue, "A monolithically integrated polarization entangled photon pair source on a silicon chip," *Sci. Rep.*, vol. 2, p. 817, 2012.

[95] A. Orieux, A. Eckstein, A. Lemaître, P. Filloux, I. Favero, G. Leo, T. Coudreau, A. Keller, P. Milman, and S. Ducci, "Direct Bell States Generation on a III-V Semiconductor Chip at Room Temperature," *Phys. Rev. Lett.*, vol. 110, p. 160502, 2013.

[96] P. Abolghasem, J. Han, B. J. Bijlani, A. Arjmand, and A. S. Helmy, "Highly efficient second-harmonic generation in monolithic matching layer enhanced AlxGa1-xAs Bragg reflection waveguides," *IEEE Photon. Tech. Lett.*, vol. 21, p. 1462, 2009.

[97] S. V. Zhukovsky, L. G. Helt, D. Kang, P. Abolghasem, A. S. Helmy, and J. E. Sipe, "Generation of maximally-polarization-entangled photons on a chip," *Phys. Rev. A*, vol. 85, p. 013838, 2012.

[98] P. G. Kwiat, K. Mattle, H. Weinfurter, A. Zeilinger, A. V. Sergienko, and Y. Shih, "New High-Intensity Source of Polarization-Entangled Photon Pairs," *Phys. Rev. Lett.*, vol. 75, p. 4337, 1995.

[99] F. Steinlechner, "Sources of Photonic Entanglement for Applications in Space," *Ph.D. thesis, ICFO-Institut de Ciencies Fotoniques*, 2015.

[100] L. Marrucci, C. Manzo, and D. Paparo, "Optical spin-to-orbital angular momentum conversion in inhomogeneous anisotropic media," *Phys. Rev. Lett.*, vol. 96, p. 163905, 2006.

[101] E. Nagali, V. D'Ambrosio, F. Sciarrino, and A. Cabello, "Experimental observation of impossible to beat quantum advantage on a hybrid photonic system," *Phys. Rev. Lett.*, vol. 108, p. 090501, 2012.

[102] V. D'Ambrosio, I. Herbauts, E. Amselem, E. Nagali, M. Bourennane, F. Sciarrino, and A. Cabello, "Experimental implementation of a Kochen-Specker set of quantum states," *Phys. Rev. X*, vol. 3, p. 011012, 2013.

[103] V. D'Ambrosio, E. Nagali, S. Walborn, L. Aolita, S. Slussarenko, L. Marrucci, and F. Sciarrino, "Complete experimental toolbox for alignment-free quantum communication," *Nat. Commun.*, vol. 3, p. 961, 2012.

[104] V. D'Ambrosio, N. Spagnolo, L. Del Re, S. Slussarenko, Y. Li, L. C. Kwek, L. Marrucci, S. Walborn, L. Aolita, and F. Sciarrino, "Photonic polarization gears for ultra-sensitive angular measurements," *Nat. Commun.*, vol. 4, p. 2432, 2013.

[105] R. Horodecki, P. Horodecki, and M. Horodecki, "Violating Bell inequality by mixed spin-1/2 states: necessary and sufficient condition," *Phys. Lett. A*, vol. 200, p. 340, 1995.

[106] R. de J. León-Montiel, A. Vallés, H. M. Moya-Cessa, and J. P. Torres, "Coherent delocalization: views of entanglement in different scenarios," *Laser Phys. Lett.*, vol. 12, p. 085204, 2015.

[107] A. W. Chin, J. Prior, R. Rosenbach, F. Caycedo-Soler, S. F. Huelga, and M. B. Plenio, "The role of non-equilibrium vibrational structures in electronic coherence and recoherence in pigment-protein complexes," *Nat. Phys.*, vol. 9, p. 113, 2013.

[108] T. Baumgratz, M. Cramer, and M. B. Plenio, "Quantifying Coherence," *Phys. Rev. Lett.*, vol. 113, p. 140401, 2014.

[109] A. Streltsov, U. Singh, H. S. Shekhar, M. N. Bera, and G. Adesso, "Measuring Quantum Coherence with Entanglement," *Phys. Rev. Lett.*, vol. 115, p. 020403, 2015.

[110] K. W. Chan, J. P. Torres, and J. H. Eberly, "Transverse entanglement migration in Hilbert space," *Phys. Rev. A*, vol. 75, p. 050101, 2007.

[111] J. L. O'Brien, G. J. Pryde, A. G. White, T. C. Ralph, and D. Branning, "Demonstration of an all-optical quantum controlled-NOT gate," *Nature (London*, vol. 426, p. 264, 2003.

[112] K. Nemoto and W. J. Munro, "Nearly Deterministic Linear Optical Controlled-NOT Gate," *Phys. Rev. Lett.*, vol. 93, p. 250502, 2004.

[113] S. V. Polyakov and A. L. Migdall, “Quantum radiometry,” *J. Mod. Opt.*, vol. 56, p. 1045, 2009.

[114] D. Bouwmeester, J.-W. Pan, K. Mattle, M. Eibl, H. Weinfurter, and A. Zeilinger, “Experimental quantum teleportation,” *Nature (London)*, vol. 390, p. 575, 1997.

[115] M. A. Nielsen and I. L. Chuang, “Quantum Computation and Quantum Information,” *(Cambridge: Cambridge University Press)*, 2010.

[116] P. J. Mosley, J. S. Lundeen, B. J. Smith, P. Wasylczyk, A. B. U’Ren, C. Silberhorn, and I. A. Walmsley, “Heralded Generation of Ultrafast Single Photons in Pure Quantum States,” *Phys. Rev. Lett.*, vol. 100, p. 133601, 2008.

[117] J. Flórez, O. Calderón, A. Valencia, and C. I. Osorio, “Correlation control for pure and efficiently generated heralded single photons,” *Phys. Rev. A*, vol. 91, p. 013819, 2015.

[118] Z.-L. Zhou, H. Yuan, and L.-F. We, “Entanglement, Quantum Discord, and Non-locality in Bell-Diagonal States,” *Int. J. Theor. Phys.*, vol. 52, p. 420, 2013.

[119] E. Knill, R. Laflamme, and G. J. Milburn, “A scheme for efficient quantum computation with linear optics,” *Nature (London)*, vol. 409, p. 46, 2001.

[120] K. Lemr, K. Bartkiewicz, A. Černoch, M. Dušek, and J. Soubusta, “Experimental Implementation of Optimal Linear-Optical Controlled-Unitary Gates,” *Phys. Rev. Lett.*, vol. 114, p. 153602, 2015.

[121] Z. Guan, H. He, Y.-J. Han, C.-F. Li, F. Galve, and G.-C. Guo, “Entangling power of two-qubit gates on mixed states,” *Phys. Rev. A*, vol. 89, p. 012324, 2014.

[122] F. Verstraete and M. M. Wolf, "Entanglement versus Bell Violations and Their Behavior under Local Filtering Operations," *Phys. Rev. Lett.*, vol. 89, p. 170401, 2002.

[123] F. Verstraete, K. Audenaert, and B. D. Moor, "Maximally entangled mixed states of two qubits," *Phys. Rev. A*, vol. 64, p. 012316, 2001.

[124] J. Batle and M. Casas, "Nonlocality and entanglement in qubit systems," *J. Phys. A*, vol. 44, p. 445304, 2011.

[125] C. Jarlskog, "A recursive parametrization of unitary matrices," *J. Math. Phys. (N.Y.)*, vol. 46, p. 103508, 2005.

[126] W. J. Munro, D. F. V. James, A. G. White, and P. G. Kwiat, "Maximizing the entanglement of two mixed qubits," *Phys. Rev. A*, vol. 64, p. 030302(R), 2001.

[127] T.-C. Wei, K. Nemoto, P. M. Goldbart, P. G. Kwiat, W. J. Munro, and F. Verstraete, "Maximal entanglement versus entropy for mixed quantum states," *Phys. Rev. A*, vol. 67, p. 022110, 2003.

[128] D. Huang, E. Swanson, C. Lin, J. Schuman, W. Stinsona, W. Chang, M. Hee, T. Flotte, K. Gregory, C. Puliafito, and et al., "Optical coherence tomography," *Science*, vol. 254, p. 1178, 1991.

[129] X. Y. Zou, L. J. Wang, and L. Mandel, "Induced coherence and indistinguishability in optical interference," *Phys. Rev. Lett.*, vol. 67, p. 318, 1991.

[130] J. G. Fujimoto, "One of the authors of the paper, was asked once in the SPIE International Congress on Optics and Optoelectronics, which took place in Warsaw, why the technique was not more appropriately called something like *white-light interferometry* or *wide-band interferometry*, and his answer was... *the name is everything.*," 2005.

[131] G. Barreto, V. Borish, G. D. Cole, S. Ramelow, R. Lapkiewicz, and A. Zeilinger, "Quantum imaging with undetected photons," *Nature*, vol. 512, p. 409, 2014.

[132] D. Kang and A. S. Helmy, "Generation of polarization entangled photons using concurrent type-I and type-0 processes in AlGaAs ridge waveguides," *Opt. Lett.*, vol. 37, p. 1481, 2012.

[133] J. Svozilík, M. Hendrych, and J. P. Torres, "Bragg reflection waveguide as a source of wavelength-multiplexed polarization-entangled photon pairs," *Opt. Express*, vol. 20, p. 15015, 2012.

[134] S. V. Zhukovsky, L. G. Helt, P. Abolghasem, D. Kang, J. E. Sipe, and A. S. Helmy, "Bragg reflection waveguides as integrated sources of entangled photon pairs," *J. Opt. Soc. Am. B*, vol. 29, p. 2516, 2012.

[135] W. Thirring, R. A. Bertlmann, P. Köhler, and H. Narnhofer, "Entanglement or separability: the choice of how to factorize the algebra of a density matrix," *Eur. Phys. J. D*, vol. 64, p. 181, 2011.

[136] R. Horodecki and P. Horodecki, "Perfect correlations in the Einstein-Podolsky-Rosen experiment and Bell's inequalities," *Phys. Lett. A*, vol. 210, p. 227, 1996.

[137] T. Hiroshima and S. Ishizaka, "Local and nonlocal properties of Werner states," *Phys. Rev. A*, vol. 62, p. 044302, 2000.